An emerging ground-based aerosol climatology:

Aerosol Optical Depth from AERONET

B.N.Holben[1], D.Tanré[2], A.Smirnov[1,3], T.F.Eck[1,4, 19], I.Slutsker[1,3], N. Abuhassan[1,3], W.W. Newcomb[1,3], J.S. Schafer[1,4, 20], B Chatenet[5], F. Lavenu[6], Y.J.Kaufman[7], J. Vande Castle[8], A.Setzer[9], B.Markham[1], D. Clark[10], R. Frouin[11], R. Halthore[12, 21], A. Karneli[13], N. T. O'Neill[14], C. Pietras[15], R.T. Pinker[16], K. Voss[17], G. Zibordi[18]

[1] Biospheric Sciences Branch, NASA's GSFC, Greenbelt, MD, USA
[2] Laboratoire d'Optique Atmospherique, CNRS, Villeneuve d'Ascq, France
[3] Science Systems and Applications, Inc., Lanham, MD, USA
[4] Raytheon STX Corporation, Lanham, MD, USA
[5] Laboratoire Interuniversitaire des Systèmes Atmosphériques, Universités Paris VII et Paris XII, CNRS, 94010 - Créteil Cedex, France
[6] CESBIO/CNRS, Toulouse, France
[7] Climate and Radiation Branch, NASA's GSFC, Greenbelt, MD, USA
[8] University of New Mexico, Albuquerque, New Mexico, USA
[9] Instituto de Pesquisas Espaciais, Sao Jose dos Campos, San Paolo, Brazil
[10] NOAA, Silver Hill, MD, USA
[11] Scripps Institute of Oceanography, La Jolla, CA, USA
[12] Department of Applied Science, Brookhaven National Laboratory, Upton, NY, USA
[13] Ben Gurion Univ. of the Negev, Sede Boker Campus 84990, Israel
[14] CARTEL, Universite de Sherbrooke, Sherbrooke, Quebec, Canada
[15] SAIC-GSC, Beltsville MD and NASA/GSFC, Greenbelt, MD., USA
[16] Department of Meteorology, University of MD, College Park, MD, USA
[17] Dept. of Physics, University of Miami, Miami, FL, USA
[18] Space Applications Institute, Joint Research Centre of the European Commission, Ispra, Italy
[19] Now at Goddard Earth Sciences and Technology Center, University of Maryland, Baltimore County, Baltimore, MD, USA
[20] Now at Science Systems and Applications, Inc., Lanham, MD, USA
[21] Now at Code 7228, Naval Research Laboratory, Washington DC, USA

Abstract

Long term measurements by the AERONET program of spectral aerosol optical depth, precipitable water and derived Angstrom exponent were analyzed and compiled into an aerosol optical properties climatology. Quality assured monthly means are presented and described for nine primary sites and twenty-one additional multi-year sites with distinct aerosol regimes representing tropical biomass burning, boreal forests, mid latitude humid climates, mid latitude dry climates, oceanic sites, desert sites and background sites. Seasonal trends for each of these nine sites are discussed and climatic averages presented.

Introduction

Man is altering the aerosol environment through land cover change, combustion of fossil fuels and the introduction of particulate and gas species to the atmosphere. Each perturbation has some impact on the local aerosol environment. How much aerosol man is contributing to the atmosphere is not known. Even more fundamental, we do not know the current total aerosol loading; thus we have no definitive measure of change for future assessment (Andrea, 1996). Regardless of current conditions, the extent of local aerosol perturbations on a global scale is the subject of extensive ground level, airborne and satellite research [*Kaufman et al*, 1998; *King et al*., 1999]. Investigations have been initiated by concerns ranging from radiative forcing by aerosols, long term impacts on climate and public health, aesthetic and ecological impacts, as well as the future of sea level habitations and political entities. The resources put into such investigations have largely been local and contributed to an enormous, yet mostly uncoordinated data base that makes global assessment of our past and present aerosol disposition difficult. Coordination between surface based network observations and satellite measurements

will be required to develop a long term monitoring system of the Earth's aerosol environment.

The simplest, and in principle, the most accurate and easy to maintain monitoring systems are ground-based**.** Aerosol optical depth is the single most comprehensive variable to remotely assess the aerosol burden in the atmosphere from ground-based instruments. This variable is used in local investigations to characterize aerosols, assess atmospheric pollution and make atmospheric corrections to satellite remotely sensed data. It is for these reasons, that a record of aerosol optical depth spanning most of the 20th century has been measured from sun photometers. The vast majority are site specific, short term investigations with little relevance for seasonal, annual or long term trend analysis, however a few multi-year spatial studies have contributed to our knowledge and experience (Table 1). The following section reviews those investigations past and present that significantly addressed long-term measurements over widely distributed locations or provided a significant contribution that allowed development of a network for long-term photometric aerosol observations.

The earliest systematic results come from the Smithsonian Institution Solar observatories. *Roosen et al.* [1973] computed extinction coefficients from 13 widely separated sites during the first half of the twentieth century using spectrobolometer observations by the Astrophysical Observatory of the Smithsonian Institution. They concluded the aerosol burden did not detectibly change at remote high altitude sites from 1905 to 1950. Seasonal and volcanic eruptions were evident however long term trends were not.

Volz [1957] developed an analog sun photometer with a 500 nm interference filter that became the basis for extensive observational networks in Europe [*Volz*, 1968] and the United States. *Flowers et al* [1969] described the US Volz sun photometer network

consisting of 29 stations across the US from 1961 to 1966. They showed the base 10 turbidity parameter to vary as a function of locality and time of year and thus were the first to develop an aerosol climatology based on light extinction. Highest values were reported for eastern US stations in July and August, lowest values in the intermountain basin of the Western US. Although the record is only available from graphs presented in the above citation, values are generally consistent with current measurements. An accuracy assessment of the *Flowers et al*. [1969] data is not presented. The European network operated 30 sun photometers from 1963 to 1967 [*Volz,* 1969]. Volz reported a case study from central Europe but no apparent attempt was made to put the database into a climatological context. No accuracy assessments were made for this network. The database is available from the National Climatic Data Center in Ashville, NC, USA.

Shaw [1982] reported 800 measurements of atmospheric aerosol optical depth (500 nm) poleward of 65 degrees latitude prior to 1982. He suggested the southern polar regions are pollution free with background conditions ranging from 0.025 at McMurdo to 0.012 at the South Pole. Similar background conditions as McMurdo were reported for Barrow and Fairbanks, AK in summer but values increase to 0.135 and 0.110 respectively in March and April with the onset of arctic haze. He also converted *Volz* [1968] turbidity measurements from 1912 to 1922 to AOD at Uppsala (60°N) for March means and noted the background values are ~0.06 lower than contemporary measurements suggesting that arctic haze is a recent phenomena of anthropogenic origin.

Herber et al. [1993] reported several long-term measurements from coastal Antarctica and satellite observations. Records dating to 1956 clearly showed the influence of volcanic eruptions on stratospheric loading however no long term discernable trends are observable suggesting no anthropogenic induced trends.

Gushchin [1988] reported extensive measurements in the former Soviet Union from 1972 to 1984 as part of the BAPMoN program. Observations were taken within the spectral range of 340-627 nm at more than 30 sites, which characterize rural, urban/industrial, maritime/continental and desert aerosol. Most observations were not continuous, but multi-year and monthly averages of aerosol optical depth and its spectral dependence along with the maximal and minimum values were presented for some sites.

West Africa and desert dust aerosol has been the focus of three network sun photometric investigations for much of the 1980's. The African Turbidity Network from 1980 to 1984 [*D'Almeida,* 1987], NASA's 15 site Sahelian network [*Holben et al*., 1991] and the Niger network from 1986-1987 [*Ben Mohamed et al*, 1992]. Clearly these networks demonstrated the temporal and spatial variability and overall high aerosol loading in West Africa, during this decade of extreme Sahelian drought.

Smirnov et al. [1995] compiled and summarized aerosol optical depth observations from over 50 published sources for marine observations from cruises spanning 30 years of observations worldwide. These results showed a wide scatter of optical parameters in general and some significant scatter between optical data for certain areas in particular. Coastal data are greatly influenced by continental sources and accordingly the aerosol optical depth values are as a rule greater than in the remote ocean air. Unfortunately, numerous experiments were sporadic, employed only a few wavelengths and measurement accuracy sometimes was unknown. However, it was evident that in a clean maritime atmosphere quasi-neutral spectral behavior of aerosol optical depth predominates.

Aerosol optical depth has been retrieved using broadband (0.3-4 μm) direct normal observations made from pyrheliometers, which are more commonly deployed at meteorological observatories. *Jinhuan and Liquan* [2000] reported observations from a

twelve-station network operating in China's northern interior from 1980 to 1994. Effective Optical depth retrievals were made at 750 nm with an estimated accuracy of 10% due to the retrieval method but no mention is made of errors due to calibration uncertainty. High optical depths, for the colder interior cities in winter due to emissions from coal heating and spring-time pulses from dust sources, were routinely reported. In contrast, Beijing reported a summer maximum. None of these sites necessarily represent rural conditions.

Dutton [1994] presented broad band aerosol optical depths from pyrheliometers (0.3-3 μm) as monthly average anomalies from measurements taken at four NOAA/CMDL background stations (Barrow, AK, Mauna Loa, HI, Samoa, U.S. Territories and South Pole) from 1977 to 1992. All sites being far removed from anthropogenic sources of aerosols showed no significant long-term trends after the effect of volcanic eruptions were removed. Slight seasonality was observed at Mauna Loa associated with Asian dust from March through May and Arctic haze during the same time period in Barrow.

Historically the most ambitious attempt to monitor background aerosol optical depth levels was that organized under the auspices of the WMO BAPMoN program which officially operated from 1972 to 1992. The network was composed of 95 sites operated by member countries that provided processed data to the National Climate Data Archive in Ashville, NC, USA. The diversity of instruments, expertise, analysis methods and quality control led a WMO evaluation committee to recommend abandonment of the network and declare the data archive in its present form as unsuitable '…for scientific analysis of either short or long term changes in global aerosol optical depth.' Experience from BAPMoN was used in formulating and establishing the follow-on network Global Atmospheric Watch (GAW) in 1996. The GAW network consists of approximately 12 background locations with identical instruments provided and supported by the Swiss

government. Results from this network are not published but information is obtained through the GAW website. Subsets of the BAPMoN program have been shown to be successful in Canada [*Smirnov et al*., 1996] or developed spin-off networks as in Australia [*Forgan*, 2000].

Michalsky et al. [1994] reported on a network of 11 rotating shadowband radiometers established in he Eastern US. The network is notable for its high temporal resolution and in situ calibration approach. Data collection began in 1992 and continues to the present and is available through the Internet. This instrument approach has rapidly expanded to numerous research facilities and programs [*Bigelow et al*., 1998] but has not coalesced into a coordinated network.

A developing network of inexpensive light emitting diode handheld sun photometers is being supported by NASA's Global Learning and Observations to Benefit the Environment (GLOBE) program with the goal of involving student scientists to take scientific quality measurements [*Mims*, 1999]. The potential to make regular observations at internationally dispersed secondary schools with a common database could be of great benefit educationally and scientifically. No results are yet available.

The AERONET program [*Holben et al*., 1998] is an automatic robotic sun and sky scanning measurement program that has grown rapidly to over 100 sites world wide (Figure 1). The program provides the satellite remote sensing, aerosol, land and ocean communities quality assured aerosol optical properties to assess and validate satellite retrievals. The real time globally distributed network has grown through international federation (PHOTON, primarily in Europe and West Africa, AEROCAN in Canada) since 1993. The result has been a long-term quality assured record for a large diversity of aerosol types, mixtures and source and transport regions. An unaffiliated network based in Japan (Skynet) provides similar measurements.

This paper presents the first of a multi-paper study of the climatology of aerosol optical properties retrieved from AERONET measurements. We present here the monthly aerosol optical depths measured or interpolated to 500 nm, the multispectral Angstrom parameter (or wavelength exponent) and the retrieved precipitable water at nine selected sites representing aerosols from biomass burning, desert dust, biogenic/background and anthropogenic/urban sources. In most cases, the monthly record is continuous however several sites are limited to summer and/or dry seasons summaries due to the difficulty of maintaining year-long measurements. To provide a more complete assessment of the program results we provide an appendix of monthly and yearly average aerosol optical depth, Angstrom exponent and precipitable water for additional AERONET sites with over two years of quality assured data.

Instrumentation and methods

All of the measurements reported in this paper were made with CIMEL sun/sky radiometers, which are a part of the AERONET global network. These instruments are described in detail in *Holben et al.* [1998], however a brief description will be given here. The automatic tracking Sun and sky scanning radiometers make direct Sun measurements with a 1.2^0 full field of view at least every 15 min at 340, 380, 440, 500, 675, 870, 940, and 1020 nm (nominal wavelengths). The direct sun measurements take 8 seconds to scan all 8 wavelengths, with a motor driven filter wheel positioning each filter in front of the detector. A sequence of 3 measurements (termed a triplet) taken 30 seconds apart are made resulting in 3 measurements at each wavelength within a one minute period. These solar extinction measurements are then used to compute aerosol optical depth at each wavelength ($\tau_a(\lambda)$ except for the 940 nm channel, which is used to retrieve precipitable water (PW) in centimeters. The filters utilized in these instruments are interference filters

with bandpass (full width at half maximum) of the 340 nm channel at 2 nm and the 380 nm filter at 4 nm, while the bandpass of all other channels is 10 nm.

The data, which we analyzed for the Goddard Space Flight Center (GSFC), in Maryland, utilized only $\tau_a(\lambda)$ measurements from Mauna Loa Observatory (MLO) calibrated instruments**.** These reference instruments are typically recalibrated at MLO every ~3 months using the Langley plot technique with morning data only. The zero air mass voltages (V_o, instrument voltage for direct normal solar flux extrapolated to the top of the atmosphere (Shaw, 1983)) are inferred with an uncertainty of approximately 0.2 to 0.5% for the MLO calibrated reference instruments (Holben et al., 1998). Therefore the uncertainty in τ_a due to the uncertainty in zero airmass voltages (computed as the standard deviation/mean of the V_o values from MLO) for the reference instruments is better than 0.002 to 0.005.

The stability in time of the V_0 values derived from MLO Langley analyses for one of our reference instruments (#101) is shown in Fig.2. The data in this figure cover the time period of September 30, 1997 to September 11, 1999, a nearly 2 year interval. The filters in use for this instrument and all others in the AERONET network from 1997 onward were ion assisted deposition interference filters. We computed the average yearly change in V_0 from a linear regression of V_0 versus time for the entire 711 day data record. As depicted in Fig 2, there are varying rates of change for the different wavelengths, ranging from 0.24%/ year for 870 nm to -3.90%/year for 675 nm. The change in V_0 with time show in general a linear tendency, with the exception of the 940 nm filter. This is due to a much larger uncertainty in V_0 determination for the 940 nm channel as a result of water vapor variability at MLO as contrasted with a very stable aerosol environment. The repeatability of morning Langley derived values of V_0 for aerosol channels at MLO, from typically 5 to 15 mornings, is excellent with a coefficient of variability (standard

deviation/mean) averaging only ~0.3-0.5% while the value for the 940 nm channel averages 2-4%.

The Sun/sky radiometers at sites other than GSFC utilized in this study were intercalibrated against a MLO calibrated AERONET reference instrument at GSFC both before deployment in the field and post-deployment. The period of time between calibrations for field instruments typically varies from 6 to 12 months. A linear rate of change in time of the zero airmass voltages is then assumed in the processing of the data from field sites. Our analysis suggests that this results in an uncertainty of approximately 0.01 – 0.02 in $\tau_a(\lambda)$ (wavelength dependent) due to calibration uncertainty for the field instruments.

Eck et al. [1999] have computed the combination of calibration uncertainties (V_0) and uncertainty in ozone (due to seasonality and atmospheric dynamics) and Rayleigh optical depth (due to variability in air pressure), for optical airmass of 1, in the manner of *Russell et al.* [1993]. The resulting estimated total uncertainty is ~0.010-0.021 in computed $\tau_a(\lambda)$ for field instruments (which is spectrally dependent with the higher errors in the UV), and approximately 0.002 to 0.009 for reference instruments. *Schmid et al*. [1999] compared $\tau_a(\lambda)$ values derived from 4 different solar radiometers (one was an AERONET sun-sky radiometer), operating simultaneously together in a field campaign and found that the τ_a values from 380 to 1020 nm agreed to within 0.015 (rms), that is similar to our estimated level of uncertainty in τ_a retrieval for field instruments.

The technique of *Bruegge et al.,* [1992] is used to retrieve precipitable water. Given the current discussion for the optimal method for PW retrievals from sun photometry observations [*Schmid et al., 2000*] and the relatively large uncertainty in the modified Langley Vo, we conservatively estimate our uncertainty to be ±10%. Informal

comparisons to retrievals of PW from raman lidar, microwave radiometer, other sun photometer methods and radiosondes, support this estimate.

The Angstrom wavelength exponent, α, values presented in this paper were computed as the slope of the linear regression of $\ln\tau_a$ versus $\ln\lambda$ using the 440, 500, 675, and 870 nm filter data. Prior to 1995 there were no 500 nm filter data therefore the α values in 1993-1994 were computed from the 440, 675 and 870 nm data only. The τ_a data at 500 nm that we present for 1993-1994 are computed from interpolation of the 440 and 675 nm data on a $\ln\tau_a$ versus $\ln\lambda$ scale. It is recognized, that there is often significant spectral variation of α for aerosol size distributions with an accumulation mode [*Eck et al.*, 1999; *O'Neill et al*., 2000]. In this paper we present only the 440-870 nm linear fit determination of α as a first order parameter indicative of the general size distribution and the relative dominance of fine versus coarse mode particles.

The AERONET $\tau_a(\lambda)$ data in this paper were cloud screened following the methodology of *Smirnov et al.* [2000a], and here we present just a brief outline of the procedure. The principal filters used for the cloud screening are based on temporal variability of the $\tau_a(\lambda)$, with the assumption being that greater temporal variance in τ_a is due to the presence of clouds. The first filter is a check of the variability of the three τ_a values measured within a one-minute period. If the difference between minimum and maximum $\tau_a(\lambda)$ within this one minute interval is greater than 0.02 (for τ_a less than 0.667) or $0.03\tau_a$ (for τ_a greater than 0.667) then the measurement is identified as cloud contaminated. Then the time series of the remaining $\tau_a(\lambda)$ are analyzed for the presence of rapid changes or spikes in the data. A filter based on the second derivative of the logarithm of $\tau_a(\lambda)$ as a function of time is employed to identify rapid variations which are then eliminated as observations affected by cloud. Other secondary order cloud

screening and data quality checks are also made and these are described in detail in *Smirnov et al*. [2000]. This cloud screening technique has not been validated on a broad scale although the procedure was favorably tested on experimental data obtained in different geographical and optical conditions,(*Smirnov et al*. [2000]). For a variety of sites, our cloud screening algorithm eliminated from 10% to 50% of the initial data.

Mauna Loa, Hawaii

The Cimel sunphotometer on Mauna Loa, Hawaii is located at the Mauna Loa Observatory (MLO; 19°53' N, 155°57' W) which is 3400 m above sea level on the north side of the gently sloping shield volcano (summit is 4170 m). The nearby surface consists of bare lava rock with no vegetation or soil and therefore minimal local production of aerosol. In addition, other factors which contribute to the very low aerosol loading at MLO are its mid-Pacific location (>3500 km from the nearest continent) and its height above the marine boundary layer. MLO is considered to be the best location for calibration of direct sun observing instrumentation by the Langley method applied to morning data (airmass > 2), due to the extremely low and stable aerosol optical depth [*Shaw*, 1983]. However, typically after 9-10 am local time air flowing up the to the observatory altitude from the breakup of the marine inversion layer often results in rapid temporal variation and an increase in aerosol concentrations [*Perry et al*., 1999; *Shaw*, 1979]. Emission of gasses and the formation of aerosols as a result of volcanic activity on the island of Hawaii occur primarily below the MLO altitude, but are sometimes transported to the observatory altitude and above during the daytime by upslope flow caused by heating of the mountain slope and growth of the marine mixed layer [*Luria*, 1992; *Ryan*, 1997].

The aerosol optical depth data, which we present here, are daily averages representative of the complete diurnal cycle (Figure 3, Table 2). Since cloud cover is typically greater in the afternoon, due to the arrival of moisture rich marine boundary layer air, there are more morning cloudless observations and therefore the daily averages of aerosol optical thickness at 500 nm (τ_{a500}) are more heavily weighted by morning data when τ_{a500} is also lower. As a result of frequent calibrations from morning Langley analysis, our estimated uncertainty in instantaneous values of τ_{a500} is approximately ±0.003. The seasonal variation of the monthly average aerosol optical depth (Fig. 3a) shows maximum values in the spring season months of March, April, and May. This seasonal peak in spring is due to the long-range transport of primarily Asian aerosols to MLO [*Perry et al.*, 1999; *Shaw*, 1980]. *Perry et al*. [1999] have measured spring peaks in fine soil mass and elements associated with fly ash (bromine, zinc, and lead) from coal burning, in addition to an anthropogenic sulfate enhancement. Lidar observations at MLO [*Barnes and Hoffman*, 1997] show only a slight enhancement of stratospheric aerosol backscatter from the Mt. Pinatubo eruption (June 15, 1991) in 1994 and approaching background levels in 1995. Nearly continuous monitoring of τ_a by AERONET commenced in 1996 (Fig. 3b), therefore most of the data presented here are not significantly affected by volcanic aerosols in the stratosphere, since there are only 2 months with observations in 1994.

Daily mean values of τ_{a500} (Fig. 3c) show the spring seasonal peaks (maximum daily values of ~0.09) but also very large day-to-day variability due to variation in air mass trajectories transporting aerosols from differing source regions to MLO [*Perry et al*., 1999]. Daily variability is also due in part to variation in the production and transport of volcanic aerosols from the active volcanoes on the island. It is noted that τ_{a500} in the spring months (March-May) of 1999 was significantly higher than was measured for the

spring months of 1996-1998 (Fig.3b and 3c). Thus it appears that there is significant inter-annual variability in aerosol transport to MLO. Minimum values throughout the 1995-1998 period range from approximately 0.006 to 0.009, which is similar to the minimum for 1982-1992 observed by *Dutton et al.* [1994] of 0.008 from the winter of 1990-1991prior to the Mt. Pinatubo eruption. It is noted however, that *Dutton et al.* [1994] computed τ_{a500} from measurements made in the morning only during the Langley measurement sequence, and thus their values are lower than would be for daily averages, which is what we report here. *Dutton et al*. [1994] also determined a stratospheric background value of aerosol optical depth of 0.004 for the winter of 1990-1991. *Shaw* [1979] computed a mean value of total atmospheric column τ_{a500}=0.019 for MLO measurements made from March-August 1976 and January-February 1977. The value we compute from the multi year AERONET observations from monthly means *f*or January-August (the *s*ame months as [Shaw, 1979]) is similar, 0.022. In addition, Shaw [1982] computed an annual mean τ_{a500} at MLO for 1980 of 0.020, which is equal to our multi-year annual mean of 0.02. The frequency of occurrence histogram of τ_{a500} for the entire data record of 1994-1998 (Fig.3e) shows a skewed distribution with a peak from 0.01 to 0.02, with lesser frequencies trailing off at higher τ_a values.

Daily average precipitable water amounts (Fig. 3d), in cm, exhibit large daily variability and some seasonality with higher values in summer and fall. The range of values from less than 0.05 cm to almost 1.0 cm is nearly identical to the range of PW values measured by *Dutton et al.* [1985] from 1978 through 1983 (morning data only), also from sunphotometric retrievals. It is interesting to note that the dry period in the winter-spring of 1998 (Fig.3d) is very similar in duration and magnitude to a dry period observed by *Dutton et al.* [1985] at MLO from December 1982 through March 1983 both of which occurred during strong El Nino cycles. The relationship between aerosol optical

depth and precipitable water (Fig.3h) shows no significant correlation, thus suggesting that part of the reason may be that aerosol and water vapor are transported at different altitudes above MLO and/or that there are trajectories from several source regions with differing seasonal combinations of τ_{a500} and PW.

The Angstrom wavelength exponent plotted versus τ_{a500} (Fig.3g) shows a weak trend of decreasing values of α as τ_{a500} increases. This may be the result of some of the highest observations of τ_{a500} being associated with the transport of Asian soil dust composed of coarse mode (>1 μm) sized particles. All of the values of α>0.8 for τ_{a500} >0.06, shown in Fig.3g are from spring 1999 when there was a higher than normal level of transport of aerosol to MLO. These episodes of relatively high α and τ_{a500} in 1999 suggest transport of industrial pollution or possibly mixed desert dust and industrial pollution. Part of the reason for the wide range in α values for τ_{a500} < 0.02 is due to the uncertainty in τ_a of ~0.003 approaching the magnitude of the τ_a data, thus resulting in larger errors in α computation. The frequency of occurrences histogram of α (Fig.3f) shows a broad peak from ~1.0 to 2.0 with a minimum near zero and a maximum at 3.0. The annual average value of α computed from the monthly means is 1.48. In comparison, *Dutton et al.* [1994] computed an α of 0.7 for near background conditions in 1990-1991 and *Shaw* [1979] inferred α values that ranged from 1.1 to 3.5 with a mean of 1.63, however his data from 1976 was influenced by volcanic aerosols in the stratosphere from the Augustine Volcano eruption. At low τ_a, the stratospheric background aerosol optical depth (~0.003 to 0.005) may comprise a significant contribution to the total column integrated aerosol optical properties**.** Typical non-volcanic stratospheric optical depths, as summarized by *Russell et al.* [1993], result in α varying from 1.0 to 1.5 for the 500 to 1000 nm wavelength range.

GSFC, Greenbelt, Maryland

Goddard Space Flight Center ($39^0$01'N, 76^0 52'W, 50 m elevation), located in suburban Washington, D.C. and approximately 30 km south of industrial Baltimore, aerosol environment is influenced by a synoptic scale meteorology. A southerly flow due to the Bermuda high is a dominant feature from late spring through the early fall months and a west and northwesterly flow typifies the other months. Some episodes of each type of flow may occur at any time of the year and be regionally modified by cold fronts with a strong southerly flow in advance of the front and a northwesterly flow behind. Most heavy industry is located to the north and local emissions are dominated by automobiles, owned by the 2.3 million metropolitan area residents. The landscape is dominated by deciduous trees leafed out from late April through October.

Figure 4a illustrates the monthly averaged aerosol optical depth at 500 nm for the seven year record (1993-1999) at Goddard. A total of 1297 daily averages are analyzed. The aerosol optical depth is dominated by a marked increase in optical depth from June through September which peaks during July and August. The seven-year July mean of τ_{a500} is 0.48. In contrast, the aerosol optical depth decreases to a minimum during the winter months, averaging ~ 0.10 from November-January. Standard deviations generally increase with the mean values of τ_a. Monthly averages of τ_a and α for the whole period of observations are shown in Fig.4c and 4d. With respect to the τ_a variations, a "classical" annual pattern with an increase to maximum turbidity in the summertime [*Flowers et al*., 1969; *Peterson et al*., 1981] is apparent in all the years. A winter minimum is always in evidence. Because of the post-Pinatubo contribution, τ_a was slightly higher for the fall and winter of 1993-1994 than the value expected from the historical data. A notable decrease of the Angstrom parameter α (Fig.4d) in 1993 is also

associated with the post-Pinatubo effect. Generally, no regular pattern is seen in the mean monthly values of the Angstrom parameter, although a late winter and early spring minimum can be noticed. The mean annual values of α are close to 1.6-1.7 for all years (except for 1993).

Daily average values of $\tau_{a\ 500}$ for all 7 years show very large day to day variation especially during the summertime (Fig.4g). The dramatic increase in summer aerosol loading over the eastern US is a dynamic mixture of natural and anthropogenic sources, processed by convection within humid air masses. A histogram of τ_a and α is shown in Fig. 4i and 4j. The aerosol optical depth probability distribution is rather narrow with the modal value of about 0.1. The probability distribution of α is relatively broader with the modal value of about 1.7. Figure 5 shows the seasonal variability of aerosol optical depth and the Angstrom parameter (DJF is winter, MAM is spring, JJA is summer, and SON is fall). It can be seen from Figure 5 and Table 3 that the atmosphere was typically more turbid and more variable in the summer (wider distributions or larger σ values). The winter months have the narrowest probability distribution of τ_{a500} with a modal value about 0.08. In the spring the maximum shifts towards greater values (0.18), and in the fall the distribution widens as higher values of τ_a appear. The complex nature of atmospheric processes, associated with the competition of air flows from northern and southwestern sectors, and frequent air stagnation above the area, are most likely responsible for the fall pattern [*Bryson*, 1966; *Trewartha*, 1954]. Parallel sets of graphs of the Angstrom parameter do not display any obvious season to season trends.

The daily average values of the total precipitable water amount, (Fig.4h), show typically higher values in the summertime which range to maximum values of 4-5.5 cm, while in November-February values are typically less than 1 cm. This is consistent with the general synoptic pattern for the area in which polar and arctic air masses, which are

cold and dry, dominate in winter, and moist warm tropical air masses dominate in summer. Mean monthly values of the precipitable water are presented in Figure 4e. The relatively cold summer of 1996 was influenced by air advected from northern Canada yielding smaller values for the months of July and August. Otherwise, the temporal annual variability of precipitable water is quite similar from year to year. Derived mean monthly values are consistent (within 10%) with the calculations of *Gueymard* [1994] (estimates based on the long-term surface-level temperature record) made for the Washington D.C. area.

The relationship between daily averages of precipitable water and aerosol optical depth at 500 nm (Fig. 4l) shows strong correlation (r^2 of 0.56). This result is consistent with the intra-annual variability of aerosol optical properties, synoptic air masses and associated amount of precipitable water. The trend may be observed in Fig. 4f where mean monthly values of $\tau_{a\ 500}$ are plotted versus PW monthly means increasing the r^2 to 0.79. The exponential fit is consistent with the relationship established for the US Atlantic coast sites during the TARFOX experiment [*Smirnov et al*., 2000b].

Sevilleta, New Mexico

Sevilleta is located in the arid intermountain basin of the American Southwest, approximately 1400 km east of the Pacific Ocean (34˚21'N, 106˚53'W, elevation 1850 m). The annual precipitation (240 mm/yr.) is characterized by the dry, cold, winter months of December through February (10 to 15 mm/mo.) with a transition into the warmer, windy, but still generally dry, spring period of March-May. Spring is followed by a hot, dry June and then a hot but wetter summer "monsoon" period of July and August and early September (40 to 45 mm/mo.). Summer precipitation generally occurs as intense thunderstorms often account for half of the annual total. Fall is characterized

by moderate temperatures with drying from October through November [*Moore*, 1996]. El-Niño and La-Niña events strongly influence the non-monsoon precipitation [*Dahm et al*., 1994].

The sparse vegetation, consisting of annual grasses and shrub species, is typical of high altitude intermountain deserts. Vegetation cover is generally dictated by available moisture and responds rapidly to seasonal rainfall events. Thus dry conditions during high spring winds likely contribute to local aerosols. The nearest city, Albuquerque, New Mexico is 100-km north, thus no local anthropogenic sources are present.

The aerosol optical depth record began in May 1994 and continues almost unbroken to the present (Fig. 6, Table 4). The monthly averaged record clearly shows the long term seasonal variations in aerosol optical depth. A gradual increase in τ_{a500} from the January low of 0.03 to relatively broad but low summer peak in June, July, August and September of 0.11 is followed by a gradual decrease through the fall to the mid winter minimum values (Fig. 6a). The mean annual τ_{a500} of 0.08 represents one of the lowest values in the AERONET network.

Summer maximums of τ_a typically occur in July-September and minimums in November - February (Fig. 6c). Daily averages as expected show large variability within the mean annual cycle which typically varies between 0.02 to ~0.30 at 500 nm (Fig. 6d). Instantaneous measurements occasionally far exceed daily averaged maximums during dust storms but are short lived. Some dust events, which may be associated with cold fronts and cloudy conditions, are filtered out of the data set.

Retrieved precipitable water closely follows the aerosol dynamics with peak values in July through September (peak daily averages as high as 3 to 3.5 cm) associated with the summer monsoon flow into the desert Southwestern US (Fig. 6e). Minimum values occur throughout the winter season with lowest values in November-December (below

0.5 cm). It is noteworthy that the maximum aerosol loading does not occur during the dry windy spring period but rather is associated with the wettest time of year when water vapor may play a role in the scattering properties of aerosols (Fig. 6i, $r^2 = 0.32$).

On average, Sevilleta is a very low concentration aerosol environment. The percent frequency of occurrence histogram shows a peak frequency of 39% (τ_{a500}= 0.07), which declines rapidly (<2% for optical depths >0.2) (Fig. 6f). The Angstrom parameter histogram suggests a variety of aerosol types (Fig. 6g). Approximately 5% of the daily averaged α's have values less than 0.5 indicating that fine particles dominate the observed scattering effects. The most probable α is approximately 1.3, which is a typical value assumed for mid-latitude rural conditions. Less than 10% of the observations exceed 2.0 that would likely be caused from dominance of accumulation mode aerosol emissions generated by regional wildfires in the nearby mountains.

H.J. Andrews, Oregon

The H. J. Andrews Experimental Forest, a US Forest Service/ Long Term Ecological Research Reserve (LTER) forestry research reserve, is located in Oregon's central Cascade Mountains approximately 250 km east of the Pacific ocean. The landscape is highly dissected by streams and small rivers in narrow valleys with sharp ridgelines. Regionally the elevation ranges from 450 m to 1600 m. The Cimel site is located on a ridgeline (latitude 44 15' N, longitude 122 9' W) at 827 m and is typically not influenced by local mountain-valley inversions. The dominant natural vegetation is Douglas Fir in a patch work of old growth, clear cuts and re-growth. Outside the reserve, little old growth remains, the landscape being dominated by re-growth in various stages of development. Regional precipitation is variable being dependent on Pacific storms modified by orography. Typically this ranges from 2000 to 3000 mm annually within the watershed,

and the Cimel site averages 2290 mm [*Bierlamaier and McKee*, 1989]. Precipitation falls primarily from October through May with a three to four month dry season the remainder of the year. Sources of aerosols are expected from local and regional wild and prescribed fires during late summer and fall. Biomass burning from agricultural grass fields in the fall and industrial/urban aerosols are transported from the Willamette Valley 100 km upwind and possibly from California's Central Valley. Long range transport from Asian dust sources has been observed. On a geological time scale, volcanism in the Cascade range is likely. No published aerosol studies have been conducted in this region.

The meteorology is dominated by a strong westerly flow off the Pacific Ocean ~ 250 km to the west. The flow is particularly strong from December through March when most of the precipitation falls. From June through September, blocking high-pressure ridges can develop preventing transport of Pacific origin aerosol. Low level thermal lows beginning in California's central valley develop northward into Oregon and the Pacific Northwest increasing the influence of local and regional sources on aerosol loading during stagnant conditions. Rare midwinter arctic high-pressure systems can affect the region.

The LTER has maintained a seasonal AERONET site since 1994 from ~ June-October. Extensive cloudiness and inaccessibility in the winter precludes measurements throughout the year. H.J. Andrews is characterized by aerosol optical properties typical of mid latitude maritime influenced background locations (Figure 7, Table 5). At 500 nm monthly averaged aerosol optical depth is low for all months; however, the lowest values of 0.04 occur with the onset of the rainy season and clean Pacific air. Midsummer means approach 0.10 (Fig.7a). Episodes of biomass burning emissions are evident during the dry season and indications of smaller particles are shown by slightly higher Angstrom parameters during this time. The 6-month mean τ_{a500} is 0.06.

Elevated τ_{a500} at H.J. Andrews is highly variable from year to year (Fig.7c), which is dependent on the intensity and duration of the July through September dry season. Agricultural burning of grass fields in the Willamette Valley raised the instantaneous τ_{a500} to nearly 1 on several occasions in August and September of 1999. Daily τ_{a500} for all years (Fig. 7d) showed a small variation from 0.03 to approximately 0.2 owing to lack of strong regional aerosol sources. Episodic smoke events due to regional forest fires raised the τ_{a500} above 0.2 on only 23 days in four years (Fig. 7d).

The aerosol optical depth frequency distribution clearly illustrates that nearly 75% of the τ_{a500} observations are below 0.1 and half of those below 0.05 (Fig. 7f). The frequency distribution of the Angstrom parameter α shows a broad range 0.3 to 2.2 indicating a wide range in particle size; however, the dominant range is 1.3 to 1.8 which includes values expected for rural background conditions (Fig. 7g). The data were partitioned into two meteorological time periods, June, July and August, the driest period and September, October and November, the onset of the wet season. The wet season has a greater frequency of lower optical depths than the dry season which would be expected from an increased flow of clean Pacific air masses over the site. Correspondingly the central tendency of the Angstrom parameter is shifted approximately 0.1 higher for the dry period owing to local or regional aerosol production from biomass burning. Approximately 30% of the points in the wet season have an average Angstrom parameter less than 1 and optical depths less than 0.1. We are unable to determine whether this is due to cloud contamination, marine aerosol or dust, however, marine aerosol is likely. Approximately 10% of the dry season observations fall into this category.

Precipitable water retrievals clearly show a systematic decline from July and August (2 to 2.5 cm) to minimums of ~0.5 cm in November and December despite the onset of the wet season (Fig. 7e). This apparent discrepancy may be partially explained by the

reduction in air temperature of approximately 20°C from August to December reducing significantly the capacity of the atmosphere to hold water. Additionally measurements are only made during fair weather conditions thus no information is available during the more frequent precipitation events of the wet season. The aerosol optical depth and PW are nearly uncorrelated (r^2 ~0.04), (Fig. 7i).

Cape Verde

Sal Island, Cape Verde (16° 45'N, 22° 57'W) is located approximately 600 km west of Dakar, Sénégal, in the outflow area of Saharan dust from West Africa. The nearest town of ~6,000 residents is about 3 km away from the measurement site. The dominant easterly wind direction is well known to be influenced by easterly waves, Saharan storms and associated dust outbreaks [*Carlson and Prospero*, 1972; *Schutz*, 1980]. A 4-year measurement record (1994-1999) has been collected as part of the PHOTON network, with a total of 726 daily averages analyzed (Fig. 8).

Monthly averages of τ_{a500} and α for the whole period of observations are shown in Figures 8a and 8b. The aerosol optical depth for this site is high throughout the year with elevated values in summer (from May to September) and secondary peaks in winter (January-February). April and October correspond to the lowest aerosol contents. Monthly means range between 0.26 (April) to 0.68 (June) (Fig. 8a, Table 6). Mean monthly values of τ_{a500} show significant inter-annual variability of aerosol optical depth. The Angstrom parameter α is typically below 0.5 (Fig. 8b). The high aerosol loading in summer with corresponding low α indicates that dust dominates the aerosol regime associated with frequent Saharan dust outbreaks. This annual cycle has been observed by several authors (see e.g., the early study by *Jaenicke and Schütz*, [1978]). It is associated with dust transported over long distances at an altitude typically between 2-5km.

Satellite data, like TOMS [*Chiapello et al*., 1999a] also indicate a seasonal pattern in aerosol loading with a maximum in summer time. This time evolution is quite consistent over the 4 years of measurements (Fig.8c). It is noted that dust concentrations at ground level, have a minimum during the same period [*Chiapello et al*., 1995].

The situation is more complex in wintertime. The relative high aerosol content can still be associated with dust transported at a lower altitude and coming from other sources as observed by *Chiapello et al*. [1997]. The contribution of the marine sea salt when the optical thickness is low (around 0.2) may also represent up to 30% of the total optical thickness [*Chiapello et al.,* 1999b].

Daily average values of τ_{a500} for all years show very large day to day variation (Fig.8d). A histogram of τ_{a500} is wide with a modal value of about 0.20 (Fig. 8f).

Unfortunately, there is no obvious method to distinguish sea salt aerosols from dust in our data since both aerosol types are associated with the low Angstrom parameters (Fig.8g and 8h). On the other hand, there is obviously in late winter-early spring, a contribution from a different aerosol type as reported by the higher values of the Angstrom parameter; monthly averages in this season are around 0.8-0.9 (i.e. March-May of 1995) with some individual cases larger than 1.0 (Fig. 8g). Chemical analysis from samples performed at ground level and air mass trajectory analysis [*Chiapello et al.*, 1999b] suggest that there is possible pollution by sulfates coming from urban and industrial regions in North Africa. However, it is difficult to conclude about the origin and type of aerosols during this period. For the entire data set the probability distribution of α is narrow with a modal value of ~0.1-0.3 (Fig. 8g).

As expected, the precipitable water is a maximum during summer months (Fig.8e), that corresponds to the northern most position of the ITCZ (June-September) and

minimum in the dry season (January-April). There is no correlation between precipitable water and aerosol optical depth (Fig. 8i).

To conclude, the aerosol content over Cape Verde is high all year. Very high values in summer can clearly be attributed to desert dust but the contributions of other aerosol sources may be significant during the other seasons.

Banizoumbou, Niger

Banizoumbou, Niger (13°45'N, 02°39'E) is located in the Sahel region, between the Sahara desert to the north and the Sudanian Zone to the south. The aerosol climate is influenced by the Harmattan, an easterly or northereasterly wind laiden with dust transported from the Sahara. *Prospero* [1981], *d'Almeida* [1986], and *Pye* [1987] identify several aerosol source regions and associated transports that contribute to the Harmattan. Banizoumbou is mainly influenced by sources located in Niger, south Algeria, Libya and Chad. *N'Tchayi et al*., [1997]has shown that, in addition to the sources located in the Sahara, the semi-arid Sahelian region is also a major source of dust. The dust loading in the atmosphere depends on the meteorological and surface conditions in the source region. High winds and strong convective processes are needed for lofting particles in the atmosphere for long range transport. The area can also be affected by the presence of biomass burning aerosols. The savanna vegetation is characteristic of the Sudanian zone and fire activities are important in the zone during December to February. Biomass burning aerosols have a size distribution with a significant fraction in the accumulation mode (a few tenths of microns), while dust particles generally present larger sizes near the sources that result in smaller Angström exponents (Fig. 9 and Table 7).

The climate of the area is characterized by a single and usually short rainy season and depends on the presence of the Inter Tropical Convergence Zone (ITCZ). The ITCZ corresponds to the transition zone between dry airmasses coming from the north and moist air coming from the equatorial regions. As expected, the PW increases when the ITCZ is moving northward and is a maximum (Fig. 9e) when the ITZC reaches the area, ranging from 1.0 cm in January up to 4.0 cm in June through September.

Seasonal trends in τ_{a500} are not apparent from these data however values are high all year (larger than 0.2) with primary peaks in October, February and April (Fig. 9a and 9c). The distribution (Fig. 9f) has a peak value at 0.2-0.4 and the yearly average is approximately 0.48 (Table 7). These maximums are associated with very small Angström exponents (less than 0.15) which indicates that dust is the main contributor to the optical thickness (Fig. 9b and 9g). There are several secondary peaks in January, March, June and July, associated with either small or large (relative to the average conditions) Angström exponents, less than 0.05 in June and ~0.3 in January. The higher values of the Angstrom parameter in January correspond to the presence of biomass burning aerosols. It is more obvious in December when α reaches its maximum (0.45). August and September are relatively clean months due to the scavenging of the atmosphere by precipitation.

The prevailing aerosol type is clearly dust coming from the Saharan/Sahelian zone and transported over the area. The largest values of τ_{a500} are associated with small values of alpha (Fig. 9h) that is characteristic of the presence of dust. Over our 2 years of measurements, the turbidity is always significantly above background levels. From March through June, the very low Angström exponent confirms the presence of dust. In December and January, there is clearly a second aerosol type that contributes to the turbidity as confirmed by the higher values of the Angström exponent. At that time,

aerosols resulting from biomass burning activities are then mixed with dust depending on the wind direction. In the rainy season, from late July to early October, in addition to dust background conditions, humidity effects may contribute to the atmospheric turbidity but there is no correlation between precipitable water and optical thickness (Fig.9i).

Mongu

Mongu, Zambia ($15^0$15' S, 23^0 09' E, 1107 m elevation) is located in west central Zambia on the eastern edge of the Zambezi River floodplain. The local regional vegetative cover is grassland, seasonal marsh, and cropland in the floodplain and principly miombo woodland on the higher ground. The annual variation in the aerosol optical depth is dominated by the practice of agricultural biomass burning (Fig.10a, Table 8), which occurs primarily during the second half of the dry season and includes the beginning of the wet season (August-November). Average rainfall for the 7 months dry season of April - October is less than 8% of the mean annual total (969 mm). Compared to the biomass burning season in South America (for example: Cuiaba, Fig.11a) which reaches a maximum for approximately 2 months (August-September), the burning season is longer (3-4 months) in the savanna region of south central Africa near Mongu. *Scholes et al.* [1996a] estimated the geographical distribution of the amount of biomass burned, utilizing satellite estimates of burned area [*Justice et al.,* 1996] in 1989 south of the equator, and showed much higher amounts to the north of Zambia with low amounts south of Zambia. This is primarily due to the north-south gradient in rainfall and thus vegetation production. *Scholes et al*. [1996b] combined these biomass burned estimates with emission factors dependent on fuel type to show a strong N-S gradient in trace gas production for southern Africa south of the equator. The frequency of occurrence of high aerosol loading of absorbing aerosols from biomass burning has been measured from

satellite retrievals made in the UV wavelengths from the TOMS instrument [*Herman et al*., 1997]. These data show that the region with the most prevalent heavy smoke is north of Zambia, corresponding to the region with higher biomass.

Gartsang et al. [1996] analysis of trajectories over southern Africa showed 5 aerosol transport modes that are likely to occur frequently with transport possible in all major directions from and to western Zambia. They also noted that subsidence from anticyclonic circulation is a dominant feature during much of the biomass burning season with 4 stable vertical layers identified in the troposphere. The two layers most important in controlling aerosol vertical and horizontal transport occurred at 1.5 km above the surface (top of the diurnal mixing layer) which is broken every 5-7 days, and a very persistent layer at 3.5 km above the surface which is subsidence induced.

From the monthly means of τ_{a500} (Fig. 10c), it is noted that there is significant inter-annual variability in the length of the biomass burning season. For example, the average November τ_{a500} is nearly 3 times greater in 1996 than in 1995. This variation is due in large part to the timing of when rainfall starts increasing at the beginning of the wet season, but is probably also due in part to the predominant circulation modes and trajectories in a given year. Daily average values of τ_{a500} for all 4 years (Fig. 10d) show very large day to day variations especially in 1996 and 1997 peak burning season months, thus showing the influence of variable air trajectories. The daily average values of the precipitable water (Fig.10e) show that they are typically low in June-July at 0.5-1.5 cm, while in November the PW values are much higher ranging from 2.5-3.5 cm, due to the southward advance of the Intertropical Convergence Zone (ITCZ). The daily values of PW in August and September show a large amplitude range, suggesting trajectory variations in this season. The relationship between PW and τ_{a500} (Fig. 10i) shows that over the total 6 month season, there is not a strong relationship, but it is noted that there is

a lack of very high τ_{a500} cases (>0.8) for PW < 1.0 cm. If only peak burning season months of August-October were shown, there would be a somewhat stronger relationship between τ_{a500} and PW because many of the values of low τ_{a500} with high PW (2-4 cm) occur in November 1995 and December 1996 when PW is high and rains have already commenced washing out some aerosol and suppressing more burning. Thus trajectories from the north in August-September, which have higher PW amounts, sometimes advect air with higher smoke aerosol concentrations from these regions with higher biomass and higher emissions [*Eck et al*., 2000]. The frequency of occurrence histogram of τ_{a500} (Fig. 10f) shows a skewed distribution with a peak at 0.1 to 0.2 and a steadily decreasing frequency at higher optical depths which results from the smoke from biomass burning.

The relationship between Angstrom wavelength exponent (α) and τ_{a500} is shown in Figure 10h. One of the main features of this plot is high values of α at high τ_{a500} which is characteristic of small particle smoke aerosols which typically have accumulation modal radius values of 0.13-0.15 μm of the log-normal volume size distribution [*Remer et al*., 1998; *Reid et al*., 1998]. Comparison of α versus τ_{a500} measurements for smoke from boreal forest fires in Canada [*Markham at al*., 1997] shows a striking similarity to the Mongu data. For both locations the α value tends to asymptote at a value of approximately 1.8 thus suggesting similar size smoke particles from vastly different environments and thus fuel types. A similar feature is seen for South American biomass burning smoke (see Cuiaba Fig. 11h) with α values typically between 1.6 and 2.0 for τ_{a500} values over 0.8. This contrasts with the measurements of *Liousse et al*. [1995] for savanna smoke at Lamto, Ivory Coast where α values were found to range from 0.84 for aged smoke to 1.42 for fresh smoke. However, in that West African site it is possible that

the relatively low α values may be influenced by the presence of Sahelian/Saharan dust as a secondary aerosol type.

Some of the lower values of α at low τ_{a500} for Mongu, may be due to windblown soil aerosol of much larger size particles either from local soils or from long range transport from distant sources such as dry lake beds like Etosha Pan and Makgadikgadi Pan to the south-west and south of Mongu, respectively. The multiyear means of average monthly α values show very little seasonal variation (Fig. 10b) from June through October, however the value in December is ~0.7 lower, perhaps due to episodes of dust transport, or possibly due in part to cloud contamination. It is noted that the June monthly mean α is equal to the September mean (Fig. 10b) suggesting that the aerosol in June may be dominated by smoke from small cooking fires prior to the peak biomass burning season (landscape fires) of late July-October. The frequency of occurrence histogram of daily average α (Fig.10g) at this site shows a relatively narrow peak at 1.6-2.0, again due to the dominance of smoke aerosols for the months of June-November.

Cuiaba, Brazil

Cuiaba, Brazil is located in central South America, immediately to the south of the Amazon Basin, ($15^0$33' S, 56^0 4' W, 250 m elevation) in a region that is cerrado (savanna) vegetation, which has been largely converted to agricultural land. Annual burning of these cerrado and agricultural lands is a common practice which occurs primarily at the end of the dry season in August-September but which may continue into October-November depending on the timing of the rainfall. In addition to biomass burning of cerrado vegetation in the region surrounding Cuiaba, there is also biomass burning of tropical forest to the north (~500 km) and burning of grazing grasslands in the Pantanal (the world's largest seasonally flooded wetland) to the south (~100 km). *Remer*

at al. [1998] has shown from trajectory analysis that smoke from these different regions is advected over Cuiaba during the burning season and that these differing trajectories may result in the advection of smoke aerosol with somewhat differing size distributions and that total precipitable water may also vary. The CIMEL sun/sky radiometer site was located ~10 km north of the city of Cuiaba and therefore may also be influenced by some urban/industrial aerosol production.

A detailed discussion of the seasonality of the aerosol optical depth, Angstrom wavelength exponent, and precipitable water for Cuiaba is given in [*Holben et al.*, 1996] for measurements made in 1993 and 1994. Here we present an analysis of data with 1995 added to the previous 2 years and emphasize a discussion of average seasonality and inter-annual variations.

The 3 year average monthly variation in τ_{a500} at Cuiaba (Fig. 11a, Table 9) clearly shows that the peak in smoke concentrations from biomass burning aerosols occurs in August and September. However, τ_a does not return to background levels until December, thus there is some local burning and/or advection of smoke from other regions in the months of October-November which is the beginning of the rainy season. During the 5 months dry season at Cuiaba, May through September, only ~9% of the total annual average precipitation (1373 mm) occurs. Decreases of τ_a in October-November with the onset of rains (aerosol washout and less flammable fuels) vary from year to year during 1993-1995 (Fig.11c). For example, the October monthly average τ_{a500} for 1994 is nearly double the value for 1993. The daily variability of τ_{a500} during the burning season at Cuiaba can be quite large (Fig.11d). For example during August-September 1995 the range is from ~0.3 to 2.4, as a result of air trajectories coming from burning regions on some days and on other days the trajectories may be from a direction with very few fires. The average τ_{a500} for the non-burning season months of June, December, and January are

low and consistent, suggesting a relatively stable and low background τ_{a500} of ~0.15. The frequency of occurrences histogram of daily average τ_{a500} (Fig.11f) is skewed with peak frequency occurring below 0.25 representing conditions approaching monthly average background conditions and a large number of higher values due primarily to biomass burning with a peak value of ~2.3.

The aerosol particle size distribution has a significant seasonal change at Cuiaba, as is indicated by strong seasonal variation in the Angstrom wavelength exponent (α) (Fig. 11b). Angstrom wavelength exponent values average ~0.6-0.7 for non-burning season months, while for the peak burning season months of August-September, the average is 1.7-1.8. As shown in Fig.10h there is a strong relationship between τ_{a500} and α at Cuiaba, with the majority of α values for $\tau_{a500} > 0.6$ falling in the range 1.5-2.0. This is somewhat similar to the α values for biomass burning smoke in Mongu, Zambia (Fig.10h) thus implying similar aerosol size distributions for the smoke in these two vastly different regions. *Remer et al.* [1998] has found the accumulation mode particle size of the log-normal volume size distribution for biomass burning smoke in Cuiaba to be typically about 0.13 um modal radius, but with a range of 0.12-0.17 um. *Kotchenruther and Hobbs* [1996] found the humidification factor of South American biomass burning aerosols to be rather small (~1.05-1.35), suggesting little influence of relative humidity on aerosol size and optical properties. This may explain in part why the α values of smoke from biomass burning are so similar in such widely differing environments as African savanna (see Mongu, Fig.10h), boreal forest fires in Canada [*Markham et al.*, 1997], and South American tropical forest and savanna [*Holben et al.*, 1996].

The α values in Cuiaba at lower τ_{a500} (<0.4) show a wide range from ~0.1 to 2.2, thus suggesting differing aerosol types on different days. However, in contrast to Mongu, which shows monthly average α values which are equal for burning season and non-

burning season alike, there are more cases of lower α values in Cuiaba in non burning season months, resulting in lower monthly average α values indicative of a predominant influence of larger aerosol particles. The frequency of occurrences histogram of α (Fig. 11g) shows a skewed distribution with peak frequency at 1.6-1.8 resulting from biomass burning aerosols dominated by accumulation mode particles. A significant number of occurrences from 0.8 to 1.4 are representative of bimodal size distributions with varying relative concentrations of accumulation mode versus coarse mode aerosols.

The seasonal variation of precipitable water at Cuiaba (Fig. 11e) ranges from 1-3.5 cm in June-July at the middle of the dry season to 4.0-5.5 cm in January in the mid-wet season. Significant day to day variability in PW occurs, associated with air mass trajectories from different source regions. However, there is very little correlation between τ_{a500} and PW for the entire combined wet plus dry season data set (Fig. 11i). In contrast, however, *Remer et al*. [1998] found some correlation between PW and τ_{a500} for Cuiaba when primarily burning season data are analyzed. This occurs since PW acts as a tracer of air mass origin and since the highest smoke aerosol concentrations originate in the forest burning regions to the north which also have the highest PW concentrations.

Thompson, Manitoba, Canada

Thompson, Manitoba ($55^0$47' N, $97^0$50' W, 218 m elevation) is located near the northern ecotone of the boreal forest zone of central Canada. The local land cover is dominated by forest of three species: black spruce, jack pine, and aspen with numerous lakes and ponds present. The climate is characteristic of a high latitude mid-continental geographic location, with long severe winters and heavy snow pack. The warm spring and summer seasons experience a high degree of variability in precipitation amount, which results in very large interannual variations in forest fire frequency and total area

burned [*Stocks*, 1991]. The seasonal variation and interannual variability in aerosol optical depth is dominated by the amount of biomass burning aerosols produced from forest fires (Fig. 12a-12c, Table 10). Data for June 1994 and most of July 1994 were measured at a site ~35 km northwest of Thompson since the Thompson monitoring site was not established until late July 1994. It is noted that 1994 was the driest year on record for this region, resulting in numerous and widespread forest fires with heavy aerosol loading (Fig. 12d). In contrast to the years 1994 and 1995 which had numerous fires and associated biomass burning aerosols, the relatively moist years of 1997-1999 (especially 1997) had relatively little burning and therefore much lower aerosol optical depth (Fig. 12d). This time series is in relatively good agreement with satellite estimates of the area covered by heavy smoke, as estimated by the TOMS sensor [*Hsu et al*., 1999], for all of Canada from 1979 to 1998. For Canada, TOMS estimates show 1997 as having the least heavy smoke coverage of any year, while 1994 was a year of moderate to high coverage within the context of the 19 years of satellite monitoring. However TOMS data shows that for all of Canada, 1998 was a year of extensive burning while our measurements in Thompson show relatively little smoke compared to 1994 and 1995, thus suggesting that other regions of Canada experienced weather conditions more conducive to fires that year.

Although the seasonal and inter-annual variation of aerosol optical depth is dominated by biomass burning aerosols from forest fires, there are additional sources of aerosol which are present also. There is a large nickel smelting operation located in the town of Thompson, and the forest itself is a source of biogenically produced aerosols. In addition to the production of pollen in the spring, coniferous forests also produce biogenic hydrocarbons which lead to the formation of atmospheric particulates [*Kavouras et al.*, 1998]. Comparison of optical depth data from winter to early spring months for

this site in 1996 [*Markham et al.*, 1997] before biomass burning typically begins, show slightly higher values in spring which may be due in part to biogenically produced aerosols. In addition, aerosols may be advected into the region from distant source regions having different air mass characteristics. For example, *Smirnov et al.* [1996] have shown that tropical air masses influence the site of Wynward, Saskatchewan ($51^0$46' N, 104^0 12' W) about 5% of the time and that these air masses are associated with higher aerosol optical depths observed at that site (up to 0.36 at 500 nm). In Figure 12d, we see that there is large daily variability in τ_{a500} for all years except 1997 and 1999, which is due mainly to varying air mass trajectories from forest fire regions (and precipitation variability), but also, to a much lesser degree, due to long range aerosol transport from other sources. Total column integrated PW (Fig. 12e) also show significant daily variability, with high values in mid summer suggestive of air mass advection from the south and/or large scale regional convergence increasing the precipitable water. The relationship between daily average τ_{a500} and PW (Fig. 12i) shows that for days where precipitable water exceeds 2.5 cm there are very few cases of very high τ_{a500}. The days with high precipitable water are likely to have had a southerly flow component, therefore suggesting that most of the large forest fires do not occur to the south of Thompson. The frequency histogram for the daily average τ_{a500} values (Fig. 12f) shows that a large number of occurrences are observed below 0.2 and that above τ_{a500} of 0.5 there are typically only 1 to 3 days, if any, for each 0.1 τ_{a500} interval bin. This is a result of the high spatial and temporal variability of forest fire smoke, especially at high aerosol optical depths.

The relationship between daily average Angstrom wavelength exponent (α) and τ_{a500}. (Fig. 12h) shows two principal features: a wide range of α at moderate to low

aerosol optical depths (<0.4) and a relatively narrow range of α at high optical depths (>0.5). The wide range of α associated with the low optical depth cases may be due to a wide variety of aerosol types with different associated size distributions. The high α values may possibly be associated with pollution from the nickel smelting operation in town [*Markham et al.,* 1997] and low α values perhaps associated with pollen dispersal from the forests and/or combinations of other biogenic aerosols or dust from unpaved roads during dry time periods. In addition, at low τ_{a500} (<0.10), the uncertainty in τ_a measurement of 0.01-0.02 can result in large errors in the computed values of α [*O'Neill et al.,* 2000]. The α values of 1.4-2.1, which occur at high optical depths (τ_{a500}>0.5), are typical of biomass burning values (see the Mongu, Zambia and Cuiaba, Brazil sections). These α values result from accumulation mode dominated smoke aerosols with typical log-normal volume size distribution radius values of 0.13 to 0.17 μm for the accumulation mode. The range in α for biomass burning aerosols is dependent in part on the type of fuels burned, the type of combustion (flaming or smoldering), and the aging processes of the aerosol as it is transported [*Reid et al.,* 1999]. Monthly average values of α shown in Figure 12b, reach a maximum in July and August due in part to the presence of biomass burning aerosols in those months, but also perhaps due to less pollen and other large particle aerosols produced in mid summer than in May-June when biomass burning aerosols are also present. The frequency of occurrence histogram of α (Fig. 12h) also shows the wide range of values observed at this site with a peak occurring at the 1.6-1.8 α range bin.

Conclusion

Monthly statistics for aerosol optical depth (τ_{a500}), precipitable water and angstrom exponent have been computed from AERONET direct sun observations of two or more

years at sites representing biomass burning aerosols, background aerosols, desert aerosols and aerosols generated in urban landscapes. The results clearly show seasonal dynamics in aerosol loading, type and precipitable water.

Background levels of aerosols, which we define as τ_{a500} less than 0.10, were observed at almost all sites but varying frequencies. Mauna Loa Observatory located in the mid Pacific Ocean above the marine boundary layer, exhibited the lowest values <0.02, only slightly perturbed during the spring Asian dust season plus transport of Asian pollution and infrequent emissions from local volcanism. Background levels may also be observed at GSFC mainly during winter months. Sevilleta and H.J. Andrews, representing dry and wet mid latitude regions, showed only weak increases in aerosol loading above background during summer months. Similarly the seasonal sites in the Boreal forest and tropical woodlands largely exhibited background levels prior to dry season biomass burning, predictably increasing monthly averaged τ_{a500} to 1.2 in the tropics but with very large inter-annual variability in the boreal forests. The greater inter-annual varibaility in the Boreal forest site was caused by the influence of wildfires while the tropical sites were influenced by anthropogenic fires.

The West African sites influenced by desert dust, Cape Verde and Banizoumbou, were above background levels for all months. A bimodal aerosol optical depth distribution (winter and summer peaks) was observed at Cape Verde as it lies downwind of the extensive dust source regions. Dust particles are the dominant aerosol type at the island site despite its oceanic location. τ_{a500} monthly averages range between 0.2 to 0.7 year around, lower than the high drought observations of the mid 80's. Banizoumbo is influenced by elevated levels of dust and biomass burning during the winter season and dust for much of the rest of the year as indicated in the dramatic changes of the angstrom

exponent. Again these values are lower than the peak values of the drought years of the mid 80's.

Biomass burning constitutes significant increases in monthly loading and order of magnitude daily spikes for tropical sites. Because of their anthropogenic nature associated with land cover change, the spikes are a predictable signal in the aerosol loading during August through September in both South America and southern Africa. The Angstrom parameter typically ranges from 1.7 to 2.1 indicating very small particles generated by the combustion processes. Correspondingly wildfire biomass burning in the northern hemisphere mid latitudes typically occurs in the summer months peaking in August and September however the extent is highly variable depending on local meteorological and fuel loading conditions. Daily τ_{a500} at these sites can range from background conditions to well over 1.

All northern midlatitude continental sites showed seasonal cycles of warm season peaks and cool season low values of τ_{a500}. Particularly dramatic was Goddard Space Flight Center with a July τ_{a500} average of ~0.5. This was well correlated with precipitable water suggesting that humidification contributes significantly to the aerosol burden while polar continental airmass trajectories bring air with low aerosol optical depth and low precipitable water. Likewise the midlatitude circulation slows during summer months allowing aerosol concentrations to build. Additionally more hours of sunlight can enhance photochemical smog. In all our non-dust sites, there was a positive correlation between the precipitable water and aerosol optical depth. For tropical biomass burning sites, this is a meteorological-land use phenomenon largely associated with the coincidence of source regions. The mid latitude sites studied likely represent a significant regional biogenic emission source combined with humidification and swelling of sulfate and biogenic aerosols as higher temperatures increase the atmosphere’s

capacity to hold water vapor. US mid Atlantic urban aerosols have been shown to be strongly hygroscopic while biomass burning aerosols in Brazil are very weakly hygroscopic [*Kotchenruther et al*., 1999].

The result of these observations clearly documents a pulse of aerosols with large α at many of our globally distributed sites in August and September. Although this network provides point observations, the diurnal daily and long-term observations will yield important details of aerosol optical properties to augment the spatial observations afforded by other aerosol networks and satellite retrievals. Thus in the near future we anticipate these data will provide part of a synthesis for a globally balanced assessment of the impact of aerosols on the planet's radiation balance.

Acknowledgments

This paper represents considerable effort over many years by numerous people that have collectively developed the AERONET program and allowed analysis of the data presented here. Our thanks to the individual site managers who have maintained an active interest in the project and resulted in long-term observations including Fred Bierlmaier (H.J. Andrews), Doug Moore (Sevilleta), Steve Ryan(MLO), Mukufute M. Mukelabai (Mongu), Jose Chagas (Cuiaba), Alfredo Pereria (Brazil network), Bento de Silva (Brasilia) , O. Manga, J.L. Rajot , E.F. Santos Soares, A. Werem (PHOTON sites), Ray Johnson (Thompson), S. Khudulmur and Enkhtuvshin (Dalanzadgad), Judd Welton and David Bates (Dry Tortugas), Mark Yarborough (Lanai), Miguel Rivas(Arica), Jeff Chilton, Naval Air WarfareCenter, Point Mugu (San Nicholas), T.O. Aro (Ilorin), Mike Willis(Bahrain), Paula Palachek (Waskesiu), Mike Snyder (Bondville), Alain Royer and Amadou Bokoye (CARTEL, Université de Sherbrooke, Sherbroke, Québec, Canada) and Francesco Cappellani (Ispra). Our thanks to our funding sources that had the foresight to

support this international collaborative activity, these include Dr. Michael King EOS Senior Project Scientist, Dr. Diane Wickland and Dr. Robert Curran of NASA Headquarters for support of AERONET, M. Alain Podaire (CNES) and Dr. Daniel Vidal-Madjar (CNRS) for support of PHOTON, Division of Environmental Biology (DEB) of NSF for support of the LTER sites and Dr. Philippe Teillet and Mr. Gunar Fedosejevs of the Canada Centre for Remote Sensing for supporting AEROCAN (the Canadian AERONET component coordinated by the CARTEL group of the Université de Sherbrooke), the Department of Energy's Atmospheric Radiation Measurement program for support of the Southern Great Plains site and NASA/EOS MODIS contract number NAS5-31363 for support for the Dry Tortugas site. Finally our thanks to Dr. Ellsworth Dutton and Dr. Russ Schnell of NOAA/CMDL for their long term support for our calibration effort at Mauna Loa, Hawaii.

References:

Andreae, M.O., 1996. Raising dust in the greenhouse. Nature, Vol. 380, PP 389-390.

Barnes, J.E. and D.J.Hofmann, Lidar measurements of stratospheric aerosol over Mauna Loa Observatory, *Geophys.Res.Lett., 24,* 1923-1926, 1997.

Ben Mohamed, A., J.P.Frangi, J.Fontan, and A.Druilhet, Spatial and temporal variations of atmospheric turbidity and related parameters in Niger, *J.Appl.Met., 31,* 1286-1294, 1992.

Bierlmaier, F.A. and A.McKee, Climatic summaries and documentation for the primary meteorological station, H.J. Andrews Experimental Forest, 1972 to 1984. Gen. Tech. Rep. PNW-242, Portland, OR: U.S. Department of Agriculture, Forest Service, Pacific Northwest Research Station, 56 pp., 1989.

Bigelow, D.S., J.R.Slusser, A.F.Beaubien, and J.H.Gibson, The USDA ultraviolet radiation monitoring program, *Bull.Amer.Meteor.Soc., 79*, 601-615, 1998.

Bruegge, C.T., J.E. Conel, R. O.Green, J.S.Margolis, R.G.Holm, and G.Toon, Water vapor column abundance retrievals during FIFE. J. Geophys. Res. 97(D19):18,759-18768, 1992.

Bryson, R.A., Air masses streamlines, and the Boreal forest, *Geogr.Bull., 8*, (3), 228-269, 1966.

Carlson, T.N., and J.M.Prospero, The large-scale movement of Saharan air outbreaks over the northern equatorial Atlantic, *J.Appl.Meteorol., 11*, 283-297, 1972.

Chiapello, I., G. Bergametti, L. Gomes, B. Chatenet, F. Dulac, J. Pimenta, and E. Santos Soares, An additional low layer transport of Sahelian and Saharan dust over the northeastern Tropical Atlantic, *Geophys.Res Lett., 22*, 3191-3194, 1995.

Chiapello, I., G.Bergametti, B.Chatenet, P.Bousquet, F.Dulac, and E.Santos Soares, Origins of African dust transported over the North-Eastern Tropical Atlantic, *J.Geophys. Res., 102*, 13701-13709, 1997.

Chiapello, I., J.M.Prospero, J.Herman, and C.Hsu, Nimbus-7/TOMS detection of mineral aerosols over the North Atlantic ocean and Africa, *J.Geophys.Res., 104*, 9277-9292, 1999a.

Chiapello, I., G.Bergametti, B.Chatenet, F.Dulac, C.Moulin, A.Vermeulen, C.Devaux, I.Jankowiak and E.Santos Soares, Contribution of the different aerosol species to the aerosol optical depth over the Northeastern Tropical Atlantic, *J.Geophys.Res., 104*, 4025-4033, 1999b.

Dahm, C.N., and D.I.Moore, The El-Niño/Southern oscillation phenomenon and the Sevilleta long- term ecological research site, in LTER Report, LTER Climate Committee, Ed. by D.Greenland, LTER Publication No.18, pp.12-20, 1994.

D'Almeida, G.A., A model for Saharan dust transport, *J.Clim.Appl.Meteor., 25*, 903-916, 1996.

D'Almeida, G.A., On the variability of desert aerosol radiative characteristics, *J.Geoph. Res., 92*, 3017-3026, 1987

Dutton, E.G., Aerosol optical depth measurements from four NOAA/CMDL monitoring sites, in *Trends '93: A compendium of data on global change*, edited by T.A.Boden, D.P.Kaiser, R.J.Sepanski, and F.W.Stoss, pp.484-494, Carbon Dioxide Information Analysis Center, Oak Ridge National Laboratory, Oak Ridge, Tenn., U.S.A., 1994a.

Dutton, E.G., P.Reddy, S.Ryan, and J.J.DeLuisi, Features and effects of aerosol optical depth observed at Mauna Loa, Hawaii: 1982-1992, *J.Geophys.Res., 99*, 8295-8306, 1994b.

Dutton, E.G., J.J.DeLuisi, and A.P.Austring, Interpretation of Mauna Loa atmospheric transmission relative to aerosols, using photometric precipitable water amounts, *J.Atmos.Chem., 3*, 53-68, 1985.

Eck, T.F., B.N.Holben, D.E.Ward, O.Dubovik, J.S.Reid, A.Smirnov, M.M.Mukalabai, N.C.Hsu, N.T.O'Neill, and I.Slutsker, Characterization of the optical properties of biomass burning aerosols in Zambia during the 1997 ZIBBEE experiment, *J. Geophys. Res*., 2000 (in press).

Eck, T.F., B.N.Holben, J.S.Reid, O.Dubovik, A.Smirnov, N.T.O'Neill, I.Slutsker, and S.Kinne, The wavelength dependence of the optical depth of biomass burning, urban and desert dust aerosols, *J.Geoph.Res., 104*, 31,333-31,350, 1999.

Forgan, B.W., J.J.DeLuisi, B.B.Hicks, and E.N.Rusina, Report on the measurements of atmospheric turbidity in BAPMoN, *WMO Rep*., N 94, 77 pp., Geneva, 1993.

Flowers, E.C., R.A.McCormick, and K.R.Kurfis, Atmospheric turbidity over the United States, 1961-1966, *J.Appl.Met., 8*, 955-962, 1969.

Garstang, M., P.D. Tyson, R. Swap, M. Edwards, P. Kallberg, and J.A. Lindesay, Horizontal and vertical transport of air over southern Africa, *J.Geophys.Res., 101*, 23721-23736,1996.

Gueymard, C., Analysis of monthly average atmospheric precipitable water and turbidity in Canada and northern United States, *Solar Energy, 53*, 57-71, 1994.

Guschin, G.P., The methods, instrumentation and results of atmospheric spectral measurements (in Russian), 200 pp., Gidrometeoizdat, Leningrad, 1988.

Herber, A., L.W.Thomason, V.F.Radionov, and U.Leiterer, Comparison of trends in the tropospheric and stratospheric aerosol optical depths in the Antarctic, *J.Geoph.Res., 98*, 18,441-18,447, 1993.

Herman, J.R., P.K.Bhartia, O.Torres, C.Hsu, C.Seftor, and E.Celarier, Global distribution of UV-absorbing aerosols from Nimbus 7/TOMS data, *J.Geophys.Res., 102*,16911-16922,1997.

Holben, B.N., T.F.Eck, I.Slutsker, D.Tanre, J.P.Buis, A.Setzer, E.Vermote, J.A.Reagan, Y.J.Kaufman, T.Nakajima, F.Lavenu, I.Jankowiak, and A.Smirnov, AERONET - A federated instrument network and data archive for aerosol characterization, *Rem.Sens.Env., 66(1)*, 1-16, 1998.

Holben, B.N., A.Setzer, T.F.Eck, A.Pereira, and I.Slutsker, Effect of dry season biomass burning on Amazon basin aerosol concentrations and optical properties, J.Geophys.Res., 101, 19465-19481, 1996.

Holben, B.N., T.F.Eck, and R.S.Fraser, Temporal and spatial variability of aerosol optical depth in the Sahel region in relation to vegetation remote sensing, *Int.J.Rem.Sen., 12*, 1147-1163, 1991.

Hsu, N.C., J.R Herman, J.F. Gleason, O. Torres, and C.J. Seftor, Satellite detection of smoke aerosols over a snow/ice surface by TOMS, *Geophys.Res.Lett., 26*, 1165-1168, 1999.

Jaenicke R. and L.Schütz, Comprehensive study of physical and chemical properties of the surface aerosol in the Cape Verde Islands region, *J.Geophys.Res., 83*, 3585-3599, 1978.

Jinhuan, A., and Y.Liquan, Variation characteristics of atmospheric aerosol optical depths and visibility in North China during 1980-1994. *Atm.Environ., 34*, 603-609, 2000.

Justice, C.O., J.D.Kendall, P.R.Dowtry, and R.J.Scholes, Satellite remote sensing of fires during the SAFARI campaign using NOAA advanced very high resolution radiometer data, *J.Geophys.Res., 101*, 23851-23863, 1996.

Kavouras, I.G., N.Mihalopoulos, and E.Stephanou, Formation of atmospheric particles from organic acids produced by forests, *Nature, 395*, 683-686, 1998.

Kaufman, Y.J., D.Tanre, H.R.Gordon, T.Nakajima, J.Lenoble, R.Frouin, H.Grassl, B.M.Herman, M.D.King, and P.M.Teillet, Passive remote sensing of tropospheric aerosol and atmospheric correction for the aerosol effect, J.Geophys.Res., 102, 16,815-16,830, 1997.

Kaufman, Y.J., and R.S.Fraser, Light extinction by aerosols during summer air pollution, *J.Clim.Appl.Met., 22*, 1694-1706, 1983.

King, M.D., Y.J.Kaufman, D.Tanre, and T.Nakajima, Remote sensing of tropospheric aerosols from space: Past present and future, *Bull.Amer.Meteor.Soc., 80*, 2229-2259, 1999.

King, M.D., D.M.Byrne, J.A.Reagan, and B.M.Herman, Spectral variation of optical depth at Tucson, Arizona between August 1975 and December 1977, *J.Appl.Met., 19*, 723-732, 1980.

Kotchenruther, R.A., P.V.Hobbs, and D.A.Hegg, Humidification factors for atmospheric aerosols off the mid-Atlantic coast of the United States, *J.Geophys.Res., 104*, 2239-2251, 1999.

Kotchenruther, R.A., and P.V. Hobbs, Humidification factors of aerosols from biomass burning in Brazil, in Smoke, Clouds, and Radiation - Brazil: Proceedings, edited by V.W.J.H. Kirchhoff, Transtec Editorial, 117-120, 1996.

Liousse, C., C.Devaux, F.Dulac, and H.Cachier, Aging of savanna biomass burning aerosols: consequences on their optical properties, *J.Atmos.Chem.., 22*,1-17, 1995.

Luria, M., J.F.Boatman, J.Harris, J.Ray, T.Straube, J.Chin, R.L.Gunter, G.Herbert, T.M.Gerlach, and C.C.Van Valin, Atmospheric sulfur dioxide at Mauna Loa, Hawaii, *J.Geophys.Res., 97*, 6011-6022, 1992.

Markham, B.L., J.S.Schafer, B.N.Holben, and R.N.Halthore, Atmospheric aerosol and water vapor characteristics over north central Canada during BOREAS, *J.Geophys.Res., 102*, 29737-29745, 1997.

Michalsky, J.J., J.A.Schlemmer, N.R.Larson, L.C.Harrison, W.E.Berkheiser III, and N.S.Laulainen, Measurement of the seasonal and annual variability of total column aerosol in a northeastern US network, in *Proceedings of the International Specialty Conference Aerosols and Atmospheric Optics: Radiative Balance and Visual Air Quality*, Snowbird, Utah, USA, September 26-30, 1994, vol. A, pp. 247-258, Pittsburg, PA, 1994.

Mims, F.M.III, An international haze-monitoring network for students, *Bull.Amer.Met. Soc., 80*, 1421-1431, 1999.

Greenland, D, T. Kittel, B.P. Hayden and D.S. Schimel and LTER Climate Committee members, A climate analysis of Long-Term Ecological Research Sites, Climate of Sevilleta, D.I. Moore au Chapter 17. http://lternet.edu/im/climate/climdes/

N'Tchayi Mbourou, G., J.J.Bertrand, and S.E.Nicholson, The diurnal and seasonal cycles of wind-borne dust over Africa North of the Equator, *J.Appl.Meteor., 36*, 868-882, 1997.

Perry, K.D., T.A.Cahill, R.C.Schnell, and J.M.Harris, Long-range transport of anthropogenic aerosols to the National Oceanic and Atmospheric Administration baseline station at Mauna Loa Observatory, Hawaii, *J.Geophys.Res., 104*, 18521-18533, 1999.

Peterson, J.T., E.C.Flowers, G.J.Berri, C.L.Reynolds, and J.H.Rudisill, Atmospheric turbidity over central North Carolina, *J.Appl.Met., 20*, 229-241, 1981.

Prospero, J.M., Aeolian transport to the world ocean, in *The Sea*, edited by C.Emiliani, Vol.7, pp.801-874, The Oceanic Lithosphere, Wiley Interscience, 1981.

Pye, K., *Aeolian dust and dust deposits*, Academic Press, pp.334, 1987.

O'Neill, N.T., T.F. Eck, B.N. Holben, A. Smirnov, O. Dubovik, and A. Royer, Uni and bi-modal size distribution influences on the variation of Angstrom derivatives in spectral and optical depth space, *J.Geophys.Res.,* 2000 (accepted, in press).

Reid, J.S., T.F. Eck, S.A. Christopher, P.V. Hobbs, and B.N. Holben, Use of the Angstrom exponent to estimate the variability of optical and physical properties of aging smoke particles in Brazil, *J. Geophys. Res., 104*, 27,473-27,489, 1999.

Reid, J.S., P.V.Hobbs, R.J.Ferek, D.R.Blake, J.V.Martins, M.R.Dunlap, and C.Liousse, Physical, chemical and optical properties of regional hazes dominated by smoke in Brazil, *J.Geophys.Res., 103*, 32,059-32,080, 1998.

Remer, L.A., Y.Kaufman, B.N.Holben, A.M.Thompson, and D.P.McNamara, Biomass burning aerosol size distribution and modeled optical properties, *J.Geophys.Res., 103,* 31,879-31,892, 1998.

Roosen, R.G., R.J.Angione, and C.H.Clemcke, Worldwide variations in atmospheric transmission: 1. Baseline results from Smithsonian observations, *Bull.Amer.Met.Soc., 54,* 307-316, 1973.

Russell, P.B., J.M.Livingston, E.G.Dutton, R.F.Pueschel, J.A.Reagan, T.E.Defoor, M.A.Box, D.Allen, P.Pilewskie, B.M.Herman, S.A.Kinne, and D.J.Hofman, Pinatubo and pre-Pinatubo optical depth spectra: Mauna Loa measurements, comparisons, inferred particle size distributions, radiative effects, and relationship to lidar data, *J.Geophys.Res., 98,* 22,969-22,985, 1993.

Ryan, S., The wind field around Mauna Loa derived from surface and balloon observations, *J.Geophys.Res., 102,* 10711-10725, 1997.

Schmid, B., J.J.Michaslky, D.W.Slater, J.C.Barnard, R.N.Halthore, J.C.Liljegren, B.N.Holben, T.F.Eck, J.M.Livingston, P.B.Russell, T.Ingold, and I.Slutsker, Comparison of columnar water vapor measurements during the fall 1997 ARM Intensive Observation Period: solar transmittance methods, *Appl. Opt*., 2000 (submitted).

Schmid, B., J.Michalsky, R.Halthore, M.Beauharnois, L.Harrison, J.Livingston, P.Russell, B.Holben, T.Eck, and A.Smirnov, Comparison of aerosol optical depth from four solar radiometers during the fall 1997 ARM intensive observation period, *Geoph.Res.Lett., 26,* 2725-2728, 1999.

Scholes, C.O., J.D.Kendall, and C.O.Justice, The quantity of biomass burned in southern Africa, *J.Geophys.Res., 101*, 23667-23676, 1996a.

Scholes, C.O., D.E.Ward, and C.O.Justice, Emissions of trace gases and aerosol particles due to vegetation burning in southern hemisphere Africa, *J.Geophys.Res., 101*, 23677-23682, 1996b.

Schutz, L., Long range transport of desert dust with special emphasis on the Sahara, *Ann.N.Y.Acad.Sci., 338*, 515-531, 1980.

Shaw G.E., Atmospheric turbidity in the Polar regions, *J.Appl.Met., 21*, 1080-1088, 1982a.

Shaw, G.E., Solar spectral irradiance and atmospheric transmission at Mauna Loa Observatory, *Appl.Opt, 21*, 2006-2011, 1982b.

Shaw, G.E., Sunphotometry, *Bull.Am.Meteor.Soc., 64*, 4-10, 1983.

Shaw, G.E., Transport of Asian desert dust to the Hawaiian Islands, *J.Appl.Meteor., 19*, 1254-1259, 1980.

Shaw, G.E., Aerosols at Mauna Loa: optical properties, *J.Atmos.Sci., 36*, 862-869, 1979.

Smirnov, A., B.N.Holben, T.F.Eck, O.Dubovik, and I.Slutsker, Cloud screening and quality control algorithms for the AERONET data base, *Rem. Sens. Env.*, 73(3), 337-349, 2000a.

Smirnov, A., B.N.Holben, O.Dubovik, N.T.O'Neill, L.A.Remer, T.F.Eck, I.Slutsker, and D.Savoie, Measurement of atmospheric optical parameters on US Atlantic coast sites, ships and Bermuda during TARFOX, *J.Geophys.Res., 105*, 9887-9901, 2000b.

Smirnov, A., N.T.O'Neill, A.Royer, A.Tarussov, and B.McArthur, Aerosol optical depth over Canada and the link with synoptic air mass types, *J.Geophys.Res., 101*, 19,299-19318, 1996.

Smirnov, A., O.Yershov, and Y.Villevalde, Aerosol optical depth in the Atlantic Ocean and Mediterranean Sea, *Proc. SPIE, 2582*, 203-214, 1995.

Stocks, B.J., The extent and impact of forest fires in northern circumpolar countries, in *Global Biomass Burning: Atmospheric, Climatic, and Biospheric Implications*, Edited by J.S. Levine, pp. 197-202, MIT Press, Cambridge , Mass., 1991.

Trewartha, G.T., *An Introduction to Climate*, 369 pp., McGraw-Hill Book, NY, 1954.

Volz, F.E., Some results of turbidity networks, *Tellus, 21*, 625-630, 1969.

Figure captions.

Figure 1. AERONET federated site distribution including nine described sites (green), 20 appended sites (red) and the distribution as of November 2000 (blue).

Figure 2. Time series of the zero airmass voltages (Vo) of AERONET reference instrument #101. Vo values were determined from the Langley technique from stable mornings at MLO observatory.

Figure 3. Mauna Loa, Hawaii. Mean monthly values of aerosol optical depth at the wavelength 500 nm for the whole period of measurements (a) (the bars indicate plus or minus one standard deviation), mean monthly (b) and mean daily values (c) of aerosol optical depth at 500 nm, mean daily values of precipitable water (d), frequency of occurrence of aerosol optical depth (e) and Angstrom parameter (f), scattergram of Angstrom parameter versus aerosol optical depth (g), and scattergram of aerosol optical depth versus precipitable water (h).

Figure 4. Goddard Space Flight Center, Greenbelt, Maryland. Mean monthly values of aerosol optical depth at the wavelength 500 nm (a) and Angstrom parameter (b) for the whole period of measurements (the bars indicate plus or minus one standard deviation), mean monthly values of aerosol optical depth at 500 nm (c), Angstrom parameter (d), and precipitable water (e), scattergram of mean monthly values of aerosol optical depth versus precipitable water (f), mean daily values of aerosol optical depth at 500 nm (g), mean daily values of precipitable water (h), frequency of occurrence of aerosol optical depth (i) and Angstrom parameter (j), scattergram of Angstrom parameter versus aerosol optical depth (k), and scattergram of aerosol optical depth versus precipitable water (l).

Figure 5. Goddard Space Flight Center, Greenbelt, Maryland. Seasonal frequency of occurrence of aerosol optical depth and Angstrom parameter for (a and b) winter (December – January – February), (c and d) spring (March – April – May), (e and f) summer (June – July – August), and (g and h) autumn (September – October – November). The sum of all frequencies is equal to 100% for each season.

Figure 6. Sevilleta, New Mexico. Mean monthly values of aerosol optical depth at the wavelength 500 nm (a) and Angstrom parameter (b) for the whole period of measurements (the bars indicate plus or minus one standard deviation), mean monthly (c) and mean daily values (d) of aerosol optical depth at 500 nm, mean daily values of precipitable water (e), frequency of occurrence of aerosol optical depth (f) and Angstrom parameter (g), scattergram of Angstrom parameter versus aerosol optical depth (h), and scattergram of aerosol optical depth versus precipitable water (i).

Figure 7. H.J. Andrews, Oregon. As in Figure 6.

Figure 8. Cape Verde, Sal Island. As in Figure 6.

Figure 9. Banizoumbou, Niger. As in Figure 6.

Figure 10. Mongu, Zambia. As in Figure 6.

Figure 11. Cuiaba, Brazil. As in Figure 6.

Figure 12. Thompson, Manitoba, Canada. As in Figure 6.

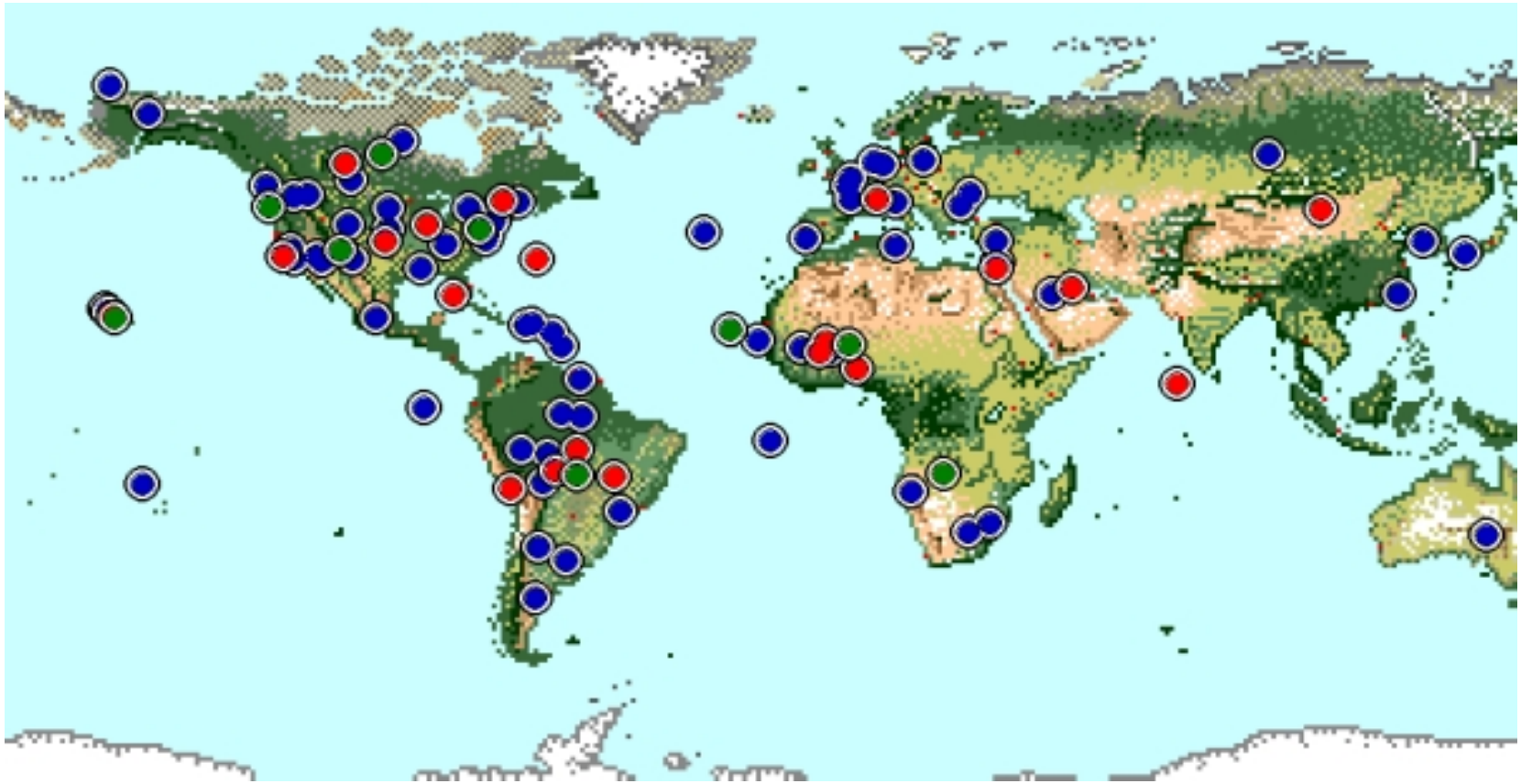

Figure 1

Figure 2

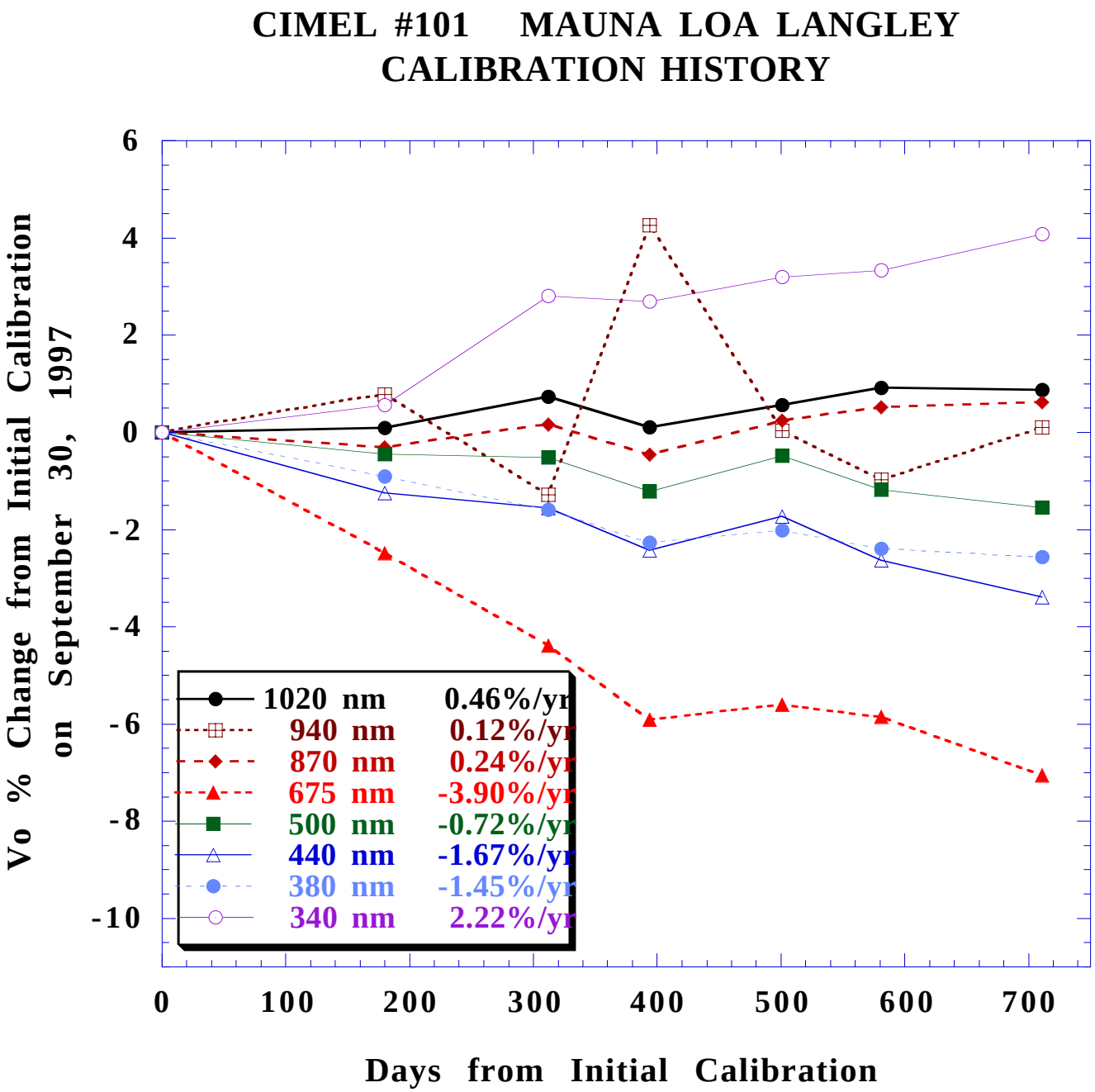
CIMEL #101 MAUNA LOA LANGLEY
CALIBRATION HISTORY
Vo % Change from Initial Calibration
on September 30, 1997
Days from Initial Calibration
6
4
2
0
-2
-4
-6
-8
-10
0
100
200
300
400
500
600
700
1020 nm 0.46%/yr
940 nm 0.12%/yr
870 nm 0.24%/yr
675 nm -3.90%/yr
500 nm -0.72%/yr
440 nm -1.67%/yr
380 nm -1.45%/yr
340 nm 2.22%/yr

Figure 3

a)

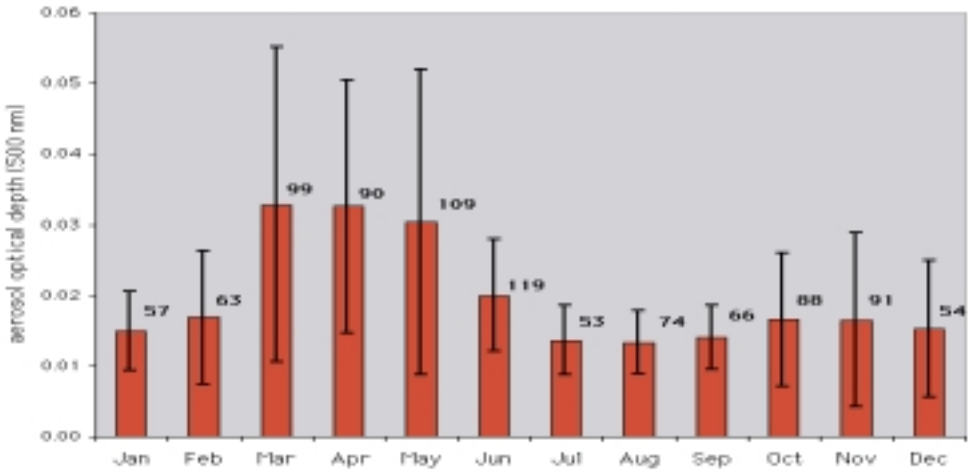
aerosol optical depth (500 nm)
0.06
0.05
0.04
0.03
0.02
0.01
0.00
57
63
99
90
109
119
53
74
66
88
91
54
Jan
Feb
Mar
Apr
May
Jun
Jul
Aug
Sep
Oct
Nov
Dec

b)

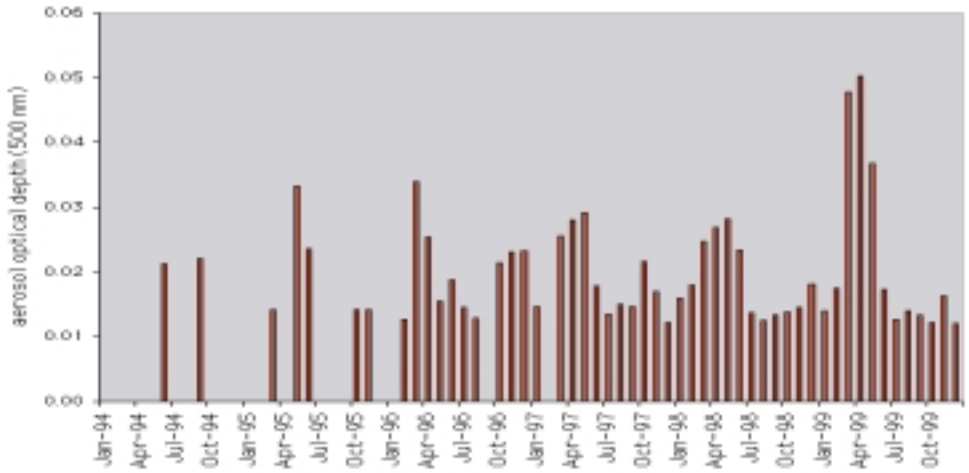
aerosol optical depth (500 nm)
0.06
0.05
0.04
0.03
0.02
0.01
0.00
Jan-94
Apr-94
Jul-94
Oct-94
Jan-95
Apr-95
Jul-95
Oct-95
Jan-96
Apr-96
Jul-96
Oct-96
Jan-97
Apr-97
Jul-97
Oct-97
Jan-98
Apr-98
Jul-98
Oct-98
Jan-99
Apr-99
Jul-99
Oct-99

Fig.3

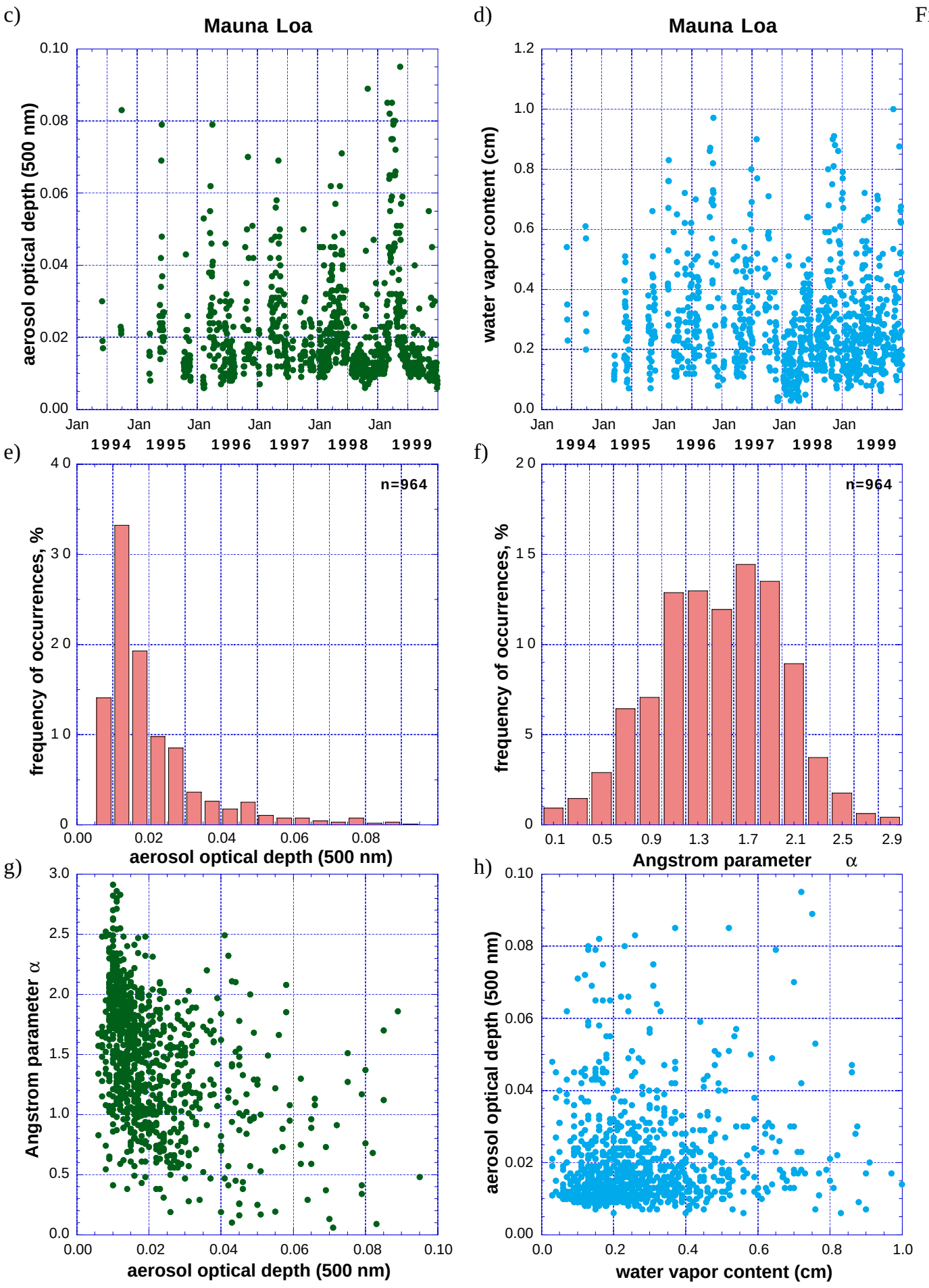
c)
Mauna Loa
aerosol optical depth (500 nm)
0.00
0.02
0.04
0.06
0.08
0.10
Jan 1994
Jan 1995
Jan 1996
Jan 1997
Jan 1998
Jan 1999
d)
Mauna Loa
water vapor content (cm)
0.0
0.2
0.4
0.6
0.8
1.0
1.2
Jan 1994
Jan 1995
Jan 1996
Jan 1997
Jan 1998
Jan 1999
e)
n=964
frequency of occurrences, %
0
10
20
30
40
0.00
0.02
0.04
0.06
0.08
aerosol optical depth (500 nm)
f)
n=964
frequency of occurrences, %
0
5
10
15
20
0.1
0.5
0.9
1.3
1.7
2.1
2.5
2.9
Angstrom parameter α
g)
Angstrom parameter α
0.0
0.5
1.0
1.5
2.0
2.5
3.0
0.00
0.02
0.04
0.06
0.08
0.10
aerosol optical depth (500 nm)
h)
aerosol optical depth (500 nm)
0.00
0.02
0.04
0.06
0.08
0.10
0.0
0.2
0.4
0.6
0.8
1.0
water vapor content (cm)

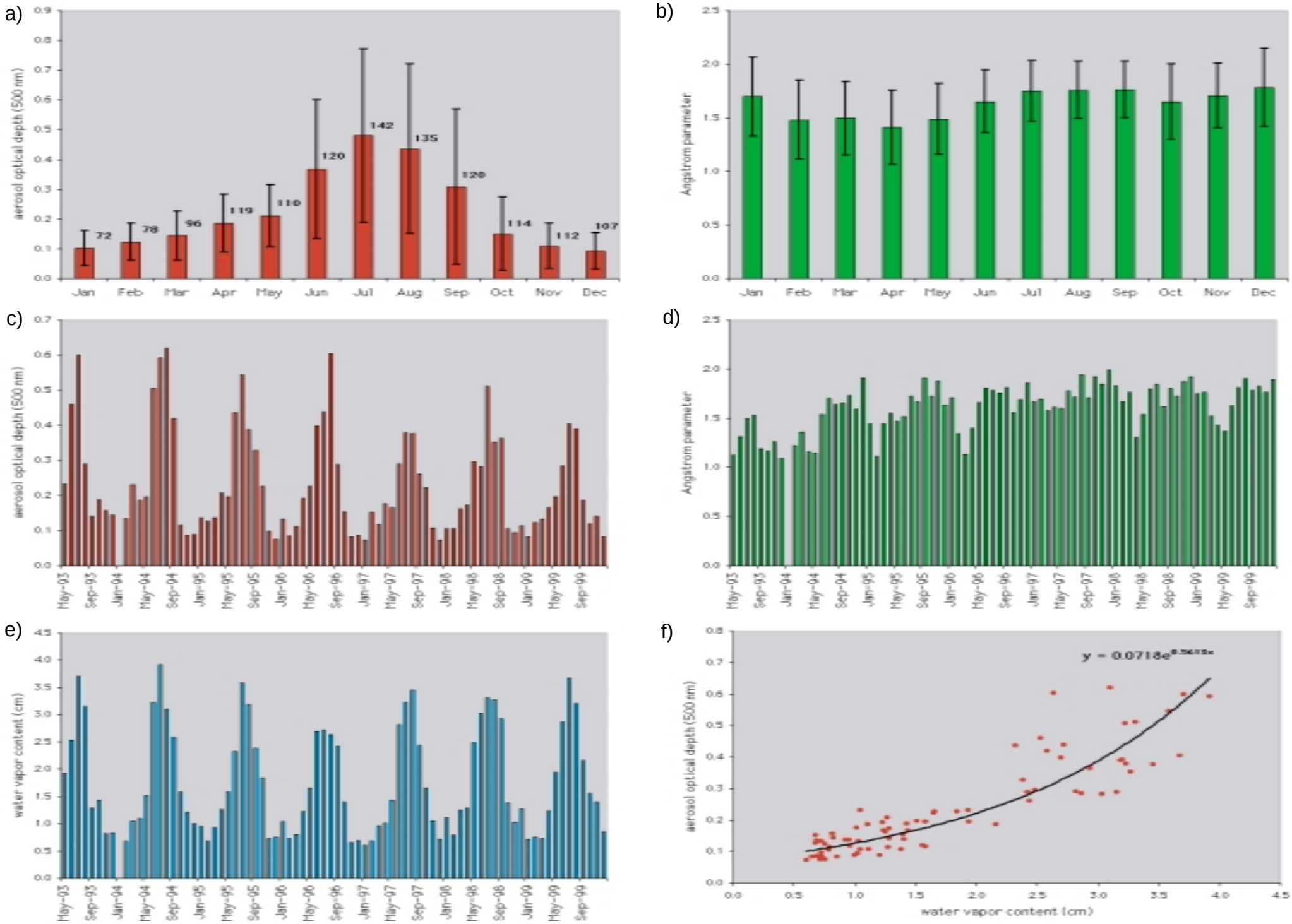
a)
aerosol optical depth (500 nm)
72
78
96
119
110
120
142
135
120
114
112
107
Jan
Feb
Mar
Apr
May
Jun
Jul
Aug
Sep
Oct
Nov
Dec
b)
Angstrom parameter
c)
aerosol optical depth (500 nm)
d)
Angstrom parameter
e)
water vapor content (cm)
f)
aerosol optical depth (500 nm)
water vapor content (cm)

Figure 4

g)

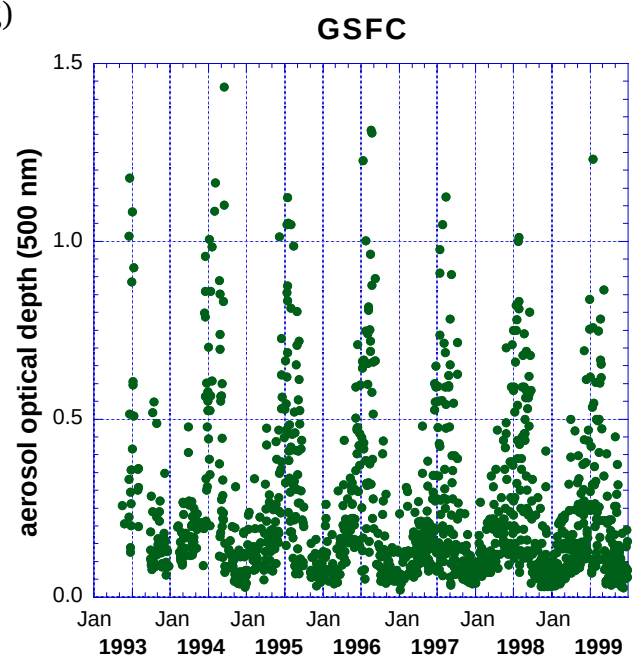
GSFC
aerosol optical depth (500 nm)
1.5
1.0
0.5
0.0
Jan 1993
Jan 1994
Jan 1995
Jan 1996
Jan 1997
Jan 1998
Jan 1999

h)

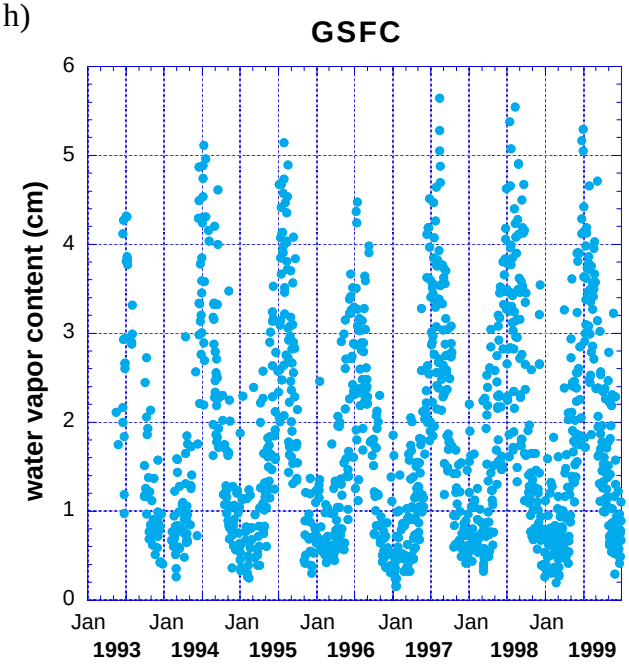
GSFC
water vapor content (cm)
6
5
4
3
2
1
0
Jan 1993
Jan 1994
Jan 1995
Jan 1996
Jan 1997
Jan 1998
Jan 1999

i)

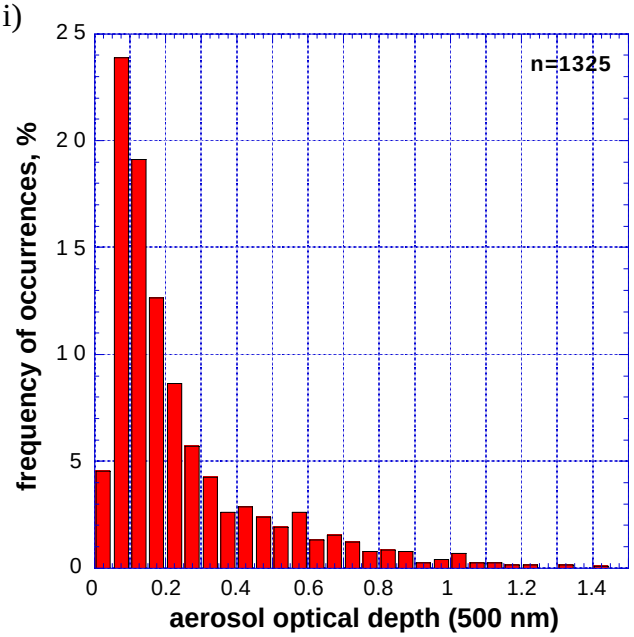
n=1325
frequency of occurrences, %
25
20
15
10
5
0
0
0.2
0.4
0.6
0.8
1
1.2
1.4
aerosol optical depth (500 nm)

j)

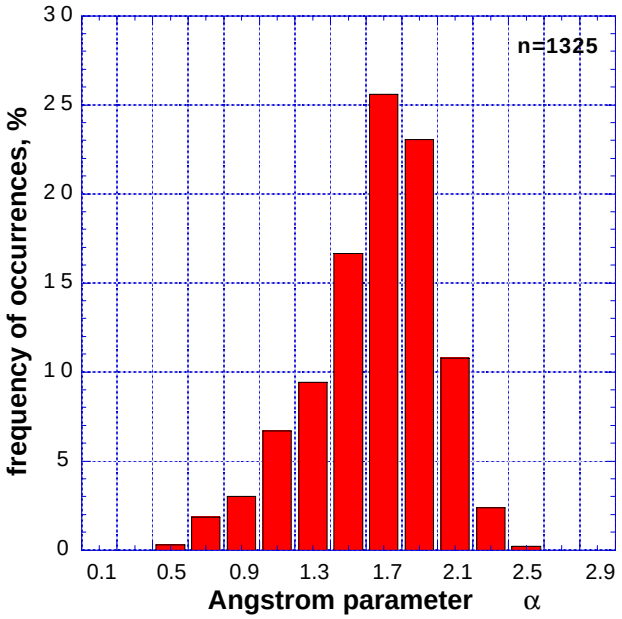
n=1325
frequency of occurrences, %
30
25
20
15
10
5
0
0.1
0.5
0.9
1.3
1.7
2.1
2.5
2.9
Angstrom parameter α

k)

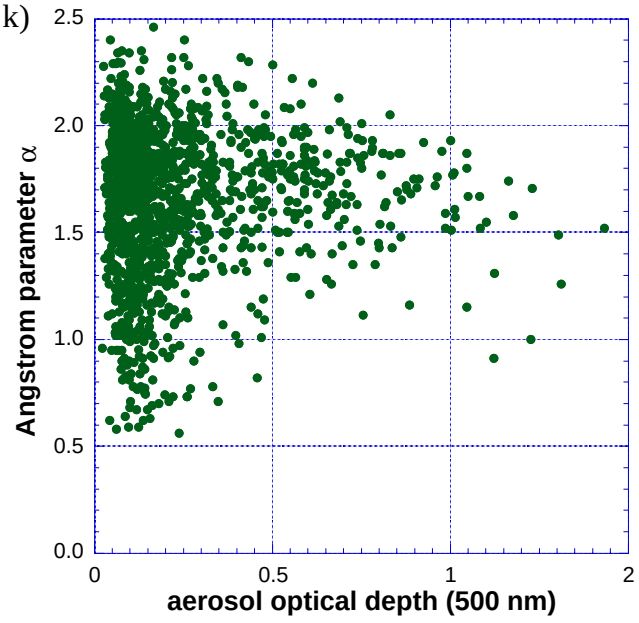
Angstrom parameter α
2.5
2.0
1.5
1.0
0.5
0.0
0
0.5
1
2
aerosol optical depth (500 nm)

l)

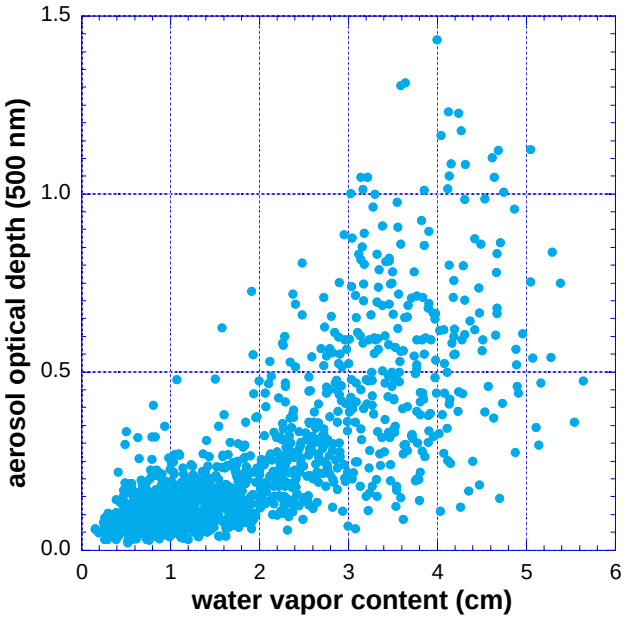
aerosol optical depth (500 nm)
1.5
1.0
0.5
0.0
0
1
2
3
4
5
6
water vapor content (cm)

Fig.5

a)

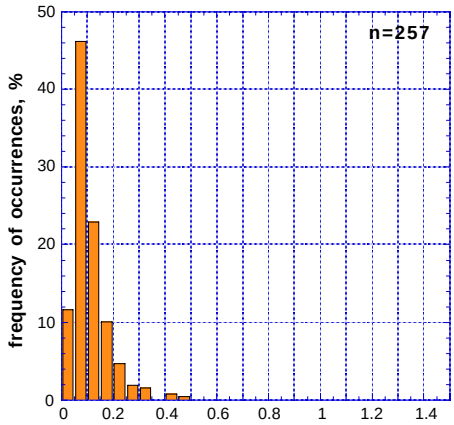

Winter, D-J-F

b)

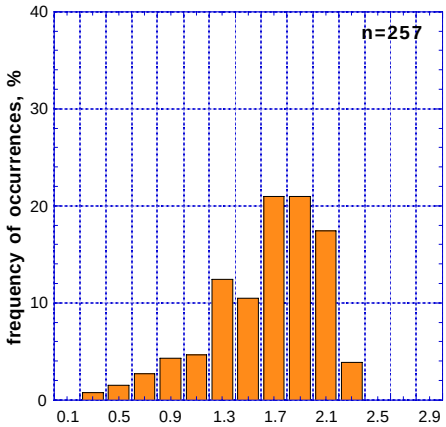

c)

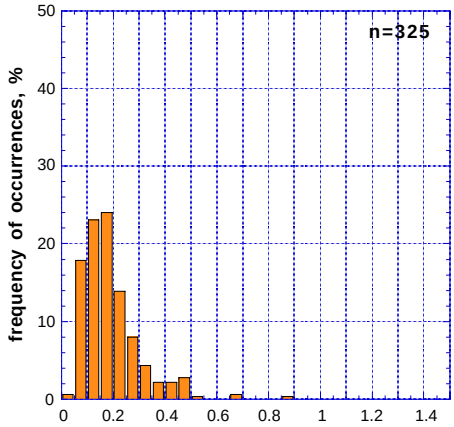

Spring, M-A-M

d)

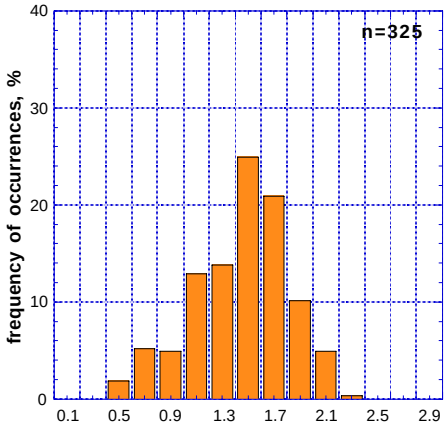

e)

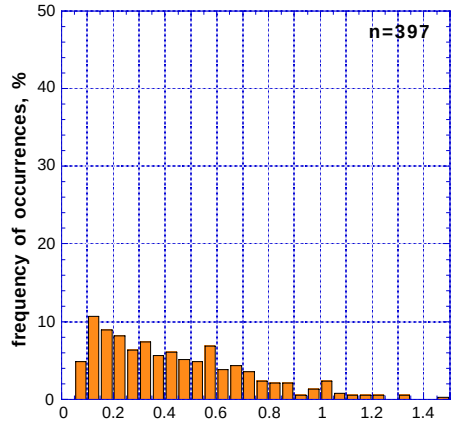

Summer, J-J-A

f)

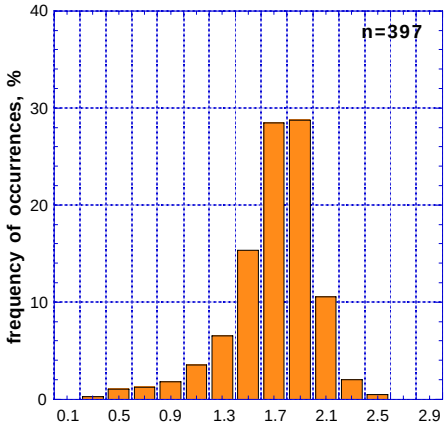

g)

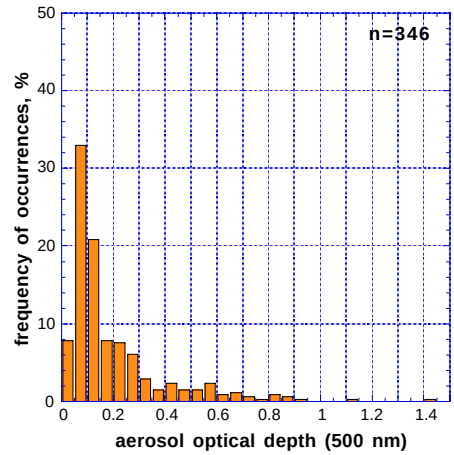

Fall, S-O-N

h)

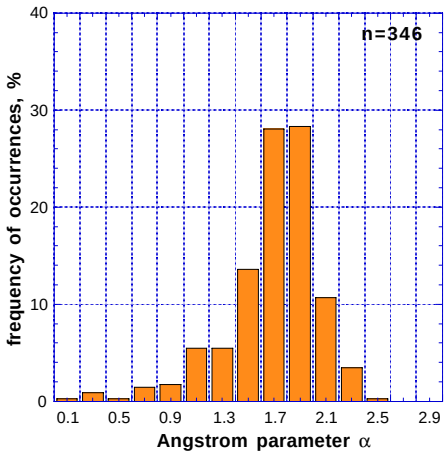

Figure 6

a)

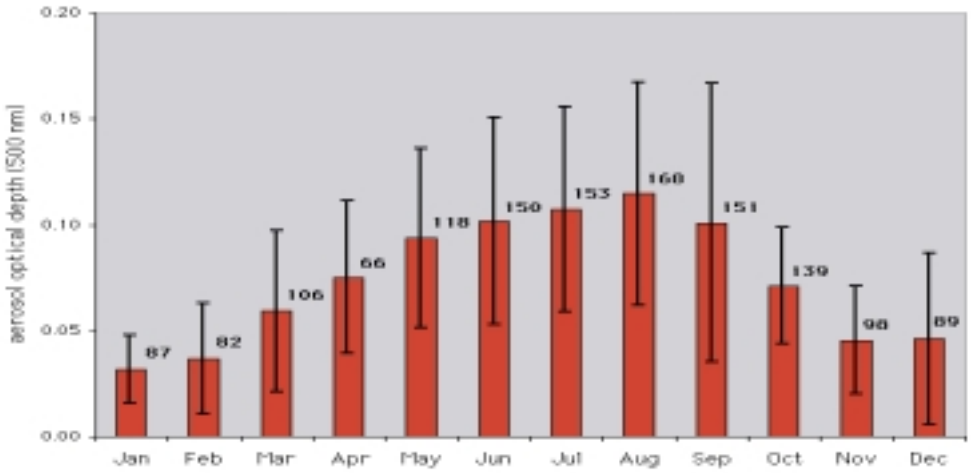
aerosol optical depth (500 nm)
0.20
0.15
0.10
0.05
0.00
87
82
106
66
118
150
153
168
151
139
98
89
Jan
Feb
Mar
Apr
May
Jun
Jul
Aug
Sep
Oct
Nov
Dec

b)

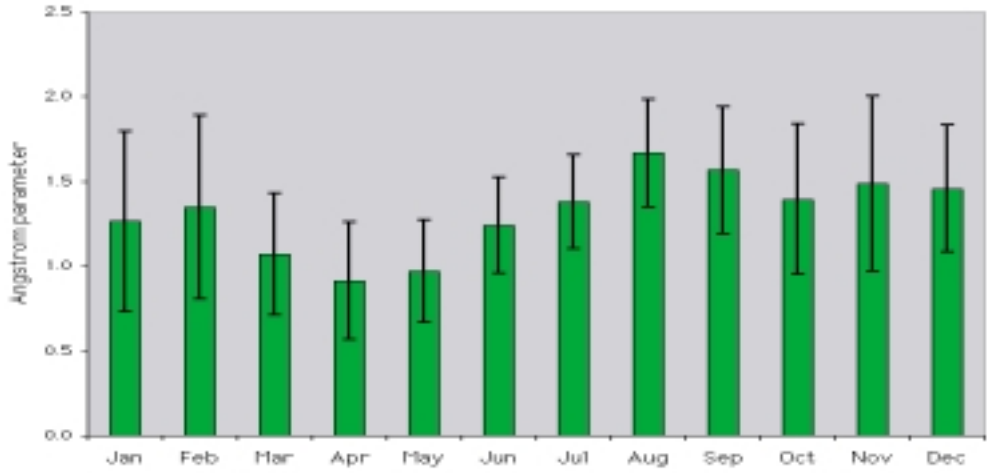
Angstrom parameter
2.5
2.0
1.5
1.0
0.5
0.0
Jan
Feb
Mar
Apr
May
Jun
Jul
Aug
Sep
Oct
Nov
Dec

c)

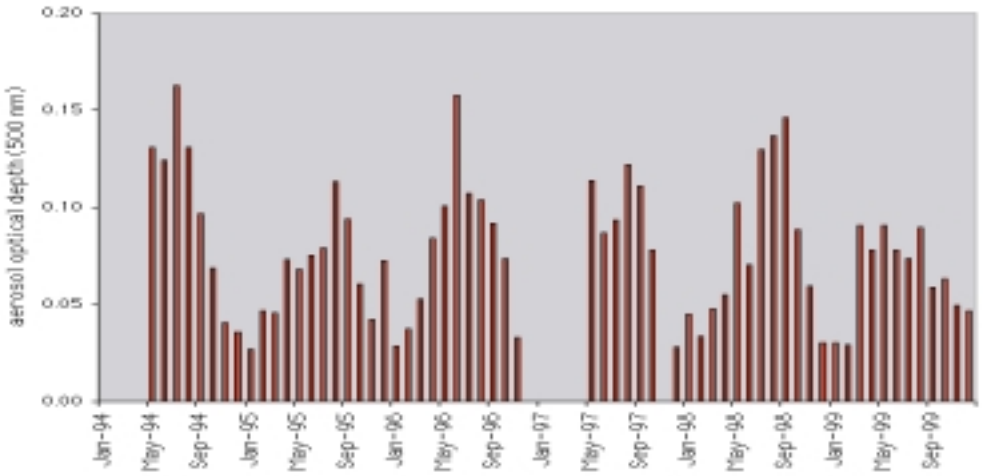
aerosol optical depth (500 nm)
0.20
0.15
0.10
0.05
0.00
Jan-94
May-94
Sep-94
Jan-95
May-95
Sep-95
Jan-96
May-96
Sep-96
Jan-97
May-97
Sep-97
Jan-98
May-98
Sep-98
Jan-99
May-99
Sep-99

Fig.6

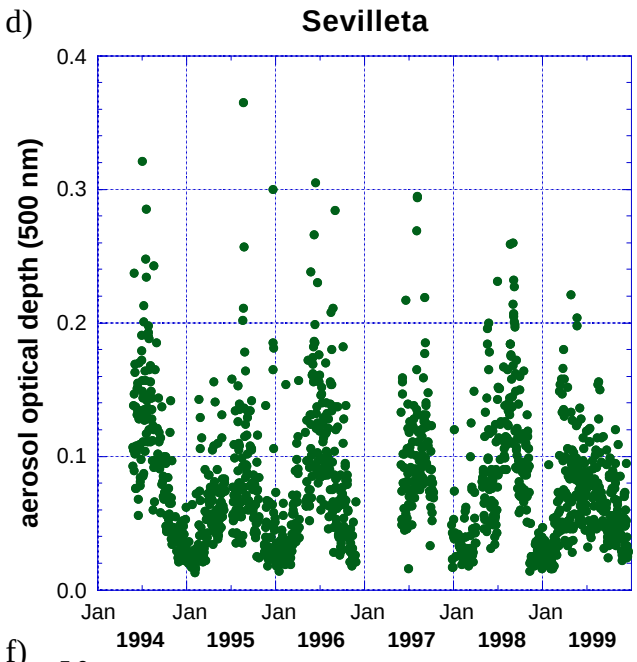
d)
Sevilleta
aerosol optical depth (500 nm)
0.0
0.1
0.2
0.3
0.4
Jan 1994
Jan 1995
Jan 1996
Jan 1997
Jan 1998
Jan 1999

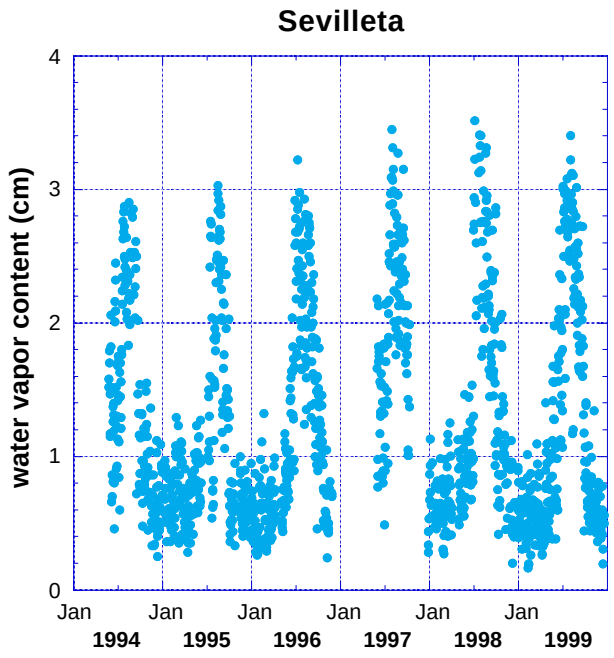
e)
Sevilleta
water vapor content (cm)
0
1
2
3
4
Jan 1994
Jan 1995
Jan 1996
Jan 1997
Jan 1998
Jan 1999

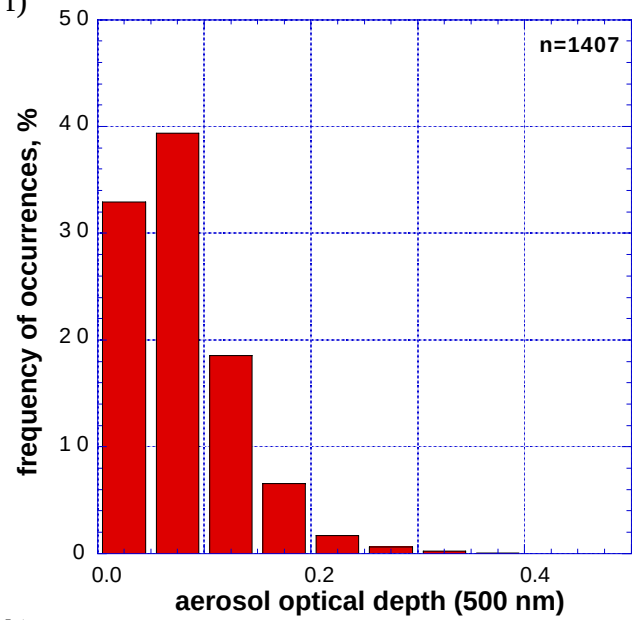
f)
n=1407
frequency of occurrences, %
0
10
20
30
40
50
0.0
0.2
0.4
aerosol optical depth (500 nm)

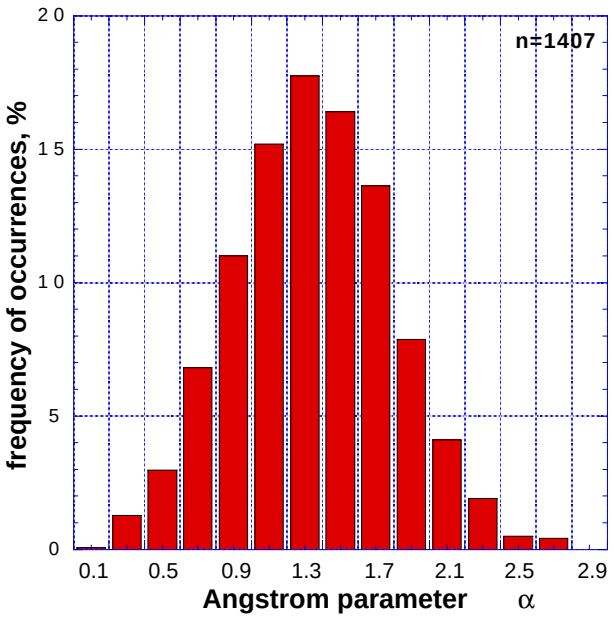
g)
n=1407
frequency of occurrences, %
0
5
10
15
20
0.1
0.5
0.9
1.3
1.7
2.1
2.5
2.9
Angstrom parameter α

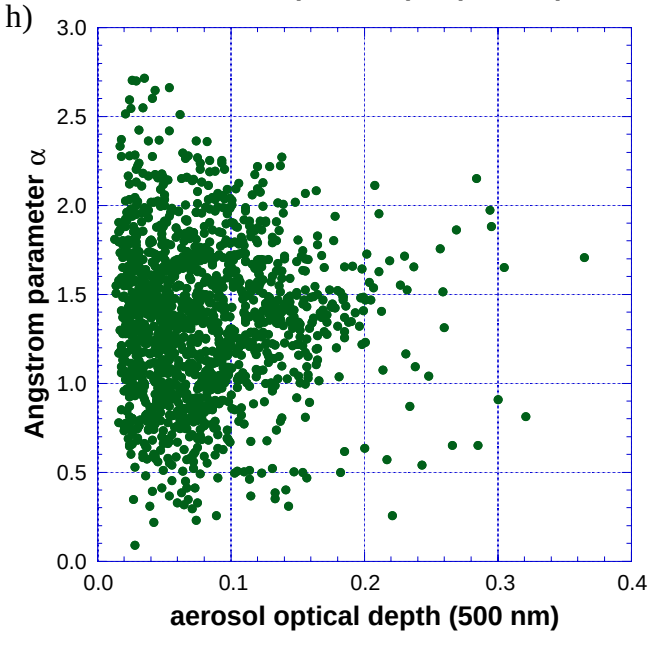
h)
Angstrom parameter α
0.0
0.5
1.0
1.5
2.0
2.5
3.0
0.0
0.1
0.2
0.3
0.4
aerosol optical depth (500 nm)

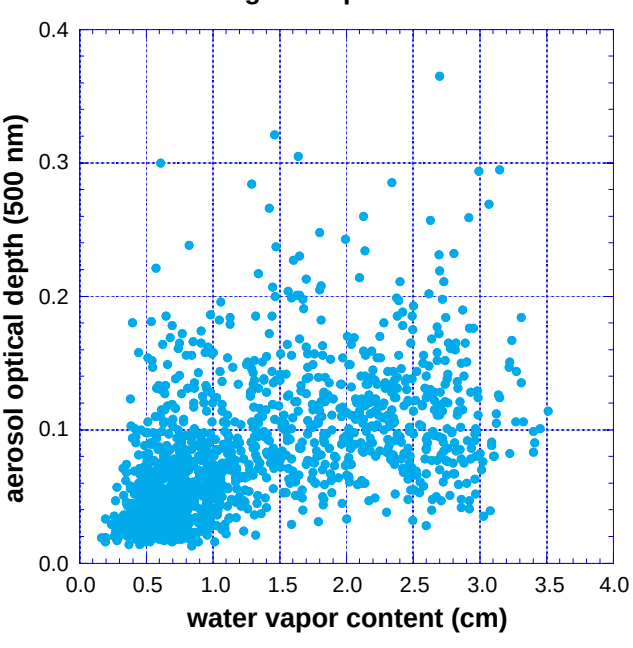
i)
aerosol optical depth (500 nm)
0.0
0.1
0.2
0.3
0.4
0.0
0.5
1.0
1.5
2.0
2.5
3.0
3.5
4.0
water vapor content (cm)

Figure 7

a)

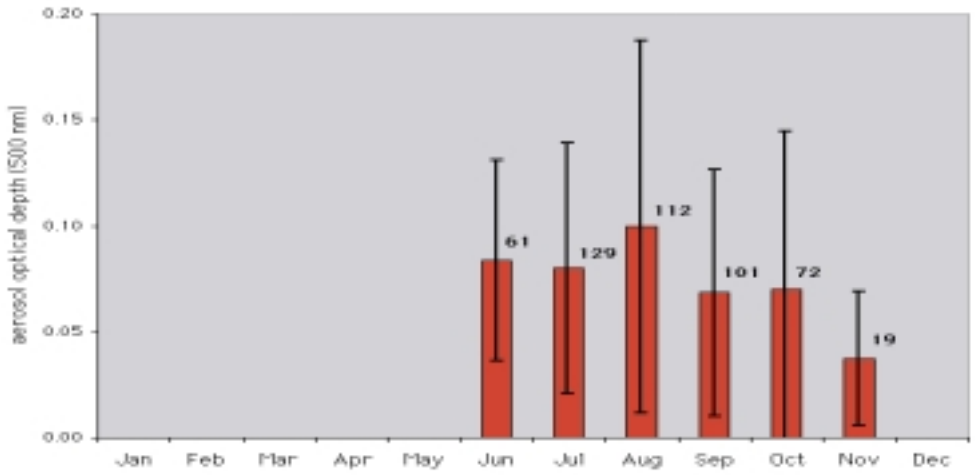
aerosol optical depth (500 nm)
0.20
0.15
0.10
0.05
0.00
61
129
112
101
72
19
Jan
Feb
Mar
Apr
May
Jun
Jul
Aug
Sep
Oct
Nov
Dec

b)

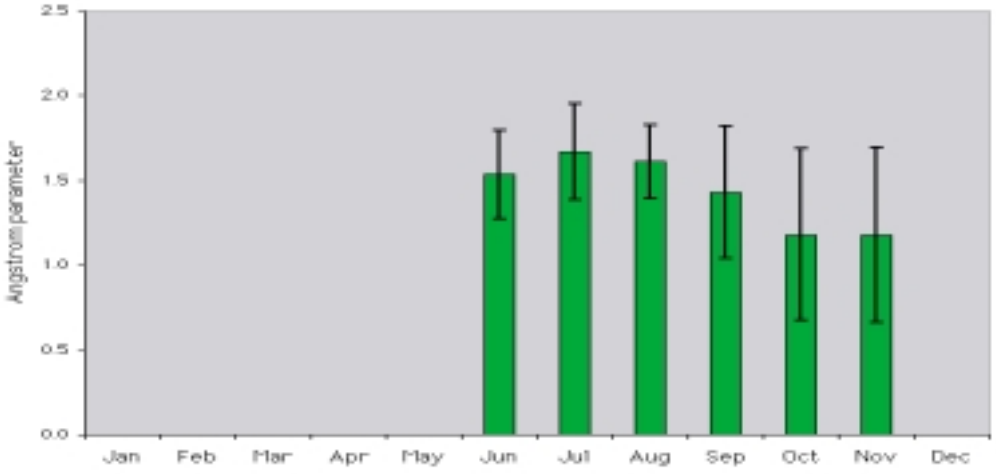
Angstrom parameter
2.5
2.0
1.5
1.0
0.5
0.0
Jan
Feb
Mar
Apr
May
Jun
Jul
Aug
Sep
Oct
Nov
Dec

c)

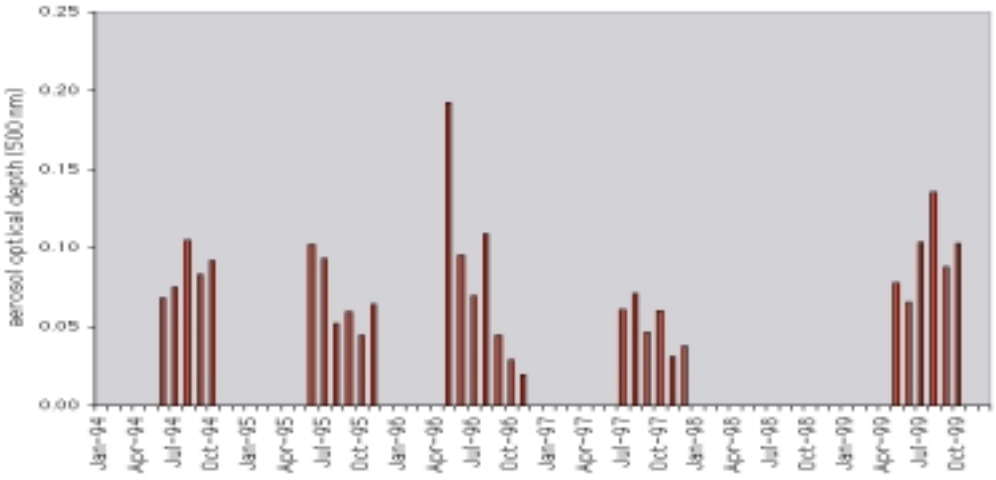
aerosol optical depth (500 nm)
0.25
0.20
0.15
0.10
0.05
0.00
Jan-94
Apr-94
Jul-94
Oct-94
Jan-95
Apr-95
Jul-95
Oct-95
Jan-96
Apr-96
Jul-96
Oct-96
Jan-97
Apr-97
Jul-97
Oct-97
Jan-98
Apr-98
Jul-98
Oct-98
Jan-99
Apr-99
Jul-99
Oct-99

Fig.7

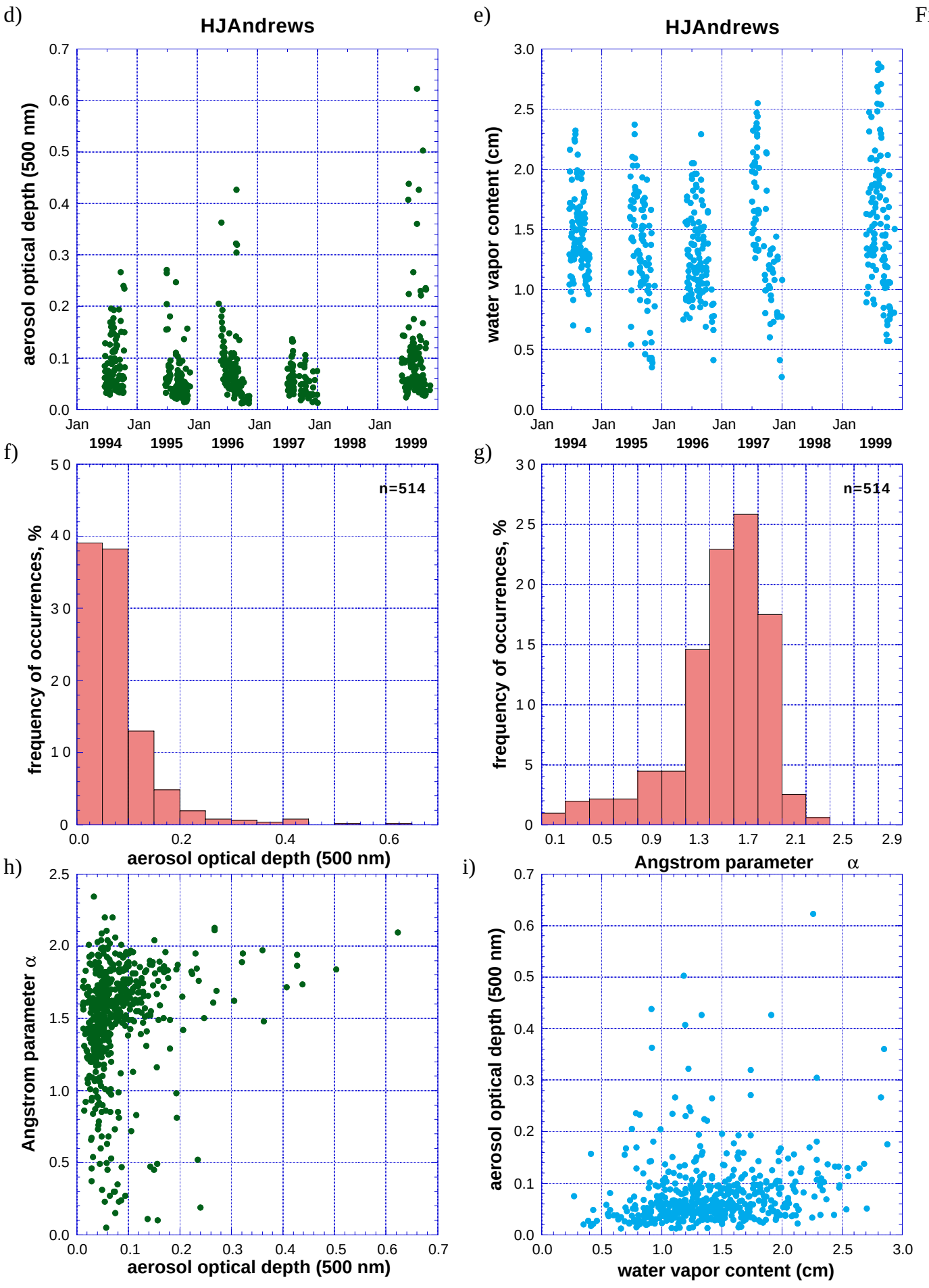
d)
HJAndrews
aerosol optical depth (500 nm)
Jan 1994
Jan 1995
Jan 1996
Jan 1997
Jan 1998
Jan 1999
e)
HJAndrews
water vapor content (cm)
f)
n=514
frequency of occurrences, %
aerosol optical depth (500 nm)
g)
n=514
frequency of occurrences, %
Angstrom parameter α
h)
Angstrom parameter α
aerosol optical depth (500 nm)
i)
aerosol optical depth (500 nm)
water vapor content (cm)

Figure 8

a)

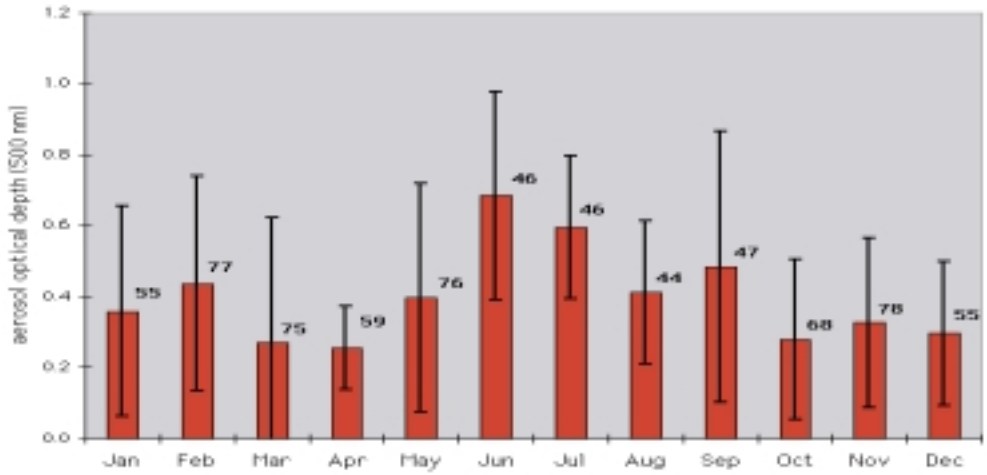
aerosol optical depth (500 nm)
1.2
1.0
0.8
0.6
0.4
0.2
0.0
55
77
75
59
76
46
46
44
47
68
78
55
Jan
Feb
Mar
Apr
May
Jun
Jul
Aug
Sep
Oct
Nov
Dec

b)

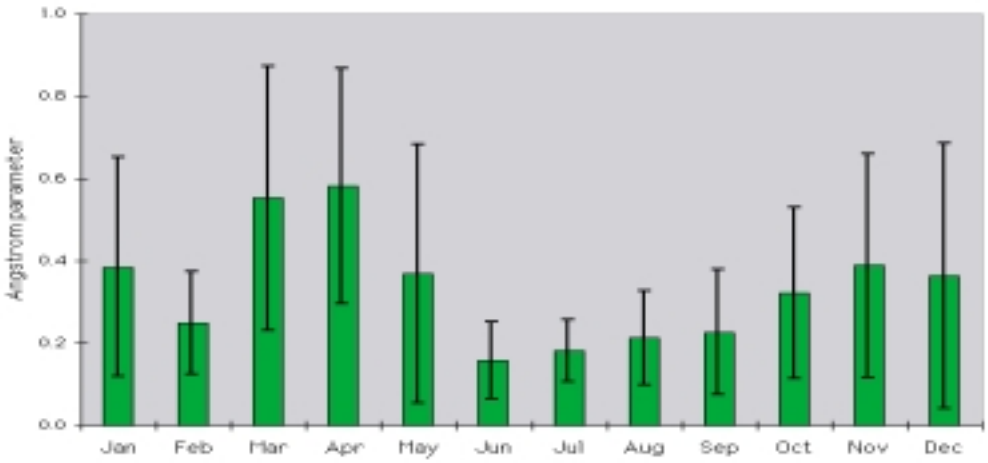
Angstrom parameter
1.0
0.8
0.6
0.4
0.2
0.0
Jan
Feb
Mar
Apr
May
Jun
Jul
Aug
Sep
Oct
Nov
Dec

c)

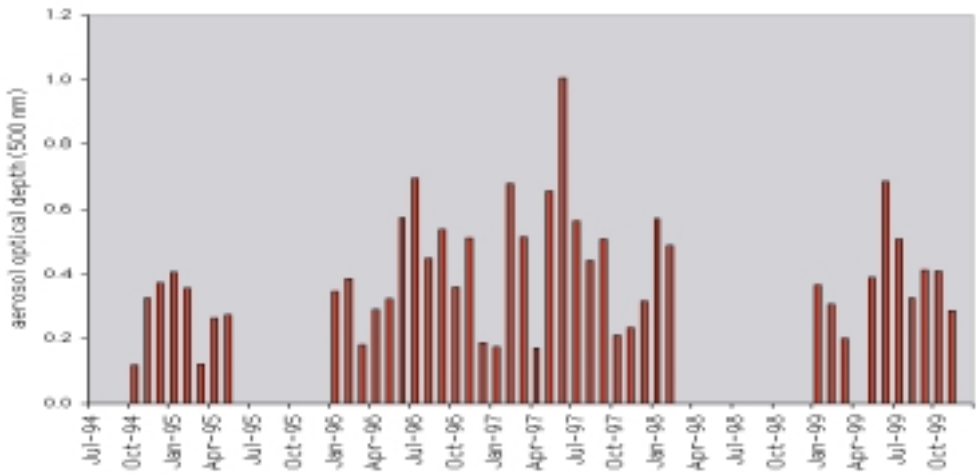
aerosol optical depth (500 nm)
1.2
1.0
0.8
0.6
0.4
0.2
0.0
Jul-94
Oct-94
Jan-95
Apr-95
Jul-95
Oct-95
Jan-96
Apr-96
Jul-96
Oct-96
Jan-97
Apr-97
Jul-97
Oct-97
Jan-98
Apr-98
Jul-98
Oct-98
Jan-99
Apr-99
Jul-99
Oct-99

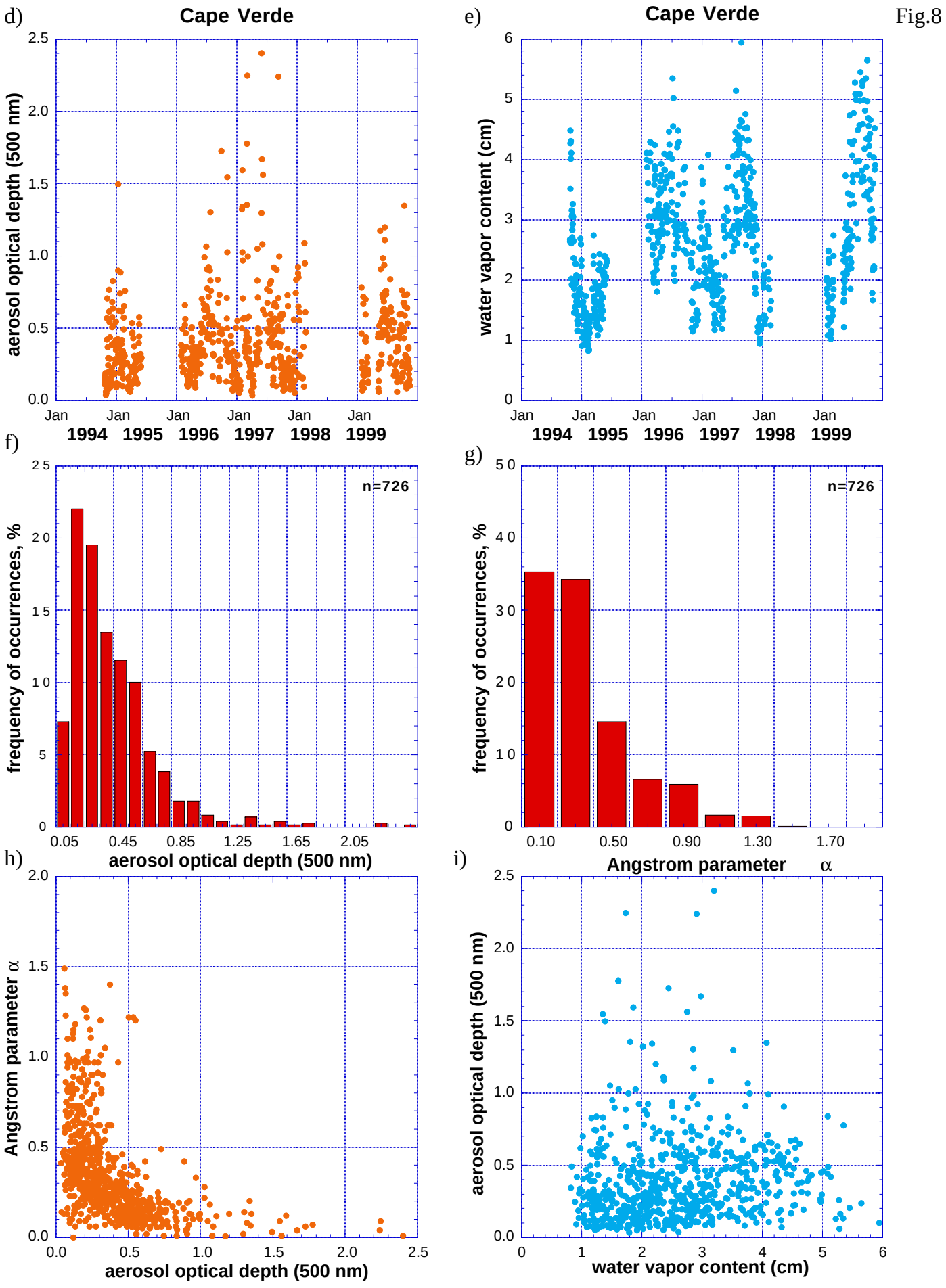
d)
Cape Verde
aerosol optical depth (500 nm)
Jan 1994
Jan 1995
Jan 1996
Jan 1997
Jan 1998
Jan 1999
e)
Cape Verde
water vapor content (cm)
f)
n=726
frequency of occurrences, %
aerosol optical depth (500 nm)
g)
n=726
frequency of occurrences, %
Angstrom parameter α
h)
Angstrom parameter α
aerosol optical depth (500 nm)
i)
aerosol optical depth (500 nm)
water vapor content (cm)

Fig.8

Figure 9

a)

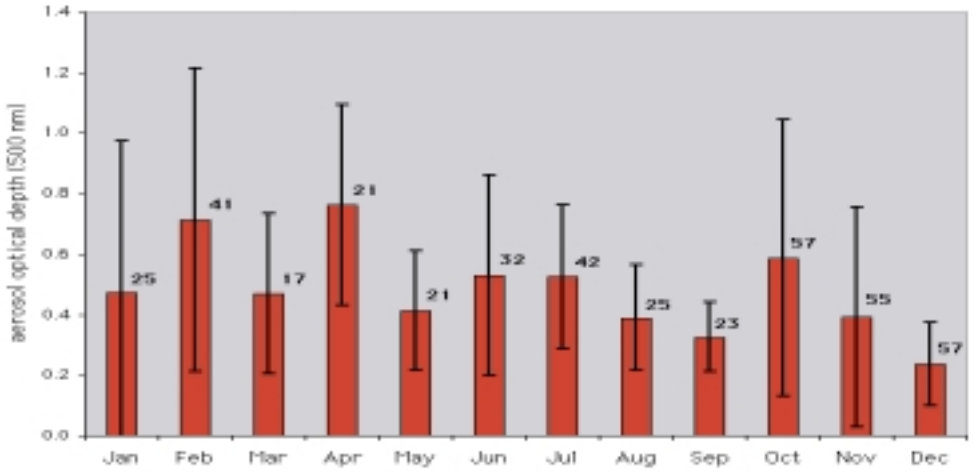
aerosol optical depth (500 nm)
1.4
1.2
1.0
0.8
0.6
0.4
0.2
0.0
25
41
17
21
21
32
42
25
23
57
55
57
Jan
Feb
Mar
Apr
May
Jun
Jul
Aug
Sep
Oct
Nov
Dec

b)

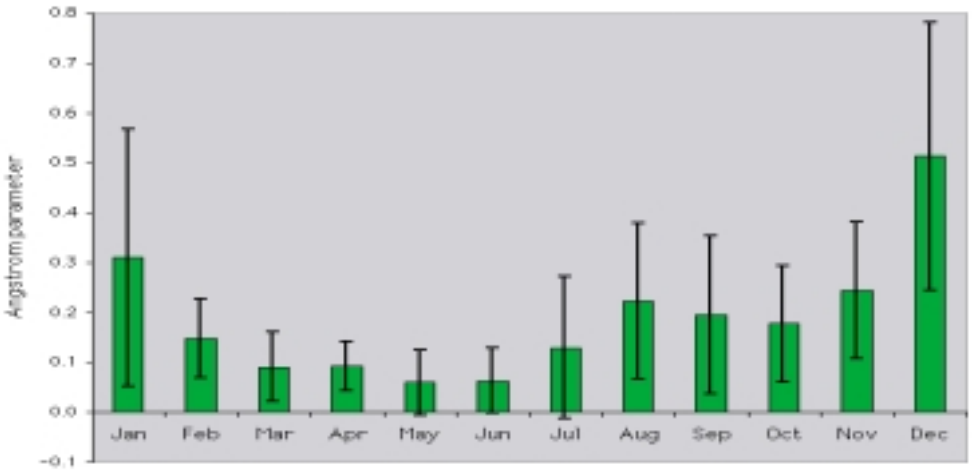
Angstrom parameter
0.8
0.7
0.6
0.5
0.4
0.3
0.2
0.1
0.0
-0.1
Jan
Feb
Mar
Apr
May
Jun
Jul
Aug
Sep
Oct
Nov
Dec

c)

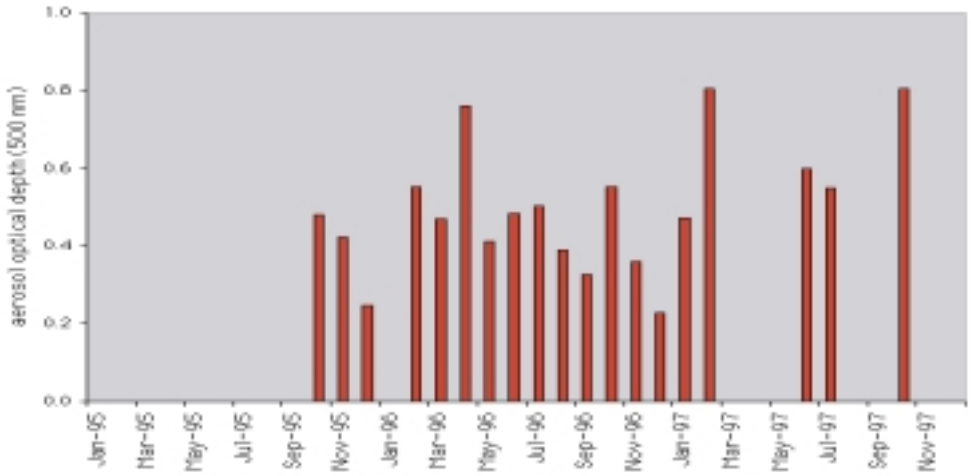
aerosol optical depth (500 nm)
1.0
0.8
0.6
0.4
0.2
0.0
Jan-95
Mar-95
May-95
Jul-95
Sep-95
Nov-95
Jan-96
Mar-96
May-96
Jul-96
Sep-96
Nov-96
Jan-97
Mar-97
May-97
Jul-97
Sep-97
Nov-97

Fig.9

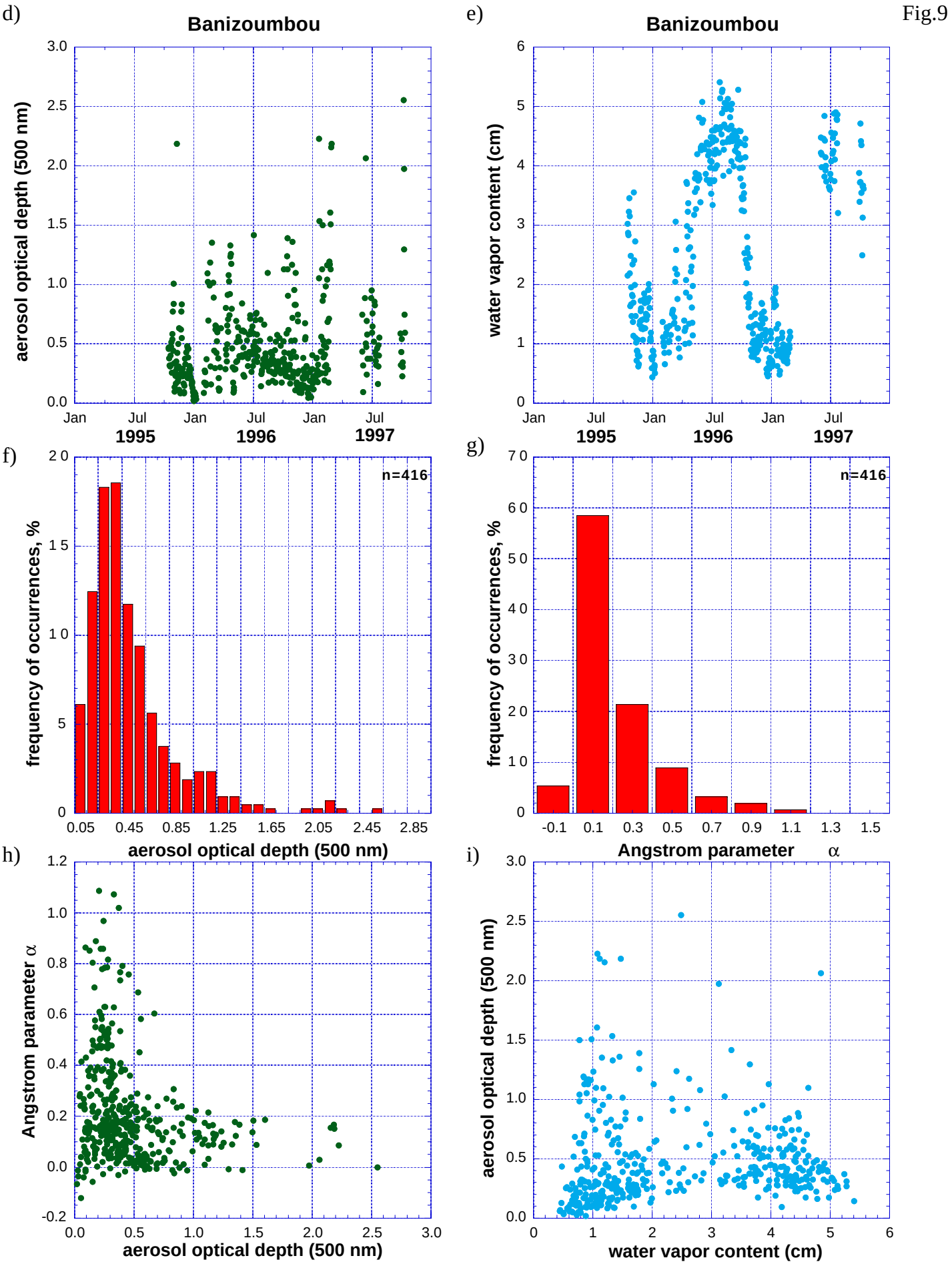
d)
Banizoumbou
aerosol optical depth (500 nm)
3.0
2.5
2.0
1.5
1.0
0.5
0.0
Jan
Jul
Jan
Jul
Jan
Jul
1995
1996
1997
e)
Banizoumbou
water vapor content (cm)
6
5
4
3
2
1
0
Jan
Jul
Jan
Jul
Jan
Jul
1995
1996
1997
f)
n=416
frequency of occurrences, %
20
15
10
5
0
0.05
0.45
0.85
1.25
1.65
2.05
2.45
2.85
aerosol optical depth (500 nm)
g)
n=416
frequency of occurrences, %
70
60
50
40
30
20
10
0
-0.1
0.1
0.3
0.5
0.7
0.9
1.1
1.3
1.5
Angstrom parameter α
h)
Angstrom parameter α
1.2
1.0
0.8
0.6
0.4
0.2
0.0
-0.2
0.0
0.5
1.0
1.5
2.0
2.5
3.0
aerosol optical depth (500 nm)
i)
aerosol optical depth (500 nm)
3.0
2.5
2.0
1.5
1.0
0.5
0.0
0
1
2
3
4
5
6
water vapor content (cm)

Figure 10

a)

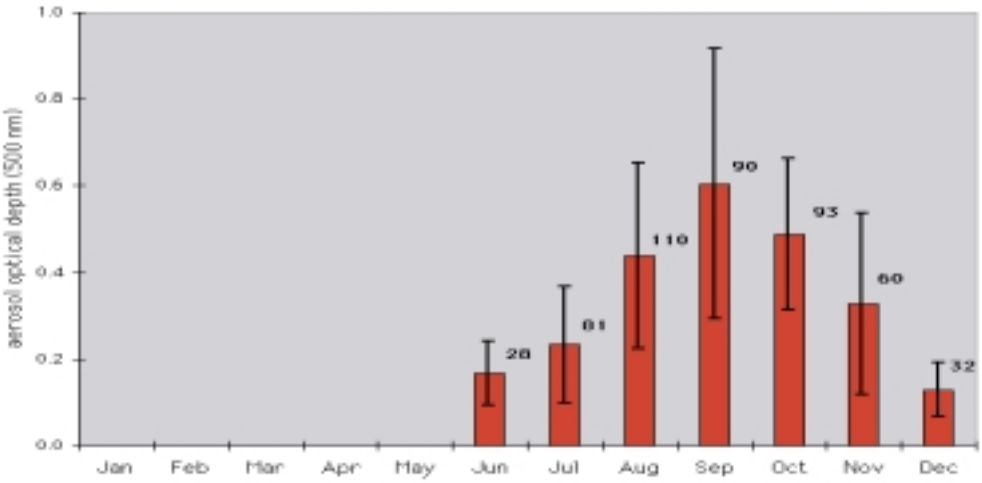

b)

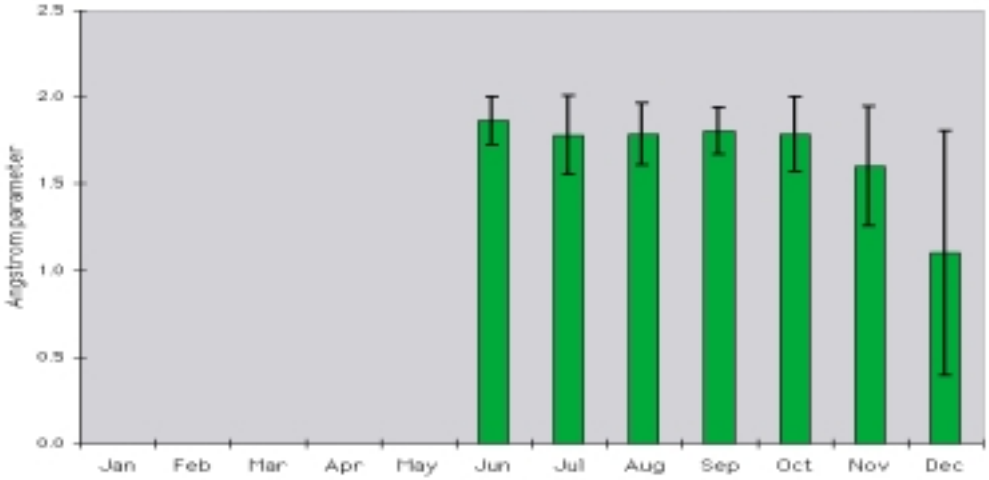

c)

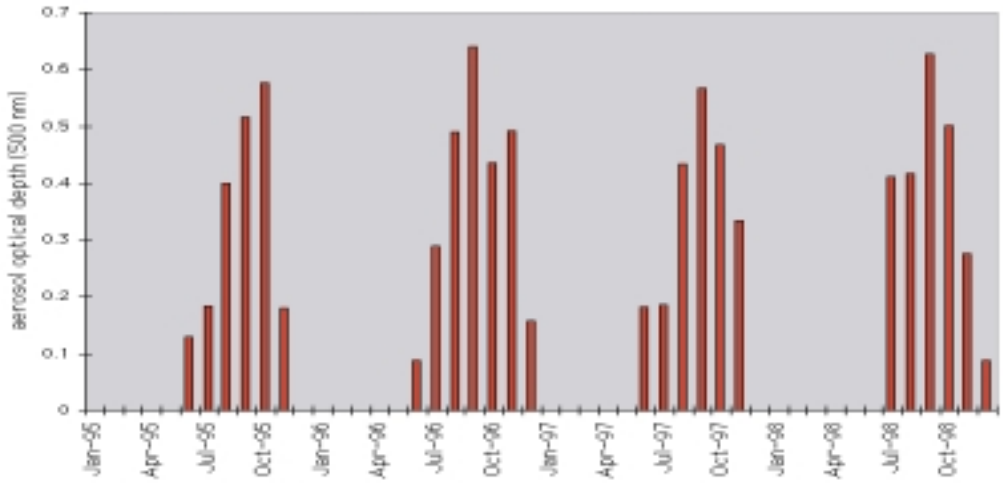

Fig.10

d)

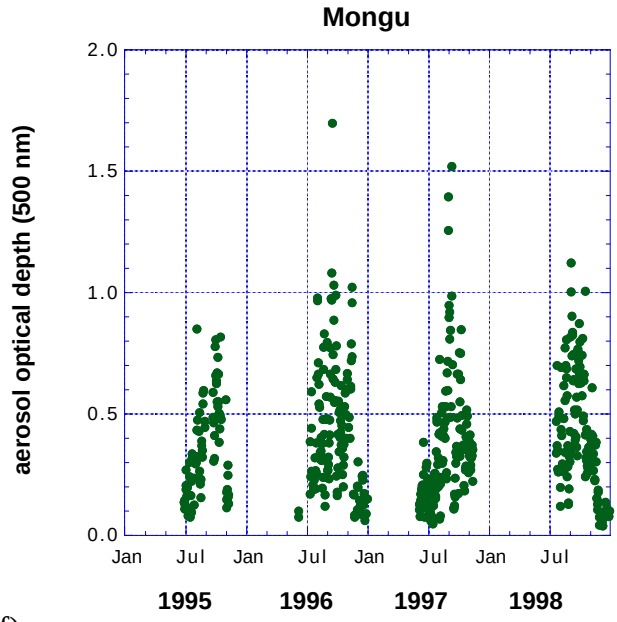

e)

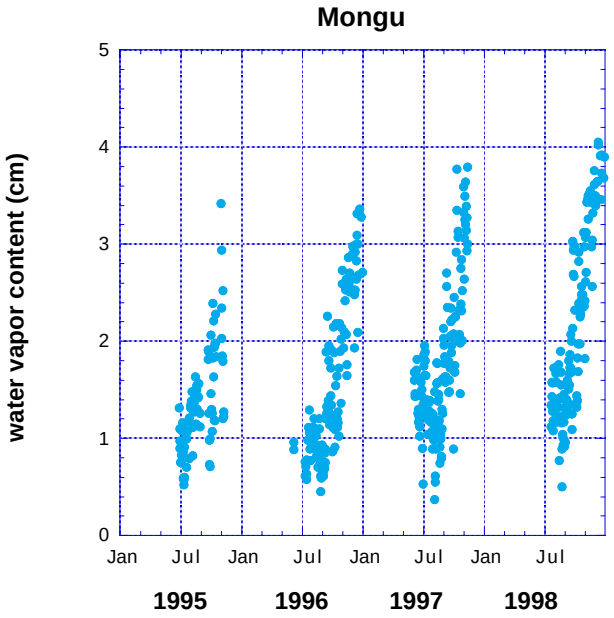

f)

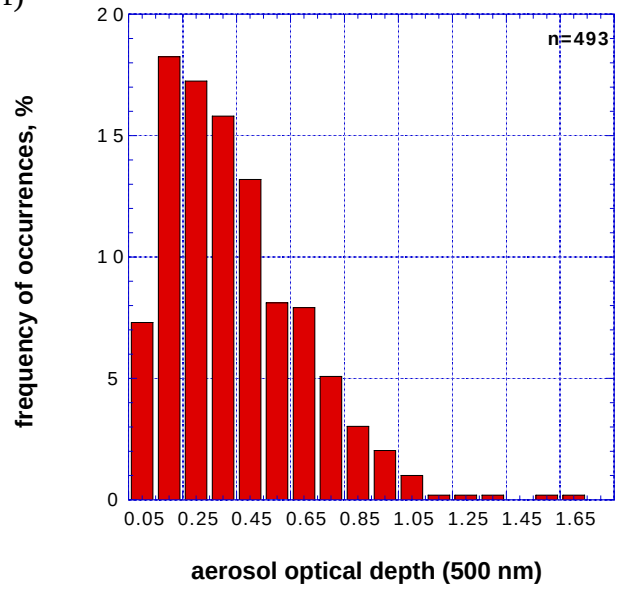

g)

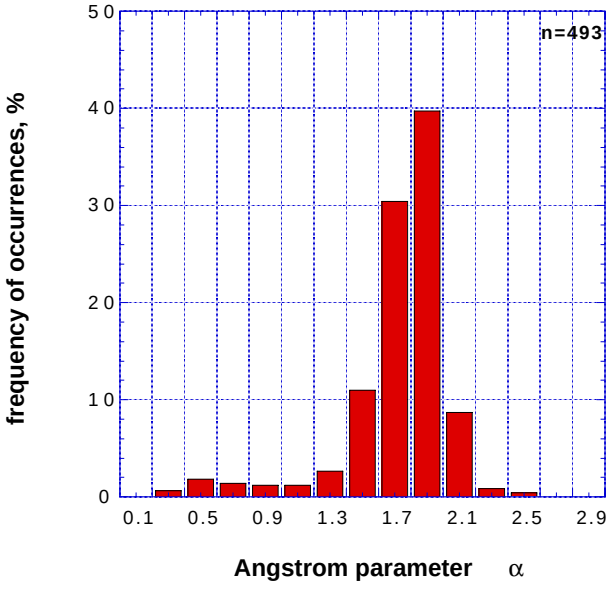

h)

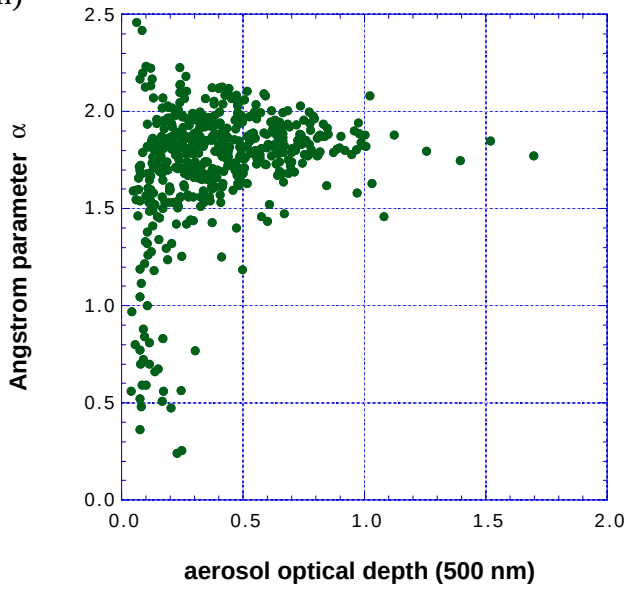

i)

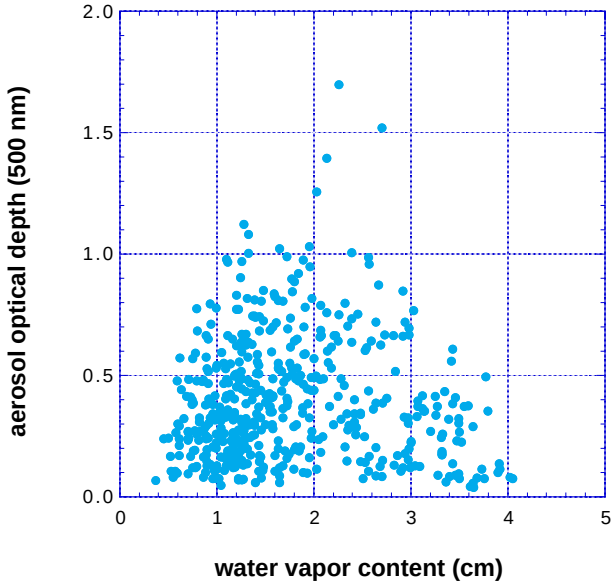

Figure 11

a)

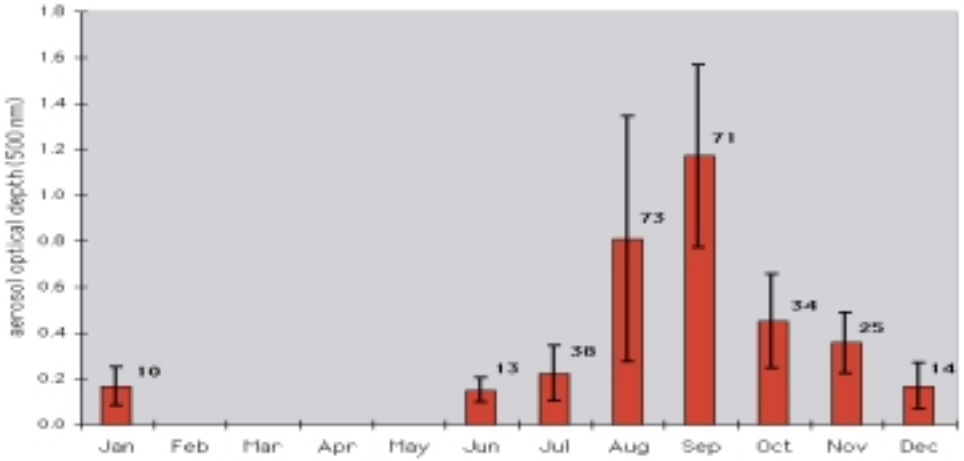

b)

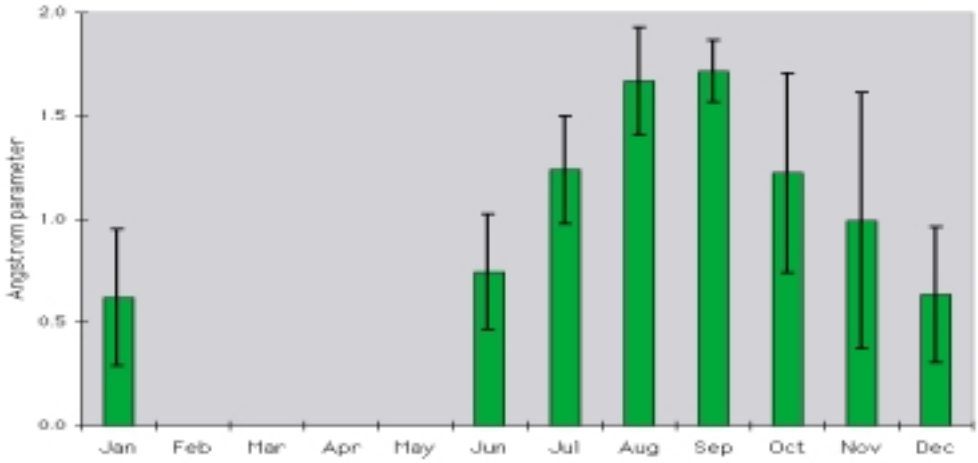

c)

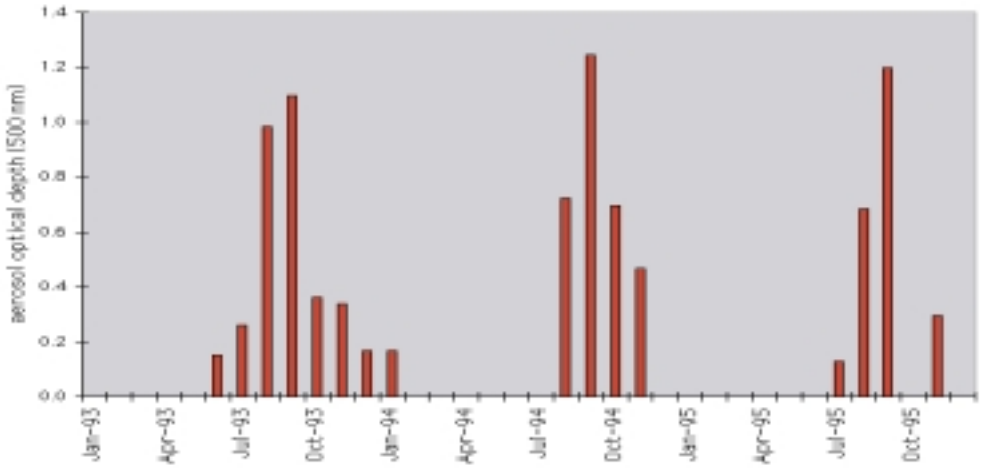

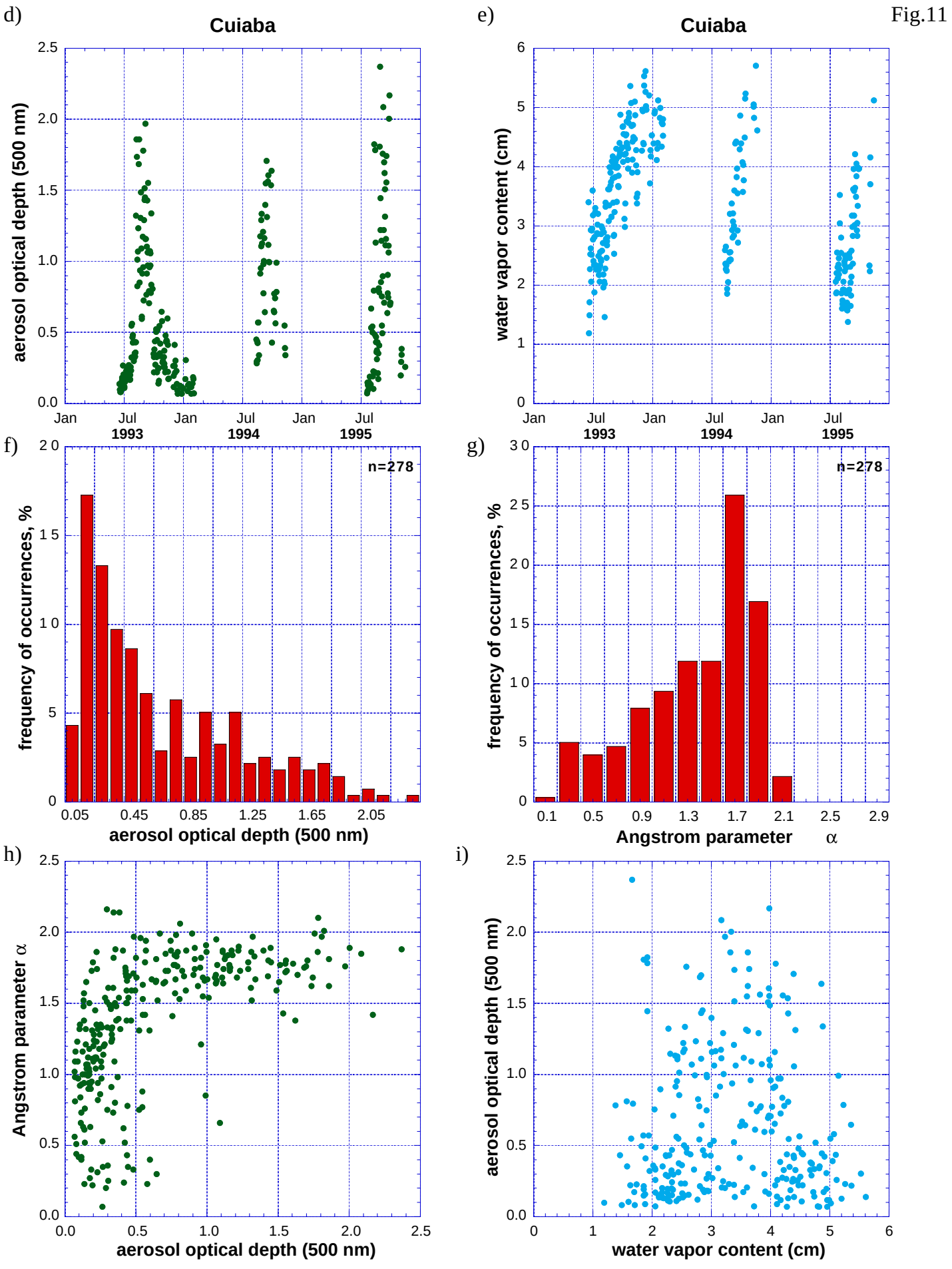
d)
Cuiaba
aerosol optical depth (500 nm)
Jan
Jul
1993
Jan
Jul
1994
Jan
Jul
1995
e)
Cuiaba
water vapor content (cm)
f)
n=278
frequency of occurrences, %
aerosol optical depth (500 nm)
g)
n=278
frequency of occurrences, %
Angstrom parameter α
h)
Angstrom parameter α
aerosol optical depth (500 nm)
i)
aerosol optical depth (500 nm)
water vapor content (cm)

Figure 12

a)

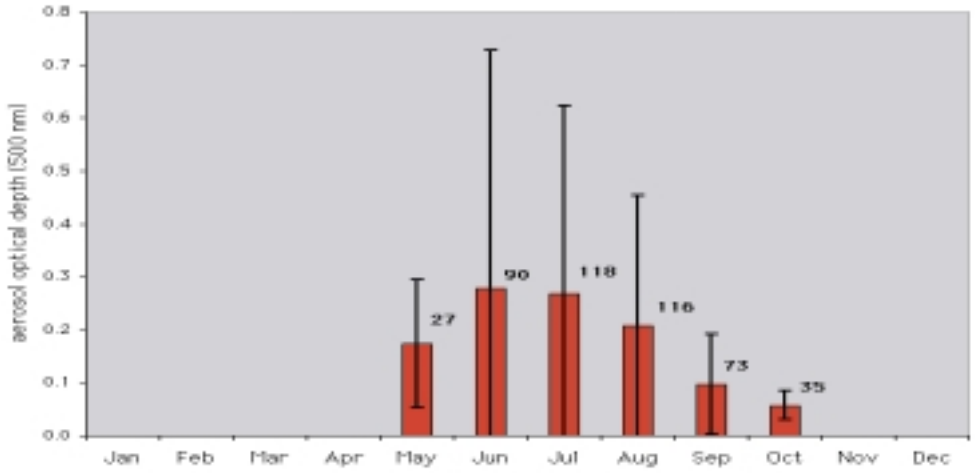

b)

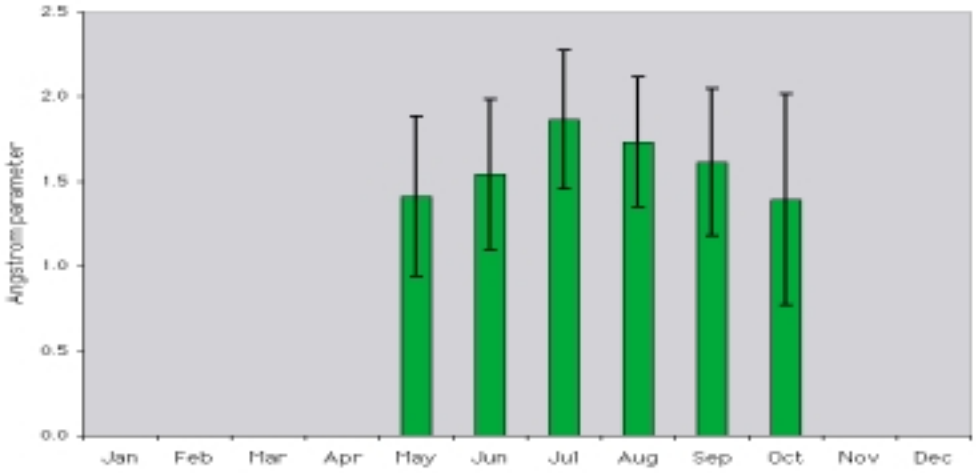

c)

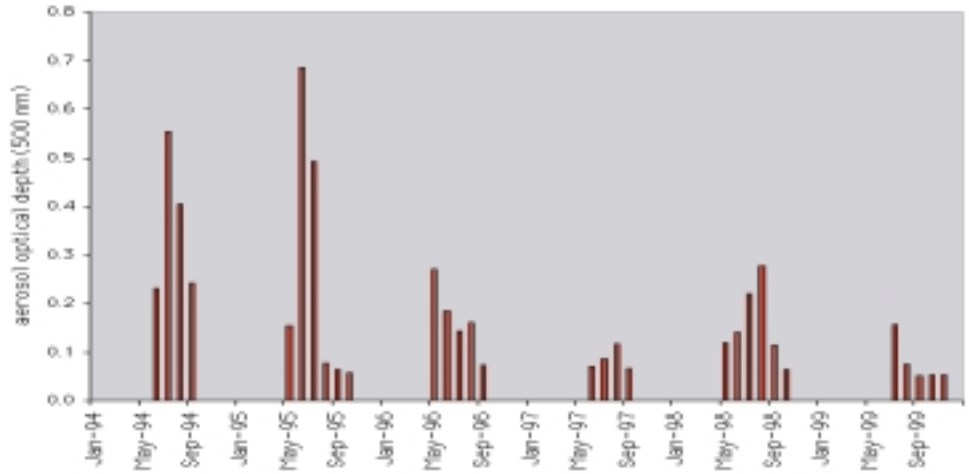

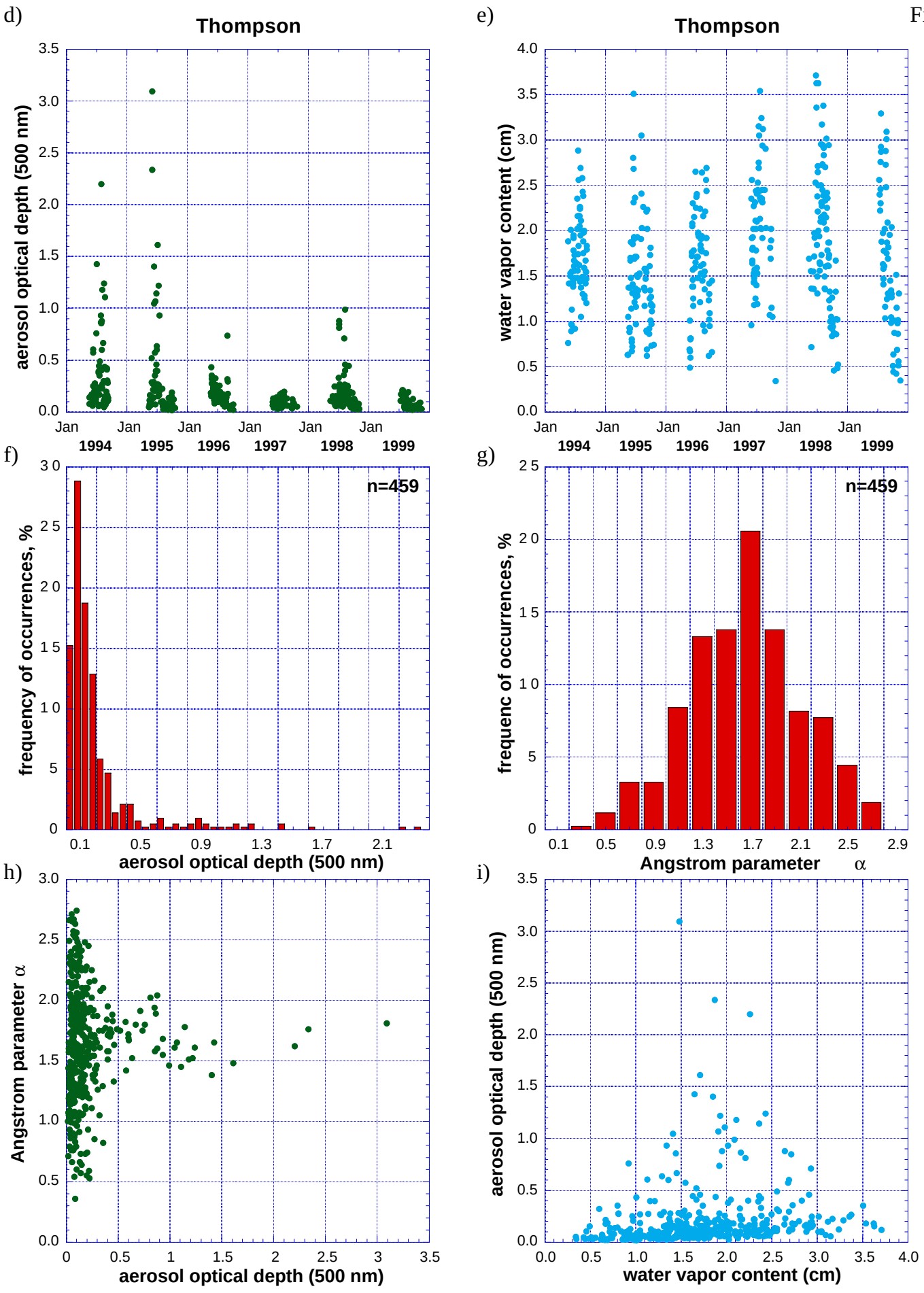
d)
Thompson
aerosol optical depth (500 nm)
Jan 1994
Jan 1995
Jan 1996
Jan 1997
Jan 1998
Jan 1999
e)
Thompson
water vapor content (cm)
f)
n=459
frequency of occurrences, %
aerosol optical depth (500 nm)
g)
n=459
frequenc of occurrences, %
Angstrom parameter α
h)
Angstrom parameter α
aerosol optical depth (500 nm)
i)
aerosol optical depth (500 nm)
water vapor content (cm)

Table 1. Summary of existing aerosol optical depth measurements from network related sources

Reference	Coverage (#sites)	Temporal	Comment
Forgan et al. [1994]	Global (95)	1971-1986	Unverifiable
Ben Mohamed et al. [1992]	Niger (7)	1986-1987	Accuracy ~0.05 est.
D'Almeida [1987]	W. Africa (11)	1980-1984	
Dutton et al. [1994]	Background (4)	1977-1992	Pyroheliometer, accuracy ~0.04
Flowers et al. [1969]	USA (43)	1960-1966	500 nm, accuracy ~0.04
Forgan [2000]	Australia (7)	1990 to present	Accuracy ~0.01
Gushchin [1988]	Soviet Union (33)	1968 to 1984	Accuracy ~0.03
Holben et al. [1991]	W. Africa (15)	1985-1986	Accuracy ~0.05
Holben et al. [1998]	Global (~100)	From 1993 to present	QA, accuracy ~0.015
Michalsky et al. [1994]	east USA (11)	From 1992 to present	QA, accuracy ~0.015
Herber et al. [1993]	Antarctica (5)	1956 to 1992)	Various inst.
Roosen et al. [1973]	N &S. America, Africa (13)	1905-1922	Smithsonian observatories
Smirnov et al. [1995]	Global Oceans	1967 to 1994	56 references
Smirnov et al. [1996]	Canada (4)	1986 to 1992	500 nm, accuracy ~0.02
SKYNET (Takamura)	East Asia (8)	1996 to present	
Bigelow et al. [1998]	USA (40)	1995 to present	Unverifiable
Jinhuan and Liquan, (2000)	China (5 cities)	1980-1994	Pyroheliometer, broad-band
Shaw [1982]	Polar regions (5)	1912-1982	Various sites, techniques
Volz [1969]	Central Europe (30)	1961-1965	500 nm, accuracy~0.04

Table 2. Database Summary for Measuring Period for Mauna Loa Observatory, Hawaii (Lat 19°32′N Long 155°34′W, elevation 3397 m), 1994-1999. Aerosol Optical Depth at 500 nm (τ_{a500}), Angstrom Expenent (α), Precipitable Water (PW), the Associated Standard Deviations (σ), the Number of Days (N) and Months (Mo.) in the observation Periods.

	τ_{a500}	σ	α	σ	PW	σ	N	Mo.
Jan	0.015	0.006	1.77	0.41	0.22	0.17	57	3
Feb	0.017	0.009	1.68	0.42	0.23	0.18	62	3
Mar	0.033	0.022	1.39	0.51	0.21	0.11	98	5
Apr	0.033	0.018	1.32	0.41	0.20	0.11	90	4
May	0.030	0.022	1.14	0.45	0.32	0.14	109	5
Jun	0.020	0.008	1.35	0.48	0.32	0.14	120	6
Jul	0.014	0.005	1.57	0.51	0.25	0.14	53	4
Aug	0.013	0.004	1.78	0.42	0.30	0.15	75	4
Sep	0.014	0.005	1.63	0.38	0.26	0.11	65	4
Oct	0.017	0.009	1.32	0.62	0.32	0.18	87	5
Nov	0.017	0.012	1.48	0.59	0.36	0.22	91	5
Dec	0.015	0.010	1.62	0.54	0.31	0.22	57	4
YEAR	0.020	0.008	1.50	0.20	0.27	0.05	964	52

Table 3. Database Summary for Measuring Period for Goddard Space Flight Center, Greenbelt, Maryland (Lat 39°01′N Long 76°52′W, elevation 50 m), 1993-1999. Parameters as in Table 2.

	τ_{a500}	σ	α	σ	PW	σ	N	Mo.
Jan	0.10	0.06	1.70	0.37	0.87	0.54	72	5
Feb	0.12	0.06	1.48	0.37	0.72	0.29	78	6
Mar	0.14	0.08	1.50	0.34	0.94	0.57	96	6
Apr	0.19	0.10	1.41	0.34	1.19	0.63	119	6
May	0.21	0.10	1.49	0.33	1.81	0.74	110	7
Jun	0.37	0.23	1.65	0.29	2.80	0.99	120	7
Jul	0.48	0.29	1.75	0.28	3.42	0.94	142	7
Aug	0.44	0.28	1.76	0.27	3.15	0.91	135	7
Sep	0.31	0.26	1.76	0.27	2.49	0.89	120	7
Oct	0.15	0.12	1.65	0.35	1.50	0.59	114	7
Nov	0.11	0.08	1.70	0.30	1.05	0.59	112	7
Dec	0.09	0.06	1.78	0.37	0.89	0.57	107	7
YEAR	0.23	0.14	1.64	0.13	1.73	0.98	1325	79

Table 4. Database Summary for Measuring Period for Sevilleta, New Mexico (Lat 34°21′N Long 106°53′W, elevation 1447 m), 1994-1999. Parameters as in Table 2.

	τ_{a500}	σ	α	σ	PW	σ	N	Mo.
Jan	0.03	0.02	1.26	0.54	0.58	0.18	87	4
Feb	0.04	0.03	1.35	0.54	0.65	0.25	82	4
Mar	0.06	0.04	1.07	0.36	0.65	0.23	106	4
Apr	0.08	0.04	0.91	0.35	0.61	0.23	66	4
May	0.09	0.04	0.97	0.30	0.91	0.35	118	6
Jun	0.10	0.05	1.24	0.28	1.31	0.52	150	6
Jul	0.11	0.05	1.38	0.28	2.19	0.72	153	6
Aug	0.12	0.05	1.67	0.32	2.43	0.46	168	6
Sep	0.10	0.07	1.57	0.37	1.85	0.55	151	6
Oct	0.07	0.03	1.40	0.45	0.96	0.41	139	6
Nov	0.05	0.03	1.49	0.52	0.69	0.23	98	5
Dec	0.05	0.04	1.46	0.37	0.59	0.20	89	5
YEAR	0.07	0.03	1.31	0.23	1.12	0.67	1407	62

Table 5. Database Summary for Measuring Period for HJAndrews, Oregon (Lat 44°14′N Long 122°13′W, elevation 830 m), 1994-1999. Parameters as in Table 2.

	τ_{a500}	σ	α	σ	PW	σ	N	Mo.
Jan	...	...	...	...	...	...	...	…
Feb	...	...	...	...	...	...	...	…
Mar	...	...	...	...	...	...	...	…
Apr	...	...	...	...	...	...	...	…
May	0.15	0.09	1.52	0.26	1.12	0.34	10	2
Jun	0.08	0.05	1.53	0.26	1.41	0.43	61	4
Jul	0.08	0.06	1.67	0.28	1.61	0.39	129	5
Aug	0.10	0.09	1.61	0.22	1.65	0.50	112	5
Sep	0.07	0.06	1.43	0.39	1.32	0.33	101	5
Oct	0.07	0.07	1.18	0.51	1.07	0.35	72	5
Nov	0.04	0.03	1.18	0.52	0.89	0.35	19	3
Dec	0.04	0.02	0.74	0.52	0.82	0.32	10	1
YEAR	...	...	...	...	...	...	514	30

Table 6. Database Summary for Cape Verde (Lat 16°43′N Long 22°56′W, elevation 60 m), 1994-1999. Parameters as in Table 2.

	τ_{a500}	σ	α	σ	PW	σ	N	Mo.
Jan	0.36	0.30	0.39	0.27	1.96	0.83	55	5
Feb	0.44	0.30	0.25	0.12	1.93	0.90	77	5
Mar	0.27	0.35	0.55	0.32	2.09	0.70	75	4
Apr	0.26	0.12	0.58	0.29	2.21	0.79	59	3
May	0.40	0.32	0.37	0.31	2.39	0.72	76	4
Jun	0.68	0.29	0.16	0.09	3.10	0.71	46	3
Jul	0.60	0.20	0.18	0.08	3.53	0.93	46	3
Aug	0.41	0.20	0.21	0.11	3.90	0.89	44	3
Sep	0.48	0.38	0.23	0.15	3.70	0.83	47	3
Oct	0.28	0.23	0.32	0.21	3.33	0.80	68	4
Nov	0.33	0.24	0.39	0.27	2.39	0.74	78	4
Dec	0.30	0.20	0.36	0.32	1.81	0.67	55	3
YEAR	0.40	0.13	0.33	0.14	2.69	0.76	726	44

Table 7. Database Summary for Banizoumbou, Niger (Lat 32°22′N Long 02°39′E, elevation 250 m), 1995-1997. Parameters as in Table 2.

	τ_{a500}	σ	α	σ	PW	σ	N	Mo.
Jan	0.47	0.50	0.31	0.26	1.15	0.48	25	1
Feb	0.71	0.50	0.15	0.08	0.96	0.19	41	2
Mar	0.47	0.26	0.09	0.07	1.64	0.60	17	1
Apr	0.76	0.33	0.09	0.05	2.22	0.90	21	1
May	0.41	0.20	0.06	0.07	3.34	1.03	21	1
Jun	0.53	0.33	0.06	0.07	4.19	0.37	32	2
Jul	0.52	0.24	0.13	0.14	4.30	0.47	42	2
Aug	0.39	0.18	0.22	0.16	4.68	0.38	25	1
Sep	0.33	0.12	0.20	0.16	4.38	0.33	23	1
Oct	0.59	0.46	0.18	0.12	2.87	0.94	57	3
Nov	0.39	0.36	0.25	0.14	1.24	0.52	55	2
Dec	0.24	0.14	0.51	0.27	1.24	0.43	57	2
YEAR	0.48	0.15	0.19	0.13	2.68	1.45	416	19

Table 8. Database Summary for Mongu, Zambia (Lat 15°15′S Long 23°09′E, elevation 1107 m), 1995-1998. Parameters as in Table 2.

	τ_{a500}	σ	α	σ	PW	σ	N	Mo.
Jan	...	...	...	...	...	...	...	...
Feb	...	...	...	...	...	...	...	...
Mar	...	...	...	...	...	...	...	...
Apr	...	...	...	...	...	...	...	...
May	...	...	...	...	...	...	...	...
Jun	0.17	0.07	1.86	0.14	1.31	0.27	28	3
Jul	0.23	0.13	1.78	0.23	1.13	0.34	81	4
Aug	0.44	0.21	1.79	0.18	1.16	0.34	110	4
Sep	0.60	0.31	1.80	0.14	1.58	0.57	90	4
Oct	0.49	0.18	1.79	0.22	2.03	0.66	93	4
Nov	0.33	0.21	1.60	0.34	2.80	0.68	60	4
Dec	0.13	0.06	1.10	0.71	3.19	0.55	32	2
YEAR	...	...	...	...	...	...	494	25

Table 9. Database Summary for Measuring Period for Cuiaba, Brazil (Lat 15°30′S Long 56°00′W, elevation 250 m), 1993-1995. Parameters as in Table 2.

	τ_{a500}	σ	α	σ	PW	σ	N	Mo.
Jan	0.17	0.09	0.62	0.33	4.59	0.32	10	1
Feb	...	...	...	...	...	...	...	...
Mar	...	...	...	...	...	...	...	...
Apr	...	...	...	...	...	...	...	...
May	...	...	...	...	...	...	...	...
Jun	0.15	0.05	0.74	0.28	2.47	0.72	13	1
Jul	0.22	0.12	1.24	0.26	2.50	0.40	38	2
Aug	0.81	0.54	1.67	0.26	2.52	0.71	73	3
Sep	1.17	0.40	1.72	0.15	3.46	0.73	71	3
Oct	0.45	0.20	1.22	0.48	4.32	0.56	34	2
Nov	0.36	0.13	0.99	0.62	4.26	0.82	25	3
Dec	0.17	0.10	0.63	0.33	…	…	14	1
YEAR	...	...	...	...	...	...	273	16

Table 10. Database Summary for Measuring Period for Thompson, Canada (Lat 55°47′N Long 97°50′W, elevation 218 m), 1994-1999. Parameters as in Table 2.

	τ_{a500}	σ	α	σ	PW	σ	N	Mo.
Jan	...	...	...	...	...	...	...	...
Feb	...	...	...	...	...	...	...	...
Mar	...	...	...	...	...	...	...	...
Apr	...	...	...	...	...	...	...	...
May	0.17	0.12	1.41	0.47	1.10	0.47	27	3
Jun	0.28	0.45	1.54	0.44	1.76	0.60	90	5
Jul	0.27	0.35	1.86	0.41	2.06	0.56	118	6
Aug	0.21	0.25	1.73	0.38	2.02	0.60	116	6
Sep	0.10	0.10	1.61	0.43	1.47	0.48	73	6
Oct	0.06	0.03	1.39	0.62	0.95	0.33	35	3
Nov	...	...	...	...	...	...	...	...
Dec	...	...	...	...	...	...	...	...
YEAR	...	...	...	...	...	...	459	29

Appendix

Approximately 100 sites comprise the AERONET network representing a wide diversity of aerosol regimes. We provide values of monthly and annual τ_{a500}, Angstrom exponent and PW for sites with two or more years of quality assured data. Annual means were not computed for seasonal sites. An exhaustive analysis of these twenty-one sites is not intended but rather a cursory inspection of these data clearly show seasonal trends, annual differences between sites and mixing of aerosol types which can be further influenced by water vapor.

The island sites of Lanai, Hawaii and San Nicholas Island, CA represent clean oceanic conditions with the mean annual τ_{a500} = 0.08 although the Lanai site has a decidedly lower Angstrom exponent indicative of marine aerosols. Bermuda (τ_{a500} =0.14), Dry Tortugas, FL (τ_{a500} =0.18), Kaashidhoo, Maldives (τ_{a500} =0.20) and Bahrain (τ_{a500} =0.32) clearly show elevated levels that are seasonally dependent due to influences of a variety of continental aerosol sources. The small desert coastal town of Arica, Chile has a high mean annual aerosol loading (τ_{a500} =0.31) yet the Angstrom exponent (1.27) is not typical of the expected aerosol type generated by either desert landscapes or marine aerosols. Desert aerosol influenced sites such as Ilorin, Nigeria (τ_{a500} =0.51), Bondoukoui, Burkina Faso (τ_{a500} =0.44), Bidi-Bahn, Burkina Faso (τ_{a500} =0.55) all have mean annual Angstrom exponents less than 0.8 however desert located sites such as Sede Boker, Israel (τ_{a500} =0.21) and Dalanzadgad, Mongolia (τ_{a500} =0.13) have Angstrom exponents indicative of seasonally variable particle sizes (0.94 and 1.14 respectively). Additionally the rural north American sites CART site, OK (τ_{a500} =0.17), Bondville, IL (τ_{a500} =0.19) and Sherbrooke, Quebec (τ_{a500} =0.12) all demonstrate a warm season peak and a narrow range of mean annual Angstrom exponent from 1.36, 1.42 and 1.56

respectively. Ispra, Italy (0.36) is influenced by a rather constant aerosol source year around as shown by high τ_{a500} each month and a small range in angstrom exponent for all months (mean $\alpha = 1.52$). Lastly the seasonal values from the forested boreal site, Waskesiu, Saskatchewan ($\tau_{a500} = 0.23$, $\alpha = 1.41$) and tropical forested sites, Alta Floresta ($\tau_{a500} = 1.48$, $\alpha = 1.66$), Brazil and Brasilia, Brazil ($\tau_{a500} = 0.56$, $\alpha = 1.44$) clearly respond to the warm/dry season influence of biomass burning as described in detail earlier.

Aerosol optical depth at 500 nm (τ_{a500}), Angstrom exponent (α), precipitable water (PW), the associated standard deviations (σ), the number of days (N) and months (Mo.) in the observation periods.

USA

Lanai, Hawaii (Lat 20°49′N Long 156°59′W, elevation 80 m), 1995-1999.

	τ_{a500}	σ	α	σ	PW	σ	N	Mo.
Jan	0.08	0.08	0.71	0.41	2.95	0.48	34	2
Feb	0.08	0.03	0.56	0.40	2.55	0.46	28	2
Mar	0.12	0.06	0.74	0.36	2.54	0.47	36	2
Apr	0.11	0.04	0.62	0.27	2.77	0.35	44	3
May	0.11	0.06	0.70	0.22	3.17	0.36	38	2
Jun	0.06	0.02	0.60	0.23	3.32	0.51	20	2
Jul	0.06	0.02	0.96	0.25	3.45	0.57	56	2
Aug	0.06	0.03	0.87	0.31	3.74	0.41	58	3
Sep	0.06	0.03	0.85	0.35	3.68	0.52	41	3
Oct	0.06	0.03	0.60	0.32	3.53	0.65	42	2
Nov	0.06	0.04	0.63	0.33	3.34	0.79	39	3
Dec	0.08	0.06	0.69	0.46	2.89	0.59	49	3
YEAR	0.08	0.02	0.71	0.12	3.16	0.42	485	29

San Nicolas Island, California (Lat 33°15′N Long 119°29′W, elevation 133 m), 1998-2000.

	τ_{a500}	σ	α	σ	PW	σ	N	Mo.
Jan	0.04	0.03	1.06	0.62	1.03	0.56	35	2
Feb	0.06	0.03	1.01	0.44	1.02	0.39	29	2
Mar	0.11	0.06	0.74	0.26	1.22	0.39	31	2
Apr	0.13	0.09	0.75	0.30	1.30	0.31	41	2
May	0.12	0.06	0.91	0.16	1.67	0.47	26	1
Jun	0.09	0.04	1.06	0.40	1.72	0.49	36	2
Jul	0.09	0.04	1.37	0.38	2.34	1.03	33	2
Aug	0.08	0.04	1.49	0.53	1.94	0.94	47	2
Sep	0.11	0.06	1.27	0.41	2.10	0.95	37	2
Oct	0.08	0.04	1.42	0.45	1.27	0.43	40	2
Nov	0.04	0.02	1.33	0.68	1.21	0.55	34	2
Dec	0.04	0.02	1.20	0.66	0.88	0.29	56	2
YEAR	0.08	0.03	1.13	0.25	1.48	0.47	445	23

Dry Tortugas, Florida (Lat 24°36′N Long 82°47′W, elevation 0 m), 1996-1999.

	τ_{a500}	σ	α	σ	PW	σ	N	Mo.
Jan	0.15	0.05	1.29	0.45	3.37	0.88	9	2
Feb	0.16	0.08	1.13	0.51	2.82	1.06	25	1
Mar	0.14	0.09	1.29	0.53	2.81	1.02	33	1
Apr	0.26	0.16	1.54	0.36	2.90	0.94	33	1
May	0.39	0.19	1.64	0.28	3.25	1.07	25	1
Jun	0.18	0.11	1.03	0.57	4.87	0.52	73	3
Jul	0.21	0.14	0.73	0.53	4.87	0.74	105	4
Aug	0.17	0.12	0.97	0.65	5.18	0.78	89	4
Sep	0.20	0.15	1.07	0.67	4.88	1.10	76	4
Oct	0.11	0.05	0.97	0.58	4.35	1.18	47	2
Nov	0.12	0.04	0.99	0.43	3.41	1.00	42	2
Dec	0.11	0.04	0.75	0.51	3.30	0.98	31	2
YEAR	0.18	0.08	1.12	0.28	3.83	0.92	588	27

CART site, Oklahoma (Lat 36°36′N Long 97°24′W, elevation 315 m), 1994-1999.

	τ_{a500}	σ	α	σ	PW	σ	N	Mo.
Jan	0.08	0.06	1.39	0.23	1.00	0.38	8	1
Feb	0.08	0.06	1.18	0.39	0.87	0.26	18	1
Mar	0.20	0.10	1.36	0.22	1.15	0.47	10	1
Apr	0.16	0.10	1.03	0.46	1.43	0.64	59	4
May	0.36	0.22	1.27	0.23	2.54	0.72	27	1
Jun	0.19	0.08	1.32	0.23	3.55	0.92	19	1
Jul	0.20	0.06	1.32	0.34	4.61	0.70	15	1
Aug	0.28	0.14	1.57	0.32	3.82	0.67	27	1
Sep	0.22	0.16	1.42	0.39	3.34	1.06	50	3
Oct	0.14	0.11	1.58	0.28	2.38	0.84	23	2
Nov	0.06	0.06	1.22	0.27	1.19	0.41	7	1
Dec	0.07	0.06	1.71	0.22	1.08	0.75	12	1
YEAR	0.17	0.05	1.36	0.19	2.25	1.31	275	18

Bondville, Illinois (Lat 40°03′N Long 88°22′W, elevation 212 m), 1996-1999.

	τ_{a500}	σ	α	σ	PW	σ	N	Mo.
Jan	0.06	0.03	1.35	0.42	0.37	0.04	3	1
Feb	0.08	0.06	1.26	0.22	0.84	0.63	13	1
Mar	0.14	0.06	1.36	0.25	0.88	0.64	31	2
Apr	0.19	0.13	1.37	0.37	1.41	0.54	32	2
May	0.31	0.28	1.24	0.33	2.19	0.75	43	2
Jun	0.31	0.23	1.41	0.45	3.10	0.96	45	3
Jul	0.29	0.18	1.59	0.35	3.48	0.99	49	3
Aug	0.33	0.25	1.62	0.32	2.92	0.77	78	4
Sep	0.30	0.31	1.42	0.47	2.39	0.99	89	4
Oct	0.16	0.10	1.48	0.48	1.54	0.72	79	4
Nov	0.09	0.08	1.42	0.39	0.91	0.47	19	2
Dec	0.06	0.02	1.52	0.22	0.58	0.27	17	1
YEAR	0.19	0.11	1.42	0.12	1.72	1.07	498	29

Canada

Sherbrooke, Quebec (Lat 45°22′N Long 71°55′W, elevation 300 m), 1995, 1998-2000.

	τ_{a500}	σ	α	σ	PW	σ	N	Mo.
Jan	0.07	0.03	1.55	0.73	0.38	0.45	9	2
Feb	0.07	0.04	1.63	0.95	0.29	0.14	14	2
Mar	0.11	0.04	1.27	0.34	0.58	0.14	10	2
Apr	0.09	0.06	1.46	0.45	0.76	0.26	20	1
May	0.13	0.06	1.20	0.35	1.70	0.70	18	1
Jun	0.23	0.17	1.48	0.39	2.07	0.85	39	2
Jul	0.22	0.15	1.66	0.38	2.59	0.77	44	2
Aug	0.15	0.16	1.57	0.40	2.15	0.66	60	3
Sep	0.10	0.10	1.26	0.54	1.56	0.68	26	3
Oct	0.09	0.05	1.66	0.46	1.11	0.44	34	3
Nov	0.06	0.03	1.97	0.63	0.91	0.56	13	3
Dec	0.06	0.03	2.03	0.43	0.42	0.23	6	1
YEAR	0.12	0.06	1.56	0.26	1.21	0.78	293	25

Waskesiu, Saskatchewan (Lat 53°55′N Long 106°04′W, elevation 550 m), 1994-1999.

	τ_{a500}	σ	α	σ	PW	σ	N	Mo.
Jan	…	…	…	…	…	…	…	…
Feb	…	…	…	…	…	…	…	…
Mar	…	…	…	…	…	…	…	…
Apr	…	…	…	…	…	…	…	…
May	0.19	0.11	1.40	0.35	1.19	0.48	49	4
Jun	0.23	0.27	1.41	0.39	1.61	0.51	93	4
Jul	0.20	0.24	1.50	0.43	2.03	0.53	133	5
Aug	0.18	0.20	1.55	0.41	1.95	0.48	144	6
Sep	0.07	0.05	1.35	0.48	1.40	0.40	112	5
Oct	0.06	0.05	1.24	0.50	0.95	0.36	68	5
Nov	0.04	0.03	1.37	0.54	0.75	0.34	16	1
Dec	0.03	0.02	1.43	0.43	0.44	0.13	6	1
YEAR	…	…	…	…	…	…	621	31

Brazil

Alta Floresta (Lat 09°55′S Long 56°00′W, elevation 175 m), 1993-1995, 1999.

	τ_{a500}	σ	α	σ	PW	σ	N	Mo.
Jan	0.09	0.03	0.66	0.24	5.41	0.12	4	1
Feb	0.08	0.04	0.57	0.27	5.22	0.29	13	1
Mar	0.11	0.12	0.74	0.51	5.10	0.41	8	1
Apr	0.09	0.04	0.98	0.46	4.82	0.55	17	1
May	0.10	0.06	1.21	0.53	4.61	0.52	23	1
Jun	0.11	0.04	1.30	0.62	3.69	0.69	29	2
Jul	0.16	0.12	1.50	0.46	2.94	0.44	55	2
Aug	1.18	0.65	1.89	0.24	2.84	0.55	81	4
Sep	1.48	0.73	1.66	0.28	4.19	0.65	80	4
Oct	0.63	0.24	1.50	0.26	4.76	0.43	31	2
Nov	…	…	…	…	…	…	…	…
Dec	…	…	…	…	…	…	…	…
YEAR	…	…	…	…	…	…	341	19

Brasilia (Lat 15°55′S Long 47°54′W, elevation 1100 m), 1993-1995.

	τ_{a500}	σ	α	σ	PW	σ	N	Mo.
Jan	…	…	…	…	…	…	…	…
Feb	0.11	0.06	1.04	0.23	2.51	0.25	4	1
Mar	…	…	…	…	…	…	…	…
Apr	0.07	0.03	0.77	0.14	2.99	0.29	7	1
May	0.10	0.03	1.12	0.18	2.60	0.16	12	1
Jun	0.08	0.04	0.95	0.32	1.74	0.51	63	3
Jul	0.09	0.07	0.96	0.27	1.70	0.27	71	3
Aug	0.23	0.23	1.15	0.35	1.56	0.41	76	3
Sep	0.56	0.36	1.44	0.29	2.10	0.69	52	2
Oct	0.35	0.21	1.32	0.42	2.60	0.46	27	2
Nov	0.16	0.08	0.83	0.45	2.89	0.55	19	2
Dec	0.14	0.04	0.64	0.34	3.21	0.41	6	1
YEAR	…	…	…	…	…	…	337	19

Bolivia

Los Fierros (Lat 14°33′S Long 60°55′W, elevation 170 m), 1996, 1998-1999.

	τ_{a500}	σ	α	σ	PW	σ	N	Mo.
Jan	…	…	…	…	…	…	…	…
Feb	…	…	…	…	…	…	…	…
Mar	…	…	…	…	…	…	…	…
Apr	…	…	…	…	…	…	…	…
May	0.08	0.02	1.16	0.25	4.22	1.11	26	2
Jun	0.14	0.07	1.52	0.21	4.25	0.54	33	2
Jul	0.19	0.09	1.69	0.17	3.23	0.51	75	3
Aug	1.07	0.80	1.88	0.16	3.58	0.90	90	3
Sep	1.16	0.68	1.86	0.11	3.86	0.65	43	2
Oct	1.02	0.48	1.75	0.23	4.56	0.74	27	2
Nov	0.24	0.07	1.03	0.35	5.06	0.44	16	1
Dec	…	…	…	…	…	…	…	…
YEAR	…	…	…	…	…	…	310	15

Chile

Arica (Lat 18°28′S Long 70°15′W, elevation 25 m), 1998-1999.

	τ_{a500}	σ	α	σ	PW	σ	N	Mo.
Jan	0.27	0.14	1.42	0.16	3.28	0.82	30	1
Feb	0.45	0.20	1.29	0.22	5.04	0.35	24	1
Mar	0.45	0.17	1.32	0.31	4.69	0.37	31	1
Apr	0.32	0.10	1.43	0.12	3.01	0.62	24	1
May	0.27	0.09	1.26	0.22	2.15	0.37	46	2
Jun	0.24	0.07	1.25	0.24	1.97	0.38	49	2
Jul	0.24	0.07	1.17	0.22	2.13	0.34	52	2
Aug	0.32	0.13	1.13	0.18	1.88	0.28	47	2
Sep	0.31	0.09	1.18	0.10	1.84	0.35	29	1
Oct	0.24	0.07	1.24	0.12	1.98	0.17	26	1
Nov	0.27	0.08	1.25	0.17	2.50	0.47	30	1
Dec	0.33	0.14	1.26	0.14	3.07	0.98	28	1
YEAR	0.31	0.07	1.27	0.09	2.79	1.09	416	16

Bermuda (Lat 32°22′N Long 64°41′W, elevation 10 m), 1996-1999.

	τ_{a500}	σ	α	σ	PW	σ	N	Mo.
Jan	0.10	0.06	0.87	0.45	2.13	0.50	16	2
Feb	0.14	0.06	0.80	0.35	1.84	0.28	20	2
Mar	0.13	0.05	0.98	0.31	1.89	0.46	44	3
Apr	0.18	0.07	0.98	0.31	2.02	0.52	59	3
May	0.24	0.16	1.09	0.33	3.05	0.62	59	3
Jun	0.19	0.12	1.10	0.46	3.56	0.75	48	3
Jul	0.17	0.12	0.90	0.42	4.45	0.74	63	3
Aug	0.11	0.06	0.86	0.39	4.91	0.54	75	3
Sep	0.14	0.08	0.93	0.50	4.20	0.90	52	3
Oct	0.11	0.06	0.78	0.44	2.93	0.72	55	4
Nov	0.10	0.04	0.84	0.45	2.43	0.54	63	4
Dec	0.13	0.08	0.92	0.48	2.35	0.63	28	3
YEAR	0.14	0.04	0.92	0.10	2.98	1.07	582	36

Nigeria

Ilorin (Lat 08°19′N Long 04°20′W, elevation 350 m), 1998-1999.

	τ_{a500}	σ	α	σ	PW	σ	N	Mo.
Jan	0.90	0.34	1.02	0.18	2.85	0.64	30	1
Feb	0.76	0.19	0.71	0.25	3.14	0.95	24	1
Mar	0.48	0.19	0.54	0.26	4.24	0.35	23	1
Apr	0.70	0.41	0.34	0.17	4.51	0.67	32	2
May	0.43	0.22	0.38	0.25	4.95	0.58	50	2
Jun	0.45	0.19	0.50	0.28	4.89	0.39	40	2
Jul	0.27	0.16	0.92	0.43	5.06	0.28	19	2
Aug	0.27	0.05	1.32	0.25	4.78	0.28	8	2
Sep	0.34	0.19	0.75	0.46	5.02	0.27	11	1
Oct	0.33	0.27	0.78	0.31	4.53	0.71	24	1
Nov	0.37	0.12	0.80	0.25	3.35	0.30	28	1
Dec	0.80	0.41	0.90	0.38	2.60	0.81	25	1
YEAR	0.51	0.22	0.75	0.28	4.16	0.91	314	17

Burkina Faso

Bondoukoui (Lat 11°50′N Long 03°45′W, elevation 0 m), 1996-1997.

	τ_{a500}	σ	α	σ	PW	σ	N	Mo.
Jan	0.32	0.20	0.77	0.33	1.47	0.46	24	1
Feb	0.71	0.60	0.22	0.11	1.05	0.44	46	2
Mar	0.80	0.55	0.26	0.16	1.95	0.94	38	2
Apr	0.56	0.33	0.18	0.11	3.02	1.04	29	2
May	0.48	0.52	0.15	0.15	3.73	0.89	49	2
Jun	0.38	0.21	0.17	0.17	4.17	0.36	45	2
Jul	0.39	0.16	0.24	0.18	4.32	0.41	32	2
Aug	0.31	0.19	0.48	0.40	4.68	0.36	27	1
Sep	0.30	0.16	0.43	0.27	4.53	0.28	19	1
Oct	0.39	0.25	0.27	0.20	3.81	0.55	28	1
Nov	0.30	0.17	0.78	0.36	1.95	0.75	39	2
Dec	0.36	0.34	0.78	0.35	1.24	0.48	59	2
YEAR	0.44	0.17	0.39	0.25	2.99	1.38	435	20

Bidi-Bahn (Lat 14°03′N Long 02°27′W, elevation 0 m), 1996-1997.

	τ_{a500}	σ	α	σ	PW	σ	N	Mo.
Jan	0.43	0.49	0.65	0.42	2.01	0.64	25	1
Feb	0.93	0.70	0.18	0.07	1.43	0.24	31	2
Mar	0.60	0.49	0.25	0.13	2.20	0.98	51	2
Apr	0.41	0.29	0.31	0.27	2.52	1.11	50	2
May	0.91	0.67	0.09	0.08	4.29	1.07	28	1
Jun	0.63	0.36	0.10	0.09	4.86	0.50	46	2
Jul	0.59	0.26	0.23	0.19	5.18	0.50	53	2
Aug	0.55	0.27	0.31	0.24	5.58	0.43	36	2
Sep	0.52	0.29	0.37	0.15	5.34	0.43	26	2
Oct	0.52	0.32	0.24	0.08	3.50	1.01	28	1
Nov	0.34	0.29	0.31	0.14	1.61	0.32	28	1
Dec	0.20	0.14	0.72	0.30	1.59	0.61	28	1
YEAR	0.55	0.21	0.31	0.19	3.34	1.63	430	19

Israel

Sede Boker (Lat 30°31′N Long 34°28′E, elevation 480 m), 1996, 1998-1999.

	τ_{a500}	σ	α	σ	PW	σ	N	Mo.
Jan	0.19	0.17	1.20	0.62	1.06	0.35	29	2
Feb	0.21	0.28	1.02	0.69	0.83	0.25	29	3
Mar	0.20	0.13	0.95	0.63	1.03	0.23	48	3
Apr	0.27	0.13	0.74	0.44	0.96	0.17	26	2
May	0.25	0.17	0.42	0.23	1.21	0.33	27	2
Jun	0.17	0.06	0.87	0.37	1.49	0.40	56	3
Jul	0.23	0.09	1.06	0.32	1.85	0.48	64	3
Aug	0.23	0.08	1.12	0.31	2.02	0.48	85	3
Sep	0.22	0.08	0.91	0.40	2.13	0.45	71	3
Oct	0.22	0.07	1.02	0.36	2.03	0.44	44	2
Nov	0.19	0.10	0.90	0.39	1.45	0.43	42	3
Dec	0.11	0.05	1.04	0.37	1.09	0.37	26	2
YEAR	0.21	0.04	0.94	0.21	1.43	0.47	547	31

Italy

Ispra (Lat 45°48′N Long 08°37′E, elevation 235 m), 1997-1998.

	τ_{a500}	σ	α	σ	PW	σ	N	Mo.
Jan	0.25	0.20	1.53	0.34	0.87	0.19	12	1
Feb	0.34	0.21	1.55	0.15	1.18	0.28	21	1
Mar	0.39	0.28	1.49	0.31	1.27	0.31	23	1
Apr	0.39	0.38	1.50	0.36	1.71	0.48	14	1
May	0.46	0.23	1.62	0.15	2.17	0.35	23	1
Jun	0.52	0.38	1.44	0.24	3.02	0.87	27	1
Jul	0.37	0.30	1.61	0.13	3.25	0.70	42	2
Aug	0.40	0.20	1.57	0.16	3.50	0.78	50	2
Sep	0.44	0.37	1.46	0.23	2.61	0.84	37	2
Oct	0.35	0.27	1.39	0.30	2.10	0.70	32	2
Nov	0.22	0.15	1.46	0.28	1.61	0.54	14	1
Dec	0.21	0.10	1.56	0.24	1.43	0.25	6	1
YEAR	0.36	0.10	1.52	0.07	2.06	0.87	301	16

Bahrain (Lat 26°19′N Long 50°30′W, elevation 0 m), 1998-1999.

	τ_{a500}	σ	α	σ	PW	σ	N	Mo.
Jan	0.23	0.09	1.21	0.21	1.84	0.64	22	1
Feb	0.29	0.11	1.00	0.27	2.29	0.70	14	1
Mar	0.27	0.14	0.78	0.54	1.53	0.39	26	1
Apr	0.33	0.12	0.68	0.21	1.88	0.55	30	1
May	0.34	0.16	0.52	0.18	1.78	0.53	31	1
Jun	0.32	0.09	0.68	0.18	1.67	0.24	21	1
Jul	0.48	0.19	0.55	0.28	2.76	0.87	30	2
Aug	0.45	0.15	1.10	0.23	3.61	0.89	31	1
Sep	0.38	0.11	1.03	0.22	3.12	0.74	28	1
Oct	0.25	0.09	1.25	0.29	2.29	0.65	31	1
Nov	0.24	0.06	1.34	0.25	1.95	0.30	28	1
Dec	0.21	0.07	1.26	0.19	1.79	0.68	29	1
YEAR	0.32	0.09	0.95	0.30	2.21	0.64	321	13

Maldives

Kaashidhoo (Lat 04°57′N Long 73°27′E, elevation 0 m), 1998-1999.

	τ_{a500}	σ	α	σ	PW	σ	N	Mo.
Jan	0.27	0.10	1.09	0.32	4.46	0.81	13	1
Feb	0.28	0.14	1.24	0.17	4.72	0.81	27	2
Mar	0.30	0.17	1.24	0.21	4.56	0.61	48	2
Apr	0.26	0.19	1.01	0.31	5.42	0.66	49	2
May	0.19	0.09	0.62	0.30	5.88	0.56	26	2
Jun	0.13	0.05	0.43	0.16	5.27	0.73	25	2
Jul	0.20	0.08	0.30	0.12	4.81	0.65	14	2
Aug	0.15	0.04	0.52	0.34	4.89	0.52	32	2
Sep	0.11	0.05	0.62	0.41	5.39	0.38	38	2
Oct	0.13	0.07	0.75	0.38	5.09	0.49	34	2
Nov	0.17	0.10	1.07	0.38	4.73	0.76	46	2
Dec	0.17	0.10	0.97	0.35	5.00	0.88	31	2
YEAR	0.20	0.07	0.82	0.32	5.02	0.41	383	23

Mongolia

Dalanzadgad (Lat 43°34′N Long 104°25′E, elevation 1470 m), 1997-2000.

	τ_{a500}	σ	α	σ	PW	σ	N	Mo.
Jan	0.07	0.04	1.34	0.64	0.22	0.09	29	2
Feb	0.10	0.05	0.94	0.57	0.25	0.08	31	2
Mar	0.21	0.25	0.58	0.35	0.27	0.10	58	3
Apr	0.22	0.23	0.68	0.37	0.50	0.20	56	3
May	0.25	0.19	0.78	0.42	0.76	0.32	52	3
Jun	0.14	0.09	0.61	0.35	1.02	0.30	34	3
Jul	0.14	0.12	1.32	0.62	2.08	0.58	31	3
Aug	0.15	0.15	1.13	0.78	1.44	0.42	36	3
Sep	0.11	0.09	1.30	0.57	1.07	0.45	46	2
Oct	0.06	0.04	1.62	0.67	0.62	0.20	38	2
Nov	0.06	0.06	1.55	0.51	0.43	0.16	32	2
Dec	0.05	0.03	1.82	0.68	0.23	0.07	16	2
YEAR	0.13	0.07	1.14	0.42	0.74	0.58	459	30